

# Numerical Analysis of Offshore Wind Farm Wakes and their Impact on the Marine Boundary Layer

INAUGURAL-DISSERTATION

zur

ERLANGUNG DES DOKTORGRADES

DER MATHEMATISCHEN-NATURWISSENSCHAFTLICHEN  
FAKULTÄT  
DER UNIVERSITÄT ZU KÖLN

vorgelegt von

SIMON KARL SIEDERSLEBEN  
aus MÜNCHEN

Garmisch-Partenkirchen

2019

Berichterstatter, Gutachter:

Prof. Dr. Stefan Emeis

Prof. Dr. Yaping Shao

Tag der mündlichen Prüfung: 31.10.2019



*To my family*



# Abstract

Given the rising number of offshore wind farms, the effect of wakes (the area downwind of wind farms characterized by a wind speed deficit) on downwind wind farms and their impact on the regional climate is discussed. This work investigates the spatial dimensions of wakes and the micrometeorological and regional climate impacts of offshore wind farms on the marine boundary layer based on mesoscale simulations using a wind farm parameterization (WFP) and airborne observations.

WFPs act as a momentum sink for the mean flow. However, WFPs differ on whether or not they add additional turbulent kinetic energy (TKE) to represent the enhanced mixing caused by wind farms. This thesis uses for the first time aircraft observations taken above and behind offshore wind farms to answer this uncertainty for stable conditions. The airborne measurements reveal that a TKE source and a horizontal resolution in the order of 5 km are necessary to represent the enhanced TKE (i.e. 20 times higher than in the ambient flow) above offshore wind farms.

Further, this thesis evaluates the simulated spatial extent of a wake by the use of airborne measurements taken on 10 September 2016. Observations and simulations show a wake longer than 45 km associated with a warming and drying at hub height in the order of 0.5 K and 0.5 g kg<sup>-1</sup>, respectively. Vertical cross-sections perpendicular to the wake reveal that warmer and dryer air was mixed towards the surface due to an inversion located within the rotor area. An analysis of 23 additional airborne measurements executed within the far-field of offshore wind farms suggests that an impact on the temperature is only visible in case of inversions in the vicinity of the rotor area and wind speeds over  $\approx 6$  m s<sup>-1</sup>.

Based on the successful evaluations above and downwind of offshore wind farms, this thesis explores a future scenario including all offshore wind farms possibly installed at the German Bight to discuss potential impacts of large offshore wind farms on the regional climate by considering two case studies. The simulations suggest that the wakes of large offshore wind farms clusters are longer than 100 km associated with changes in the sensible and latent heat flux. The net impact on the MABL depends on the inversion height and the temperature gradient between sea surface temperature (SST) and air temperature. Therefore, the dominating impact of offshore wind farms can only be determined by simulations covering several years with the constraint that the inversion height is captured by the driving mesoscale model.



# Zusammenfassung

Durch die steigende Anzahl von Offshore-Windparks werden die Auswirkungen von Nachläufen großer Offshore-Windparks auf leewärts gelegene Windparks diskutiert. Zudem ist es unklar, inwiefern große Offshore-Windparks die marine Grenzschicht und das regionale Klima beeinflussen können. Diese Doktorarbeit untersucht die räumliche Ausbreitung von Nachläufen und deren Einfluss auf die Mikrometeorologie und das regionale Klima mit mesoskaligen Simulationen, die eine Windparkparametrisierung (WFP) verwenden. Die Simulationen werden mit Flugzeugmessungen evaluiert.

WFPs entziehen der Modellatmosphäre kinetische Energie, der Effekt auf die turbulente kinetische Energie (TKE) wird jedoch unterschiedlich gehandhabt. Manche der WFPs repräsentieren eine zusätzliche TKE-Quelle im Modell, wohingegen andere nur eine Impulssenke darstellen. In dieser Arbeit werden erstmals beide Ansätze mit Flugzeugmessungen evaluiert, die über und hinter großen Offshore-Windparks durchgeführt wurden. Hier hat sich gezeigt, dass eine TKE-Quelle und eine Auflösung von 5 km oder feiner notwendig sind um die erhöhte TKE (20-mal höher als in der unmittelbaren Umgebung) zu erfassen.

Basierend auf diesen Ergebnissen, evaluiert diese Arbeit die räumliche Ausbreitung der Nachläufe mit Flugzeugmessungen vom 10. September 2016. Beobachtung und Simulation zeigen erstmals einen Nachlauf mit einer Länge von über 45 km, charakterisiert durch eine Erwärmung und trockenere Luft in Nabenhöhe in der Größenordnung von 0.5 K und 0.5 g kg<sup>-1</sup>; 45 km leewärts des Windparks. Vertikale Schnitte senkrecht zur Windrichtung zeigen, dass aufgrund einer Inversion auf Nabenhöhe wärmere und trockenere Luft nach unten gemischt wurde. Eine Analyse von 23 weiteren beobachteten Fällen zeigt, dass eine Temperaturänderung auf Nabenhöhe nur in Verbindung mit einer stabilen Schichtung und Windgeschwindigkeiten über  $\approx 6 \text{ m s}^{-1}$  in Höhe des Rotorbereichs auftritt.

Basierend auf den erfolgreichen Evaluationen über und leewärts großer Offshore-Windparks, werden die Simulationen erweitert und ein Zukunftsszenario wird untersucht, das alle möglichen offshore Windparks der Deutschen Bucht enthält um erstmals deren potentiellen Einfluss auf das regionale Klima zu diskutieren. Die Simulationen zeigen Nachläufe von großen Offshore-Windparkclustern mit einer Länge von über 100 km in Verbindung mit Änderungen im sensiblen und latenten Wärmefluss während stabiler Bedingungen. Zudem ist der Temperaturgradient zwischen Meeres-

oberflächentemperatur und Lufttemperatur entscheidend für den Nettoeinfluss der Windparks auf die marine Grenzschicht. Deswegen kann der dominierende Einfluss auf das regionale Klima nur mit Simulationen bestimmt werden, die mehrere Jahre abdecken und in der Lage sind die exakte Höhe der Inversionen über der Deutschen Bucht zu erfassen.

# Contents

<b>Abstract</b>	<b>iii</b>
<b>Zusammenfassung</b>	<b>v</b>
<b>Contents</b>	<b>vii</b>
<b>1 General introduction and motivation</b>	<b>1</b>
1.1 State of the art . . . . .	1
1.1.1 Meteorological conditions at offshore sites . . . . .	2
1.1.2 Wind speed deficit in the far-field of offshore wind farms . . . . .	4
1.1.3 Micrometeorological, regional and global climate impacts of on-shore and offshore wind farms . . . . .	7
1.2 Open questions and objectives of the present study . . . . .	9
<b>2 Dataset and method</b>	<b>12</b>
2.1 Aircraft observations . . . . .	12
2.1.1 Uncertainties in the aircraft measurements . . . . .	12
2.1.2 Vertical profiles . . . . .	12
2.1.3 In the far-field of offshore wind farms . . . . .	14
2.1.4 Above offshore wind farms . . . . .	14
2.2 Synthetic Aperture Radar Data (SAR) . . . . .	16
2.3 Ground-based observations . . . . .	17
2.4 Reanalysis Data: ECMWF analysis and ERA5 data . . . . .	18
2.5 Wind farm parameterization . . . . .	18
2.6 Numerical Setup . . . . .	19
2.6.1 Control configuration . . . . .	20
2.6.2 Sensitivity configurations . . . . .	21
2.7 Wind farms implemented in the numerical model . . . . .	22
2.8 Energy budget framework . . . . .	23
<b>3 Wind speed and TKE above offshore wind farms</b>	<b>25</b>
3.1 Observations . . . . .	25
3.1.1 Synoptics and mesoscale overview . . . . .	25

3.1.2	Wind speed above and next to the wind farms . . . . .	26
3.1.3	TKE above and next to the wind farms . . . . .	28
3.2	Control simulations . . . . .	29
3.2.1	Evaluation of the background flow . . . . .	29
3.2.2	Impact of wind farm parameterization on wind speed above wind farms . . . . .	30
3.2.3	Impact of wind farm parameterization on TKE above wind farms	31
3.3	Sensitivity experiments . . . . .	33
3.3.1	Sensitivity to horizontal and vertical resolution with an active TKE source . . . . .	34
3.3.2	Sensitivity to vertical resolution with a disabled TKE source . .	36
3.3.3	Sensitivity to advection of TKE . . . . .	36
3.3.4	Sensitivity to thrust coefficient . . . . .	37
3.4	Discussion . . . . .	38
3.5	Summary . . . . .	40
<b>4</b>	<b>The far-field of large offshore wind farms</b>	<b>43</b>
4.1	Observation . . . . .	43
4.1.1	Synoptic and mesoscale overview . . . . .	43
4.1.2	Vertical structure of the atmosphere . . . . .	44
4.2	Control run . . . . .	46
4.2.1	Verification of the background flow . . . . .	46
4.2.2	Evolution of the wind field upwind of the wind farms . . . . .	47
4.2.3	Wake simulations . . . . .	48
4.3	Sensitivity experiment . . . . .	54
4.4	Discussion . . . . .	56
4.4.1	Discussion of the wake simulations . . . . .	56
4.4.2	Comparison to other cases . . . . .	59
4.5	Summary . . . . .	64
<b>5</b>	<b>Potential micrometeorological and regional climate impacts of large offshore wind farms on the atmospheric boundary layer</b>	<b>66</b>
5.1	Offshore winds and stable conditions . . . . .	66
5.2	Onshore winds and stable conditions . . . . .	68
5.3	Discussion . . . . .	71
5.4	Summary . . . . .	73
<b>6</b>	<b>Conclusion and outlook</b>	<b>75</b>
6.1	Main results and conclusions . . . . .	75
6.2	Suggestions for further studies . . . . .	78

*CONTENTS*

ix

<b>Bibliography</b>	<b>81</b>
<b>Acknowledgments</b>	<b>93</b>
<b>Erklärung</b>	<b>95</b>



# 1 General introduction and motivation

The first offshore wind farm was installed in 1991 at the coast of Vindeby, Denmark (ØRSTED 2019). Associated with the nuclear catastrophe of Fukushima and the urgent need to stop climate warming, the wind energy offshore market has grown continuously since 1991. In 2017, Europe had a capacity of 16 GW installed offshore with 71 % in the North Sea (WINDEUROPE 2017).

The wind speed downwind of large offshore wind farms can be reduced, even 50 km downwind, as indicated by satellite images (e.g., CHRISTIANSEN and HASAGER 2005; HASAGER et al. 2005, 2015). Offshore wind farms extract kinetic energy from the mean flow and convert it into electrical energy. Consequently, the wind speed is reduced downwind of large offshore wind farms. Throughout this thesis, we refer to this area, characterized by a wind deficit, as a wake. Given the rising number and the large size of offshore wind farms, two issues arise associated with wakes of offshore wind farms.

Wakes of upwind offshore wind farms reduce the energy harvesting in wind farms located downwind and, hence, the yields of stakeholders. Offshore wind farms are clustered around transmission grids to redeem the high costs of installation and due to restrictions in space caused by military zones, pipelines and nature preserves. Hence, offshore wind farms are often only 10 km apart. Therefore, wind energy production losses are observed in downwind wind farms due to wakes from upwind wind farms (e.g., NYGAARD 2014; NYGAARD and HANSEN 2016; LUNDQUIST et al. 2018). Consequently, the wind energy industry has a great interest in determining the spatial scales of these wakes, especially under stable conditions when these wakes are expected to be longest due to the low turbulent vertical momentum transport (e.g., EMEIS et al. 2016).

The impact of offshore wind farms on the regional climate is unclear. Offshore wind farms represent an additional source of turbulence in the marine atmospheric boundary layer (MABL) (FITCH et al. 2012). Therefore, the temperature and moisture budget can be affected by offshore wind farms and, hence, the turbulent fluxes between atmosphere and open ocean could be altered by wind farms. Consequently, the impact of large offshore wind farms on the MABL needs to be investigated.

These two topics are of major importance for stakeholders and a sustainable development of the offshore wind energy industry and are, hence, in the focus of ongoing research. The remaining chapter presents the state of the art in section 1.1, developing the research questions in section 1.2.

## 1.1 State of the art

To understand the nature of wakes of large offshore wind farms, knowledge about the MABL is necessary. This information is provided in section 1.1.1, followed by two sections, presenting previous findings about the length of wakes of large offshore

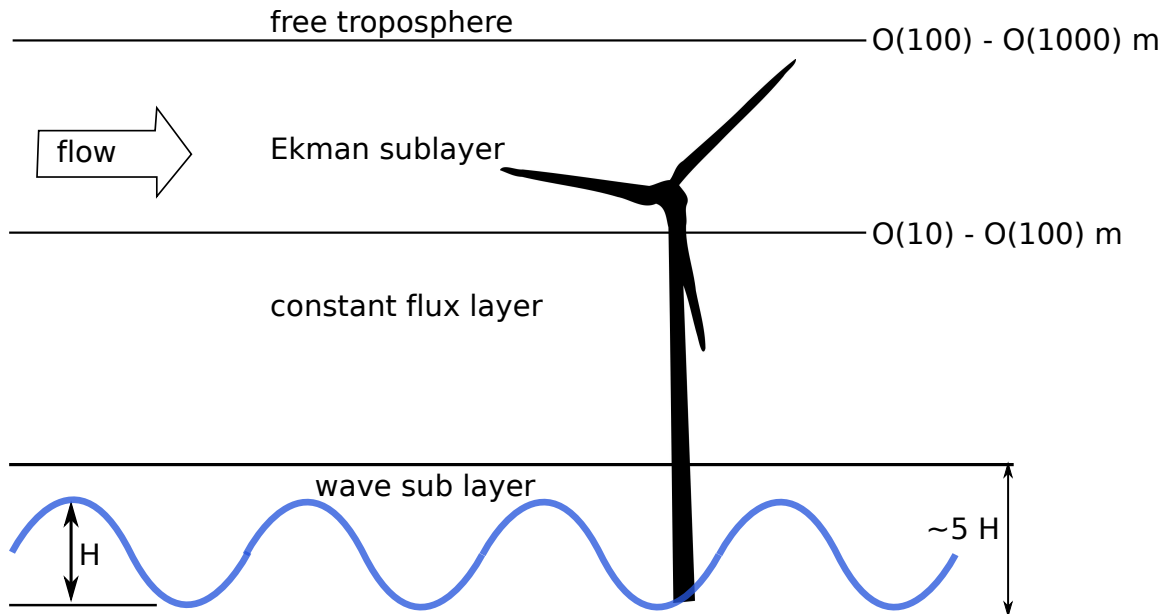


**Figure 1:** The marine atmospheric boundary layer and its vertical structure. The blue line indicates the ocean’s surface with the wave height  $H$ . (Adapted from EMEIS (2018). The wind turbine icon is taken from <https://svg-clipart.com/white/Ta0k2H4-wind-turbine-clipart>.)

wind farms (section 1.1.2) and observed and simulated impacts of wind farms on the micrometeorology and regional climate (section 1.1.3).

### 1.1.1 Meteorological conditions at offshore sites

Offshore sites are characterized by higher wind speeds compared to onshore sites. The shape of vertical wind profiles is determined by the stability of the atmosphere and the surface roughness. The roughness of the ocean is linked to the wave height, and thus to the wind speed (EMEIS 2018). Consequently, the surface roughness at offshore sites is controlled by the wind drag acting on the water surface. CHARNOCK (1955) describes the surface roughness length over water as

$$z_0 = \alpha \frac{u_*^2}{g}, \quad (1)$$

with  $\alpha$ , the Charnock parameter having a value of 0.011 for the open ocean according to SMITH (1980) and  $u_*$ , the friction velocity. Following equation (1) with  $u_* = 0.33 \text{ m s}^{-1}$ , we can expect a surface roughness length over the ocean in the order of  $10^{-4} \text{ m}$  that is at least two orders of magnitude lower than the surface roughness length for onshore sites (i.e. grassland has a surface roughness length of 0.01 m (EMEIS 2018)). Consequently, the wind speed over the ocean is higher than at onshore sites. Additionally, the low surface roughness results in a vertical wind speed gradient with low shear at the rotor area, which in turn results in a balanced wind drag at the rotor tips. Such conditions are favorable for a slow fatigue of wind turbines.

The MABL is characterized by low turbulence in contrast to onshore sites. Two

ingredients are necessary for turbulence - shear and buoyancy. Given the low surface roughness of the ocean, shear is generally low over the ocean, resulting in low mechanical production of turbulence. Additionally, the surface temperature of the ocean is almost constant during the day due to the high heat capacity of water (EMEIS 2018). Consequently, large eddies as observed onshore can not exist offshore meaning that the turbulence generated by buoyancy is lower at offshore sites. Summarized, the turbulence offshore is lower than onshore (TÜRK and EMEIS 2010; BODINI et al. 2019).

The MABL is generally shallower than the boundary layer at onshore sides (EMEIS 2018), rooted in the low turbulence at offshore sites. That is important to recognize when considering the dimensions of modern wind turbines. A hub height of  $\approx 100$  m and rotor diameter of  $\approx 150$  m are quite common, resulting in a rotor tip reaching a height of  $\approx 175$  m. Consequently, wind farms are high enough to interact with the constant flux layer and the Ekman sublayer (Fig. 1). Within the constant flux layer, turbulent fluxes only vary with  $\pm 10\%$ , reaching a height of  $\approx 10\%$  of the height of the MABL. Above the constant flux sublayer is the Ekman sublayer, characterized by a clockwise turning of the wind direction due to decreasing surface friction. At the top of the Ekman sublayer no friction is present anymore, hence, the wind is geostrophically balanced (EMEIS 2018).

Most offshore wind farms in the North Sea that were under construction in 2017, are located at sites not further than 60 km away from the coast (Fig. 2) (WIND EUROPE 2017), having the advantage that the installation of wind turbine platforms is easier in these regions due to water depths less than 60 m (Fig. 2). Additionally, the costs for transmission grids and maintenance can be minimized.

Given the close proximity of offshore wind farms to the coast, the MABL at offshore wind farms is influenced by the shore. Well known are stable conditions at offshore sites caused by the interaction of ocean and the ambient shore during spring and early summer. During daytime, the sea surface temperature (SST) is relatively constant due to the high heat capacity of water. In contrast, the ambient shore warms rapidly and causes an unstable stratification close to the ground (Fig. 3) (SMEDMAN et al. 1997). In case of offshore winds, warm air stemming from the land upwind is advected over the ocean. The advection of warm air associated with a cold SST causes a neutral layer close to the surface followed by a stable internal boundary layer over the ocean, rooted in a turbulent transport of heat towards the ocean resulting in a more pronounced cooling of the air close to the ocean's surface (e.g. SMEDMAN et al. 1996, 1997; MELAS 1998; LANGE et al. 2004; SATHE et al. 2011) as indicated in Fig. 3. According to the simulations of SMEDMAN et al. (1997), the neutral layer grows with increasing distance to the shore, resulting in a strengthening of the capping inversion. According to EMEIS (2010b), such conditions are favorable for long wakes of offshore wind farms.

Another mesoscale phenomenon influencing offshore regions in the vicinity of coasts

are sea breeze systems (e.g. SIMPSON 1994; MILLER et al. 2003). The differential heating of land and water bodies results in a pressure gradient, pointing towards the open sea during day time and vice versa during night time. Therefore, a mesoscale system develops that is known as sea breeze. In the literature, three different sea breeze types are described (MILLER et al. 2003). The most prominent type is the pure sea breeze type, where the gradient wind is pointing offshore whereas the sea breeze blows onshore. As the gradient wind depends on the dominating synoptic system, the gradient wind is not always orientated perfectly perpendicular to the shoreline (MILLER et al. 2003). Therefore, different types of sea breeze systems exist depending on the shape of the shore and the prevailing wind direction (STEELE et al. 2012, 2015). Sea breeze systems can propagate up to 200 km offshore (STEELE et al. 2015). Consequently, sea breeze systems influence the wind speed and direction at most offshore sites according to Fig. 2.

Besides the temperature difference between on- and offshore regions the surface roughness at the shore can have an impact on the wind speed over the ocean during stable stratifications. DÖRENKÄMPER et al. (2015) showed that the varying surface roughness at the coast is responsible for jet streaks close to the surface, propagating more than 100 km offshore during stable conditions i.e. resulting from warm air advection as sketched in Fig. 3. Consequently, the surface roughness at the shore can influence the energy harvesting offshore during stable conditions.

### 1.1.2 Wind speed deficit in the far-field of offshore wind farms

Due to the large size of offshore wind farms and the low turbulence offshore, wakes of wind farms are longer offshore than onshore. Satellite and aircraft observations have revealed that offshore wakes can be longer than 50 km (HASAGER et al. 2015; PLATIS et al. 2018). According to analytical models (e.g., FRANSEN et al. 2006; EMEIS 2010b), the length of wakes is driven by the vertical momentum flux above wind farms. Wind turbines extract kinetic energy from the mean flow and convert it partly into electrical energy. The resulting wind deficit downwind is balanced by the advection of momentum of the mean flow and the turbulent momentum fluxes. Within large wind farms, the kinetic energy deficit is mostly balanced by the vertical momentum flux as the inner turbines are surrounded by wind turbines extracting the kinetic energy from the mean horizontal flow. Therefore, the wind speed reduction caused by the wind turbines upwind can only be balanced by the vertical momentum flux. Given the generally low mean vertical velocities, the turbulent vertical momentum flux determines the length of the wakes. However, the intensity of vertical momentum flux is directly related to the turbulence that in turn is known to be lower for offshore sites than for onshore sites. Consequently, wakes offshore are longer than wakes onshore (EMEIS 2018).

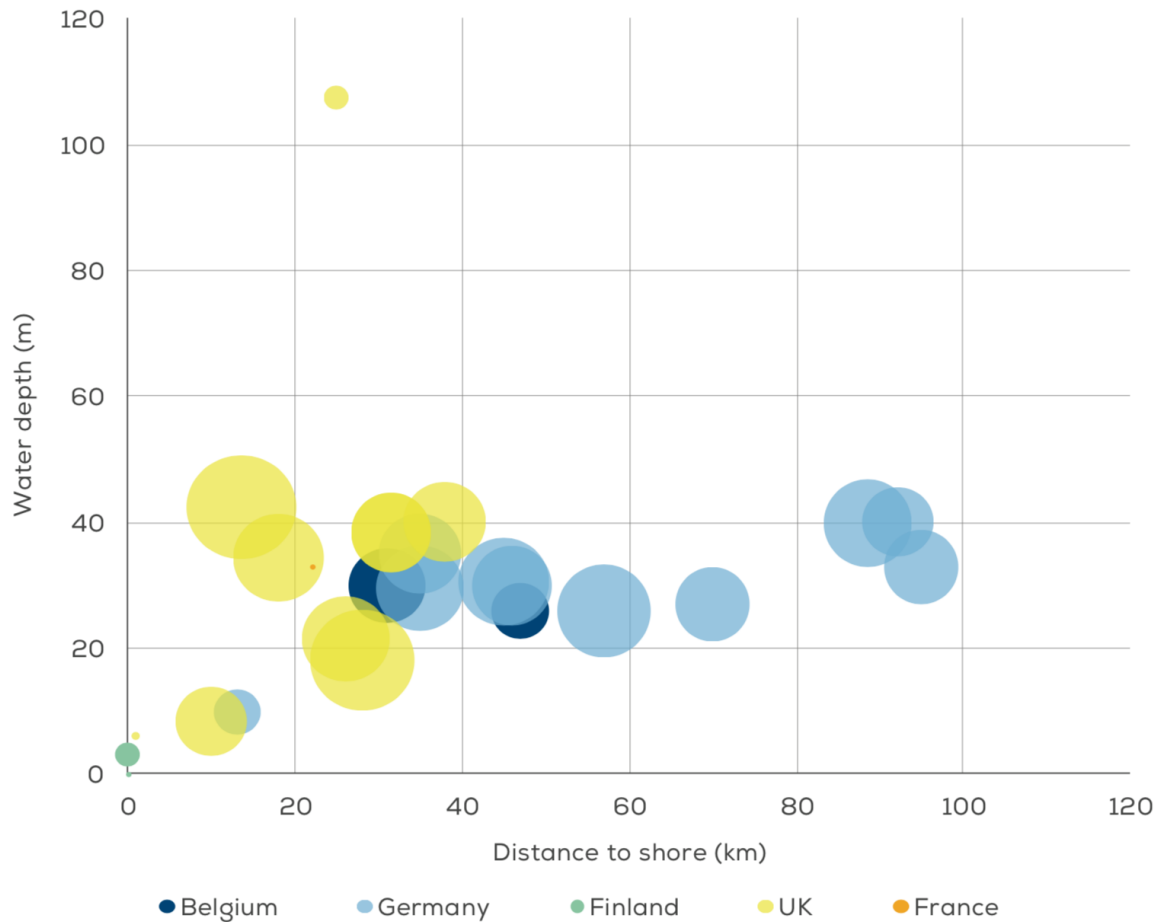


**Figure 2:** Distance to coast and average water depth of wind farms under construction in 2017. (Taken from WINDEUROPE (2017))

Obviously, the wind energy industry has a great interest in forecasting the length of such wakes for economical reasons. NYGAARD (2014) and NYGAARD and HANSEN (2016) showed that a downwind located wind farm produced less energy than the wind farm located upwind. In the US, MILLER and KEITH (2018b) showed, based on measurements, that wakes of single wind turbines and wind farms decrease the power density of wind farms below  $1 \text{ W m}^{-2}$ , agreeing with results conducted on a global scale based on simulation of MILLER et al. (2015); VOLKER et al. (2017).

Consequently, such aspects have to be considered during the planning process and the operation of a wind farm. Given the interest of stakeholders in wakes, a lot of simulations were conducted, exploring wakes on all scales. Simulations based on large-eddy simulations (LES) models, investigating the wakes of single wind turbines within a wind farm were executed in the past (e.g., CALAF et al. 2010, 2011; PORTÉ-AGEL et al. 2011; WU and PORTÉ-AGEL 2015; VANDERWENDE et al. 2016; XIE and ARCHER 2017). However, simulations covering the scales of a single wind turbine are computational too expensive to investigate the interaction of several wind farms.

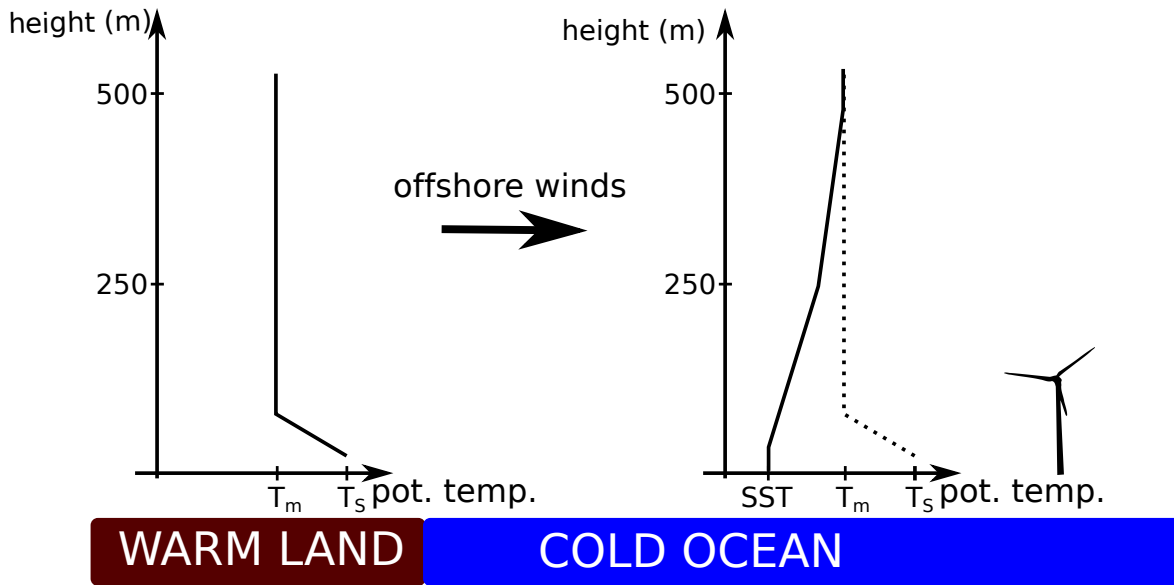


**Figure 3:** Schematic sketch of the evolution of a stable stratification over the ocean caused by warm air advection.  $T_m$  and  $T_S$  are the potential temperatures within the mixed layer and of the land surface, respectively. (This figure is based on the simulation and observational results of SMEDMAN et al. (1997). The wind turbine icon is taken from <https://svg-clipart.com/white/Ta0k2H4-wind-turbine-clipart>.)

Therefore, the wind industry favors simple engineering models because of their low computational cost. A commonly used model is the Park model based on the theory of JENSEN (1983), suited to represent the wakes of several single wind turbines, but not for representing deep-array effects, i.e. when an internal boundary layer develops due to intensive mixing within very large wind farms. Consequently, the Jensen model underestimates wake losses downwind of the third row when applying the model to large offshore wind farms (BEAUCAGE et al. 2012). Therefore, more sophisticated industrial models combine boundary layer models with single wind turbine wake models to cover the interactions on wind turbine and wind farm scale (BROWER and ROBINSON 2012). All these industrial models do not account for atmospheric stability although EMEIS (2010b) showed by using an analytical model that the wakes of offshore wind farms are significantly longer during stable conditions. In contrast, mesoscale models represent atmospheric stability. Such models have a horizontal grid size in the order of one kilometer. Consequently, mesoscale models do not resolve the effect of a single wind turbine on the atmosphere explicitly. However, it is possible to represent wind farms in mesoscale models by the use of parameterizations. In former studies, wind farms were represented as an area of increased surface roughness (e.g., IVANOVA and NADYOZHINA 2000; KEITH et al. 2004; WANG and PRINN 2010, 2011), a popular approach especially for global climate simulations (KEITH et al. 2004) as no additional computational resources need to be applied. However, this surface roughness based approach causes a too weak momentum deficit downwind of the wind farms during nocturnal conditions

(FITCH et al. 2013).

Nowadays, wind farms are represented as an elevated momentum sink for the mean flow in mesoscale models (e.g. FITCH et al. 2012; VOLKER et al. 2015). FITCH et al. (2012) adds turbulent kinetic energy (TKE) at rotor height, representing the additional TKE introduced by the wind turbines. In contrast, JACOBSON and ARCHER (2012) and VOLKER et al. (2015) let the TKE evolve based on the resolved shear instead of adding TKE directly. Some studies showed that the amount of TKE that is introduced by the parameterization of FITCH et al. (2012) is too excessive (e.g., ABKAR and PORTÉ-AGEL 2015; VOLKER et al. 2015; PAN and ARCHER 2018). Therefore, ABKAR and PORTÉ-AGEL (2015) and PAN and ARCHER (2018) introduced updates to the wind farm parameterization (WFP) of FITCH et al. (2012). In both studies, the authors use LES simulations to account for geometric effects within one grid cell (i.e. staggered vs. unstaggered wind farm) and wind direction. Additionally, they introduce a TKE source, that is also based on the LES results. However, this approach is computationally expensive as the LES results are not transferable to wind farms with a different layout. Additionally, the number of necessary LES simulations is the product of the number of wind farms, number of wind directions and atmospheric conditions and, hence, computationally expensive. Further, the WFP of PAN and ARCHER (2018) has the disadvantage that all wind turbines of a wind farm need to be within one grid cell, meaning that the wind farm size determines the simulation's horizontal grid.

### 1.1.3 Micrometeorological, regional and global climate impacts of onshore and offshore wind farms

Wind farms can impact the boundary layer. They represent an artificial source of turbulence, resulting in an enhanced mixing of the boundary layer at rotor area but also below and above rotor area. As measurements below and downwind of onshore wind farms are easy to realize compared to offshore sites, recently published studies based on observations focused on the impact of onshore wind farms on surface air temperature and soil moisture. Several studies showed that additional mixing at onshore wind farm sites was accompanied by a warming at the surface under stable conditions (e.g., ROY and TRAITÉUR 2010; ZHOU et al. 2012; RAJEWSKI et al. 2013; SMITH et al. 2013; RAJEWSKI et al. 2014; ARMSTRONG et al. 2016). For example, ROY and TRAITÉUR (2010) and ARMSTRONG et al. (2016) observed a warming of  $\approx 0.2$  K downwind of onshore wind farms at 5 m and 2 m, respectively, especially during nocturnal stable conditions. In contrast, a cooling of  $\approx 1$  K was measured by ROY and TRAITÉUR (2010) during daytime. Therefore, the implications of onshore wind farms on agriculture are discussed (e.g., ROY and TRAITÉUR 2010; RAJEWSKI et al. 2013; SMITH et al. 2013; ZHANG et al. 2013).

Only a few observational studies focused on the impact of offshore wind farms on

the MABL. These studies are all based on photos - except FOREMAN et al. (2017) and BOETTCHER et al. (2015), showing fog formation and dispersion due to the enhanced mixing of the wind farm at Horns Rev (EMEIS 2010a; HASAGER et al. 2013, 2017). The measurements of FOREMAN et al. (2017) taken at FINO1, a stationary tower located in the North Sea, revealed that the enhanced mixing in turn, has an influence on the sensible heat flux during stable conditions. BOETTCHER et al. (2015) simulates a change in cloud cover in the vicinity of Hamburg associated with the installation of wind farms in the North Sea. However, these results are based on simulation using a WFP that was so far not evaluated with observations.

Also, studies based on simulations report an impact of wind farms on the atmospheric boundary layer. Regional climate simulations for Europe obtained a significant change in temperature and precipitation in the order of  $\pm 0.3$  and 0-5 % (VAUTARD et al. 2014), respectively. These changes are most significant during the winter season and were partly attributed to local and large-scale effects. In contrast, PRYOR et al. (2018a,b) found a significant impact of wind farms in Iowa only during the summer season, with a maximal temperature difference of 0.5 K. These conflicting results arise either from the different climates of Europe and Iowa and/or the different horizontal grid size they used in their simulations (i.e. 50 km vs. 4 km) (PRYOR et al. 2018b). A third study of SUN et al. (2018) investigating the impact of onshore wind farms in China, concludes that wind farms have a significant impact during winter and summer. They observed mainly a temperature increase during winter and a warming during summer at the east coast of China associated with a cooling inland, whereby the impact did not exceed the interannual climate variability (SUN et al. 2018).

Compared to studies based on measurements and regional simulations, global simulations allow an investigation of the impact of wind farms on the global atmospheric circulation. Although WANG and PRINN (2011) covered large offshore areas with wind farms (i.e. all offshore sites with a water depth below 600 m between  $60^\circ$  S and  $74^\circ$  N), they observed only weak non-local impacts due to the presence of wind farms. However, they parameterized the wind farms as areas of increased surface roughness. According to FITCH et al. (2013), this kind of approach is not suitable to investigate the impact of wind farms on the climate as this approach overestimates the temperature change during nocturnal conditions. In contrast to WANG and PRINN (2011), POSSNER and CALDEIRA (2017) obtained surface temperature differences in the order of up to  $\approx 15$  K affecting an area expanding from Iceland to Svalbard when installing a wind farm with an unrealistic size of  $0.67 \cdot 10^6$  km<sup>2</sup> (equal to two times the size of Germany) in the North Atlantic, south of Iceland. In general, the installation of large renewable energy power plants in extreme environments seems to have the biggest impact on atmospheric circulation. Recently, LI et al. (2018) showed that the installation of wind and solar power plants in the Sahara Desert would lead to increased temperatures and a doubling

of the precipitation in the Sahel region due to enhanced surface friction and reduced albedo. Given the potentially large impact of offshore wind farms, PAN et al. (2018) investigated whether a wind farm could reduce the hurricane threat along the coast of the Gulf of Mexico. They showed that wind farms could have reduced the precipitation and wind speed at hub height by 100 mm and  $5 \text{ m s}^{-1}$ , respectively, during hurricane Harvey.

Similar to mountains, wind farms impose an obstacle to the atmospheric flow and perturb the pressure field, hence, wind farms can trigger gravity waves. Due to conservation of mass, this pressure perturbation results either in an acceleration at the flanks of a wind farm and/or an enhanced flow over the wind farms, equal to a vertical lift for air parcels going over the wind farm. During stable conditions, this lift can cause gravity waves as it is described in SMITH (2010) and ALLAERTS and MEYERS (2018). They both suggest that gravity waves are most likely to be observed in atmospheres with a Froude number close to unity. However, SMITH (2010) concluded that a low surface drag with a Froude number close to unity causes a strong blocking and, hence, an increased extinction of gravity waves. In contrast, ALLAERTS and MEYERS (2018) found that a low surface drag plays a minor role in generating gravity waves.

## 1.2 Open questions and objectives of the present study

Mesoscale wind farm parameterizations (WFP) need to be evaluated for offshore regions. The performance of WFPs for mesoscale models has been so far only investigated either in idealized simulations (e.g., VOLKER et al. 2015; CHATTERJEE et al. 2016; VANDERWENDE et al. 2016) or for onshore sites LEE and LUNDQUIST (2017) - except JIMÉNEZ et al. (2015) and HASAGER et al. (2015). JIMÉNEZ et al. (2015) evaluated the WFP of FITCH et al. (2012) by the use of energy production data of a single offshore wind farm (Horns Rev) off the Danish coast. Consequently, they were not able to evaluate the spatial dimensions of the wake of the Horns Rev wind farm. Taking into account that more wind farms are planned to be built in the North Sea, resulting in shorter distances between the wind farms, the spatial scales of wakes are of major interest for wind energy stakeholders. Additionally, idealized simulations neglect moisture effects and assume a neutral stratification with a uniform upwind inflow, although offshore wind farms are exposed to stable conditions and topographic effects introduced by the coast (see section 1.1.1). Consequently, measurements are needed to evaluate the performance of WFPs in real case simulations.

Additionally, although there is disagreement over to whether or not use an additional TKE source in WFPs, the simulated impact on the marine atmosphere has not been evaluated for real case studies. Several studies based on simulations suggest (e.g., ERIKSSON et al. 2015; VANDERWENDE et al. 2016) that the WFP of FITCH et al. (2012) adds too much TKE into the model causing exaggerated mixing. However, the

TKE and the associated change in the vertical fluxes over wind farms is difficult to evaluate, especially for offshore wind farms due to their remote locations. Therefore, implications of mesoscale WFPs on the TKE were so far not evaluated although they are of major importance when estimating the impact of large offshore wind farms on the MABL.

The uncertainty considering the TKE source of WFPs, could lead to wrong mesoscale wake simulations. According to analytical models, the impact of large offshore wind farms is rooted in an enhancement of the vertical fluxes above wind farms (EMEIS et al. 2016). As some boundary layer parameterizations (e.g. NAKANISHI and NIINO (2006)) calculate the vertical fluxes diagnostically based on the TKE, a careful evaluation of TKE over the wind farms is necessary before the simulated wakes can be evaluated.

Summarized, it is not clear whether WFPs can simulate realistic wakes under stable conditions when the impact on the MABL is expected to be largest, as the optimal configuration of the WFP is not known, i.e. with or without a TKE source and with which resolution of the driving mesoscale model. Consequently, assessments of the regional climate impact of offshore wind farms based on mesoscale simulations have a large uncertainty.

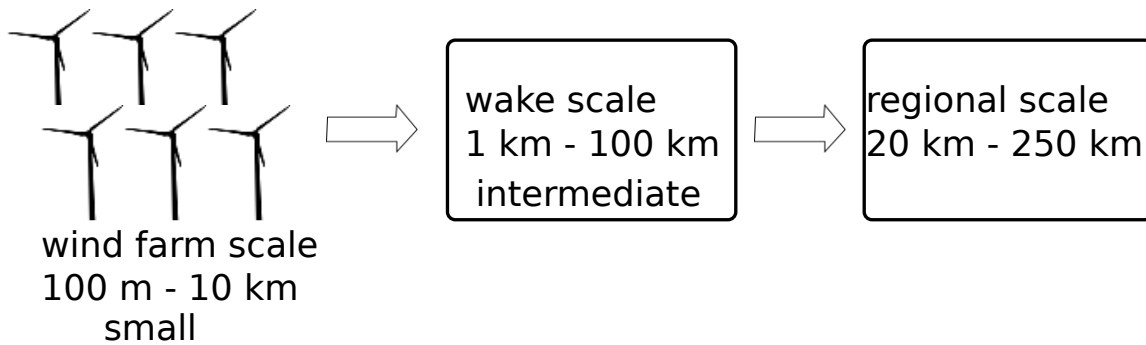


**Figure 4:** The bottom-up approach of this PhD thesis. The WFP of FITCH et al. (2012) is evaluated on a wind farm and wake scale before the impacts on the regional climate are investigated. (The wind turbine icon is taken from <https://svg-clipart.com/white/Ta0k2H4-wind-turbine-clipart>.)

This study evaluates the impacts of the WFP of FITCH et al. (2012) on the MABL at wind farm (100 m – 10 km) and wake (1 km – 100 km) scale to provide a sound basis for investigating impacts on the regional scale (20 km – 250 km) as sketched in Fig. 4. Summarized, this thesis starts from an analysis of small-scale processes (wind farm) via an intermediate scale (wake) to an assessment of impacts of offshore wind farms on the regional scale. First of all, the TKE of mesoscale simulations above offshore wind farms is compared to airborne measurements as the TKE is driving the vertical fluxes i.e. the wind farm scale. Secondly, we evaluate the impacts of large offshore wind farms in the far-field<sup>1</sup> of offshore wind farms i.e. the wake scale. Based on these

<sup>1</sup>By far-field we refer throughout the whole manuscript to the area 5 km and more downwind of a

evaluation results it is possible to discuss potential impacts of offshore wind farms on the regional scale - the largest scale considered in this thesis (Fig. 4). More specifically, we try to answer the following questions:

- How to configure the WFP of FITCH et al. (2012) and the driving mesoscale model to represent the impact of offshore wind farms on TKE and wind speed above wind farms?
- Is it possible to correctly simulate the far-field of large offshore wind farms with the setup obtained above?
- What are the micrometeorological and regional climate impacts of offshore wind farms?

In chapter 2 we describe the aircraft measurements and the simulations used to answer the questions pointed out above. The first two questions are treated in the chapters 3 and 4 to have a sound basis for the discussion about potential regional climate impacts of offshore wind farms on the MABL and the land located downwind of large offshore wind farm clusters (chapter 5).

## 2 Dataset and method

This chapter presents the data we used for analyzing and evaluating our simulations, including aircraft measurements, synthetic aperture radar (SAR) data, ground-based observations and reanalysis data (sections 2.1, 2.2, 2.3 and 2.4). This is followed by an explanation of the WFP of FITCH et al. (2012) (section 2.5), with a description of the driving mesoscale model (section 2.6). An overview of the wind farms implemented in the mesoscale model is given in section 2.7. This chapter is based on the data and method descriptions as presented in SIEDERSLEBEN et al. (2018a, 2019).

### 2.1 Aircraft observations

This section presents aircraft observations that were executed with the aircraft Dornier 128-6, operated by the TU Braunschweig. Three kinds of aircraft observation were conducted within the framework of this study: vertical profiles upwind of offshore wind farms (section 2.1.2), the measurements recorded within the far-field of wind farms (section 2.1.3) and flights performed above wind farms (section 2.1.4). The uncertainties in the aircraft measurements are explained in section 2.1.1.

#### 2.1.1 Uncertainties in the aircraft measurements

The aircraft measurements have two kinds of errors - a systematic and a relative error. The systematic error is rooted in the accuracy of the sensor itself. The temperature sensor has an accuracy of 0.2 K (CORSMEIER et al. 2001), and the wind speed measurements an accuracy of 0.5 m s<sup>-1</sup> with a resolution of 0.08 m s<sup>-1</sup> (BRÜMMER et al. 2003). The relative error is rooted in the size of the eddies of the atmosphere and, hence, the measurement strategy, as the error is a direct function of the sampling length (MANN and LENSCHOW 1994). The airborne measurements are area-averaged over 300 and 3000 data points for the climb flights and for the horizontal flight patterns corresponding to 30 m and 2 km, respectively. By averaging over different length scales we systemically under- or overestimate the turbulent values and standard deviations of temperature and wind speed. Following MANN and LENSCHOW (1994), we have a relative error of 10 % during the climb flights and 1 % during the horizontal flight patterns (i.e. above and downwind of the wind farms) for the wind speed measurements (PLATIS et al. 2018). The temperature observations have a relative error of 0.015 K during the climb flight. As we use area averages in our data analysis to investigate the spatial variation of temperature and wind measurement, the relative error is applicable. The corresponding Gaussian error propagation for the wind direction is  $\pm 3^\circ$ .

#### 2.1.2 Vertical profiles

To be aware of the atmospheric flow conditions and to provide a sound basis for the model evaluation, the aircraft probed the atmosphere in the vicinity of the wind farms

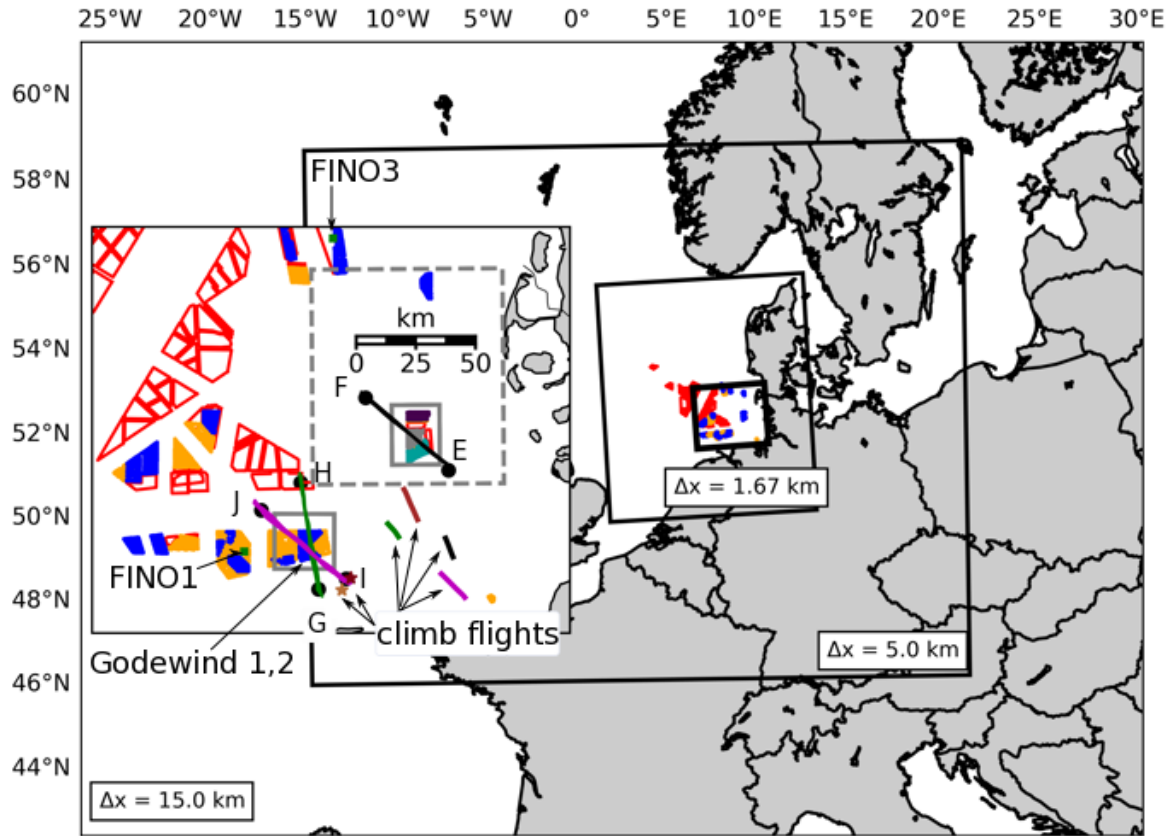


**Figure 5:** Locations of WRF domains and wind farms at the North Sea. A close-up on the German Bight shows the wind farms of interest framed with gray rectangles and the flight tracks above the wind farms in black, green and magenta, corresponding to the measurements executed on 09 August 2017, 14 and 15 October 2017, respectively. All measurements over the wind farms have a start and end point indicated with a capital letter for better orientation in Fig. 14, 16 and 18. Blue wind farms are in use, orange wind farms are approved or under construction according to plans in 2017, wind farms plotted as red polygons are potential areas for wind farms according to plans in 2015. The gray dashed rectangle highlights the location of the observations executed on 10 September 2016 with the wind farms Meerwind Sued Ost (gray), OWP Nordsee Ost (green) and Amrumbank West (purple) shown in detail in Fig. 6. The thick lines indicate the locations of the climb flights, whereby the coloring corresponds to the coloring of the flight tracks over the wind farms, except the light red and red star showing the locations of the two additional profiles recorded before and after the two additional flight legs on 15 October 2017 and the brown thick line indicating the location of climb flight on 10 September 2016. A detailed look at the wind turbine distribution of the wind farms of interest is provided in Fig. 7. The wind turbine location data was provided by the German Federal Maritime and Hydrographic Agency (BSH) and BUNDESNETZAGENTUR (2017).

of interest to obtain vertical profiles of the atmosphere during each observation. In this thesis, we present six vertical profiles in detail, the locations of these profiles are shown in Fig. 5 and the corresponding dates and times are given in Table 1.

**Table 1:** Date and start time of climb flights in the vicinity of wind farms. The corresponding locations are shown in Fig. 5

Date	Time (UTC)	color, marker in Fig. 5
10 September 2016	08:00	brown thick line
09 August 2017	13:22	black thick line
14 October 2017	13:22	green thick line
15 October 2017	07:17	magenta thick line
15 October 2017	9:23	light red star
15 October 2017	10:18	red star

### 2.1.3 In the far-field of offshore wind farms

The research aircraft flew two different flight patterns to capture the vertical and horizontal extent of wakes in the far-field. In particular, we will focus on measurements recorded on 10 September 2016, all other flights with such a pattern are listed in Table 2. The horizontal flight pattern on 10 September 2016 is shown in Fig. 6 with flight legs perpendicular to the mean wind speed at hub height equal to 90 m AMSL. The first flight leg was flown 5 km downwind of the wind farm. Four further flight legs 15 km, 25 km, 35 km and 45 km downwind of the wind farms were also flown. Note these measurements took more than 1 hour.

Additionally, the vertical extent of the wake 5 km downwind of the wind farm cluster Amrumbank West was observed on 10 September 2016 by 5 flight legs at 5 different heights along the cross-section A-B (Fig. 6): 60 m, 90 m, 120 m, 150 m and 220 m AMSL. The vertical flight pattern took place from 1000 UTC to 1100 UTC, we present this data in chapter 4.

### 2.1.4 Above offshore wind farms

Three sets of aircraft observations were executed above offshore wind farms, labeled as case I, II, and III, summarized in Table 3. The aircraft observations were conducted on 09 August (case I), 14 October (case II) and 15 October 2017 (case III) at two different wind farm clusters (Fig. 5, Fig. 7). The observations on 09 August 2017 and 14 October 2017 started at  $\approx 14:15$  UTC and lasted 35 minutes and 52 minutes. The measurements on 15 October 2017 took place from 14:15 UTC to 09:21 UTC and 09:52 UTC to 10:17 UTC. The different observational periods are summarized in Table 3.

All aircraft measurements have the same pattern. Before we started the measurements over the wind farms, the aircraft profiled the MABL in the vicinity of the wind farms of interest, followed by several flights over the wind farms orientated perpendicular to the large scale synoptic forcing. During all observations, the aircraft overflew the wind farm at least four times. Case study III included two additional measure-

**Table 2:** Overview of flights conducted within the WIPAFF project downwind of large offshore wind farms. The numbering of the aircraft measurements corresponds to the numbering in Fig. 29 and in Fig. 30. The letters A and G indicate the measurement location; A refers to the wind farm cluster consisting of Amrumbank West, Meerwind Süd Ost and Nordsee Ost and G for the wind farm Godewind. The locations of these wind farms are indicated in Fig. 5. The column indicated with *wsp*, shows the measured wind speed at hub height according to Fig. 29. The sixth and seventh column indicate whether the wind farms had an impact on temperature or humidity at hub height downwind. The atmospheric stability during each measurement is shown in the last column according to the potential temperature gradient within the rotor area shown in Fig. 29. Observations where wind farms had an impact on the atmosphere are listed at the beginning of the table. The observations suggest that a wind speed over  $6 \text{ m s}^{-1}$  and stable conditions are a sufficient constraint to observe warming or cooling. The cases fulfilling these criteria are the cases (a-k). The reasons why no warming or cooling was observed in the cases f, j and k is discussed in chapter 4 section 4.4.2.

Index	Date	Time (UTC)	wind farm	<i>wsp</i> ( $\text{m s}^{-1}$ )	$\Theta$	humidity	stability
a)	06 September 2016	14:13 - 17:20	A	6-9	warming	drying	stable
b)	10 September 2016	07:30 - 11:15	A	6.5	warming	drying	stable
c)	11 April 2017	14:04 - 18:00	G	12	warming	drying	stable
d)	08 August 2017	08:35 - 12:35	A	7	warming	drying	stable
e)	17 August 2017	06:06 - 10:10	A	10	warming	drying	stable
f)	30 March 2017	13:57 - 17:02	G	11.5	none	humidification	stable
g)	17 May 2017	15:16 - 19:22	A	13.5	cooling	none	stable
h)	27 May 2017	07:57 - 11:58	A	8.2	cooling	none	stable
i)	27 May 2017	12:39 - 16:36	A	11	cooling	drying	stable
j)	31 March 2017	13:36 - 17:00	G	11	none	none	stable
k)	24 May 2017	11:40 - 09:34	G	7.5	none	none	stable
l)	07 September 2016	07:30 - 10:45	A	5.5	none	none	stable
m)	07 September 2016	12:00 - 14:00	A	4.5	none	none	stable
n)	08 September 2016	08:30 - 12:30	A	7	none	none	unclear
o)	09 September 2016	13:42 - 17:17	A and G	7	none	none	neutral
p)	10 September 2016	12:15 - 16:00	A	4.5	none	none	stable
q)	05 April 2017	13:42 - 14:34	G	12	none	none	neutral
r)	06 April 2017	13:29 - 16:22	G	8	none	none	neutral
s)	09 April 2017	11:36 - 14:07	G	4	none	none	stable
t)	09 April 2017	14:32 - 18:12	G	3	none	none	stable
u)	13 April 2017	11:35 - 15:39	G	13	none	none	neutral
v)	23 May 2017	09:00 - 10:30	G	5	none	none	stable
w)	23 May 2017	11:18 - 15:00	A	11.5	none	none	unclear
x)	01 June 2017	06:55 - 10:54	A	8.0	none	none	neutral
y)	14 August 2017	14:40 - 18:31	A	8.8	none	none	neutral
z)	15 October 2017	11:52 - 15:35	G	8.5	none	none	neutral

ments over the wind farms of interest conducted 40 min after the first four flight legs (Table 3).

The measurements were executed at two different wind farms (Fig. 5) with two different rotor types (more details in section 2.7). Therefore, different flight heights were necessary - the aircraft flew at 200 m AMSL for case study I and 250 m AMSL

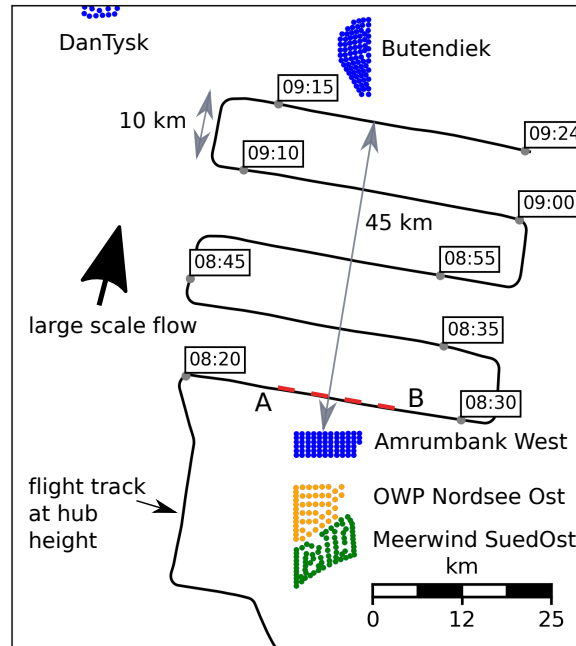


**Figure 6:** The wind farms of interest, the flight track of the research aircraft with time stamps in UTC and the mean wind direction during the field campaign on 10 September 2016. A gray dashed box in Fig. 5 indicates the location of the shown close-up. Every single wind turbine is plotted as a dot and the corresponding wind farms Meerwind SuedOst (MSO, green dots), OWP Nordsee Ost (ONO, orange dots), Amrumbank West (AW), Butendiek and DanTysk are annotated in the Figure. The flight track is indicated with a black solid line. The orientation of the wind direction on 10 September 2016 at 09:00 UTC is denoted by an arrow.

**Table 3:** Location, date and time of aircraft observations above wind farms

Case study	Date	Time (UTC)	number of flight legs	wind farms
I	09 August 2017	14:14 - 14:51	4	Meerwind SuedOst, OWP Nordsee Ost
II	14 October 2017	14:19 - 15:11	4	Godewind 1, 2
III	15 October 2017	8:28 - 9:21	4	Godewind 1, 2
	15 October 2017	9:52 - 10:17	2	Godewind 1, 2

for case study II and III, over the wind farms (Fig. 8) Meerwind Süd Ost (MSO) and OWP Nordsee Ost (ONO), Godewind 1,2 (GW), respectively.

## 2.2 Synthetic Aperture Radar Data (SAR)

Satellite data from Sentinel-1A is used to evaluate the orientation of the simulated wakes for the 14 October 2017. Literature published in the past has shown that Synthetic Aperture Radar (SAR) is a powerful tool to detect wakes offshore (e.g., CHRISTIANSEN and HASAGER 2005; LI et al. 2014; HASAGER et al. 2005, 2015; DJATH et al. 2018), due the reduced surface roughness within the wakes, rooted in the wind speed deficit downwind of offshore wind farms, resulting in turn in an altered backscattering at the sea surface. By applying post-processing methods as suggested by DJATH et al. (2018), the back scattered signal can be used to calculate the wind speed at 10 m height.

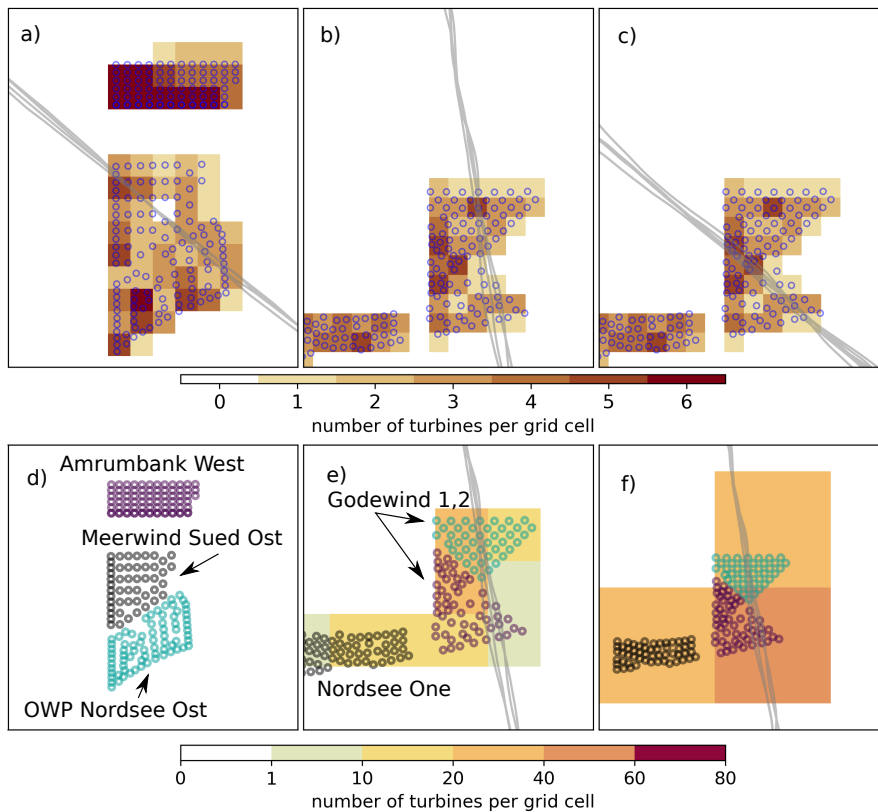


**Figure 7:** The number of wind turbines within one grid cell in colored contours for the wind farms (a) Meerwind Sued Ost and OWP Nordsee Ost and (b-c) Godewind 1, 2 for the control simulations (CN-TRa, CNTRb, CNTRc). The size of the contour areas corresponds to the size of the horizontal model grid. The circles denote the exact locations of the single wind turbines whereby the wind turbines are colored according to the wind farm they belong to in (d-f), additionally (e-f) show the horizontal grid with 5 km and 16 km resolution for the sensitivity studies: DX5, DX16, noTKESourceDX5 and noTKESourceDX16. The wind turbines are not colored in (a-c) for better visibility of the wind turbine density. The gray lines denote the flight track of the research aircraft.

However, these methods assume neutral wind conditions (VERHOEF et al. 2008), hence, we only use the data of Sentinel-1A taken at 17:17 UTC on 14 October 2014 to evaluate the orientation of the simulated wakes and not the wind speed.

### 2.3 Ground-based observations

To evaluate the simulations for the 10 September 2016 we use ground-based observations of the measurement towers FINO1 and FINO3. These towers are used to assess the lower marine atmosphere, up- and downwind of the wind farms of interest (location of towers is shown in Fig. 5) as the aircraft can not measure below 60 m AMSL. In contrast to the sounding of Norderney, FINO1 and FINO3 have the advantage that they are not influenced by the land surface and, hence, give a representative stratification of the marine boundary layer below hub height. Moreover, FINO3 was not influenced by any wakes due to the south-westerly winds on 10 September 2016. In contrast,

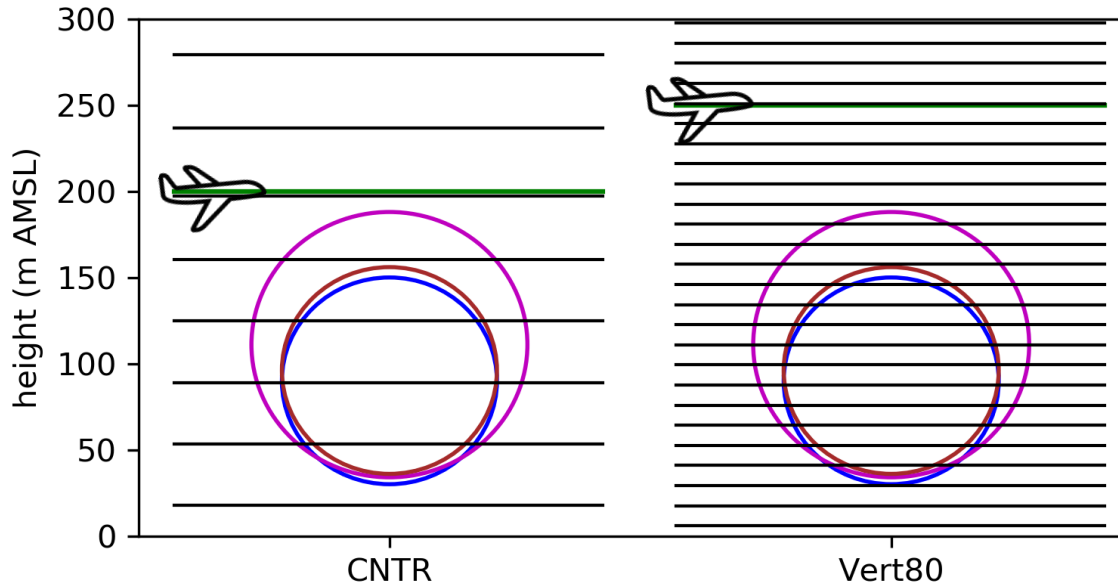


**Figure 8:** Distribution of the vertical levels with height and the levels intersecting with the rotor areas of the two wind turbine types used in the wind farms as listed in Table 5 for the CNTR and the Vert80 simulation. The rotor areas of the wind turbine SIEMENS-SWT-6.0-154 and SIEMENS SWT 3.6-120 are shown in magenta and blue, respectively. The green lines denote flight heights at 200 m and 250 m AMSL; necessary due to the two different wind turbine types. The aircraft icon is taken from <https://www.trzcacak.rs>.

FINO1 was likely influenced by Borkum Riffgrund 1. Therefore, the temperature and wind measurements at FINO1 have to be used with caution. FINO1 is equipped with five temperature sensors at 33 m, 50 m, 70 m, 90 m and 100 m AMSL, whereas FINO3 has only 3 temperature sensors at 50 m, 70 m, and at 90 m AMSL (NEUMANN et al. 2004). The temperature sensors at FINO1 have an absolute accuracy of 0.5 K (R. Fruehmann 2018, personal communication) and agree relative to each other with an accuracy of  $\pm 0.05$  K (FRUEHMANN 2016). The temperature sensors at FINO3 have an absolute uncertainty of 1.21 K (A. Mark 2018, personal communication).

## 2.4 Reanalysis Data: ECMWF analysis and ERA5 data

We use ECMWF analysis or ERA-interim data to assess the weather on a synoptic scale for all case studies presented in this study. Additionally, both data sets are used to define the lateral and initial boundary conditions of our simulations. ERA5 analysis data is freely available at COPERNICUS CLIMATE CHANGE SERVICE (C3S) (2018) with a horizontal resolution of 0.25 degrees whereas ECMWF analysis data having a grid size of 0.125 degrees and has restricted access.

## 2.5 Wind farm parameterization

In this thesis all simulations use the wind farm parameterization of FITCH et al. (2012). This parameterization acts as an elevated momentum sink for the mean flow and a

source of turbulence, depending on the thrust - and power coefficient  $C_T$  and  $C_P$ . Both coefficients are a function of wind speed and are different for every wind turbine type - an example for the wind turbine type SIEMENS SWT 3.6 120 onshore<sup>1</sup> is shown in Fig. 9. The power coefficient is the electrical power  $P_e$  generated by a wind turbine normalized by the power of the wind:

$$C_P = \frac{P_e}{P_{wind}}. \quad (2)$$

However, the power coefficient can also be used to describe the rate of loss of kinetic energy from the atmosphere associated with the conversion of kinetic into electrical energy (FITCH et al. 2012). The thrust coefficient  $C_T$  describes the total fraction of energy that is extracted by a single wind turbine from the atmosphere (FITCH et al. 2012). The amount of energy that is not converted into electrical energy is lost due to frictional and electrical losses and non-productive drag. In the parameterization of FITCH et al. (2012) frictional and electrical losses are neglected, hence, all losses are caused by non-productive drag, that in turn produces turbulence. Consequently, the difference between  $C_T$  and  $C_P$  describes the fraction of energy converted into TKE.

More specifically, the amount of TKE added to the model is:

$$\frac{\partial TKE_{ijk}}{\partial t} = \frac{\frac{1}{2} N_t^{ij} C_{TKE} V_{ijk}^3 A_{ijk}}{z_{k+1} - z_k} \quad (3)$$

$$C_{TKE} = C_T(V_H) - C_P(V_H) \quad (4)$$

whereby  $C_{TKE}$  describes the fraction of energy converted into TKE. Equation 3 is formulated for a Cartesian coordinate system with the indexes  $i, j, k$  corresponding to the directions  $x, y, z$ , that, in turn, is equal to the geographic directions West-East, South-North, and the vertical axis with  $k=0$  the level closest to the ground. The variable  $N^{ij}$  describes the wind turbine density within a grid cell  $i, j$  having the units  $m^{-2}$ ;  $V_{ijk}$  is the horizontal wind speed at grid cell  $ijk$ ;  $A_{ijk}$  is the rotor area between the two vertical levels  $k$  and  $k + 1$ , at a height  $z_k$  and  $z_{k+1}$ , and  $V_H$  the horizontal wind speed at hub height. Consequently, the rate of change in TKE is highest for high wind speeds, a large number of wind turbines within one grid cell and a large difference between the power and thrust coefficient.

## 2.6 Numerical Setup

In this thesis, we present simulations covering 10 September 2016, 09 August 2017 and 14, 15 October 2017. For all these days we performed simulations using the control configurations as described in section 2.6.1. The control simulations covering the 09 August 2017 and 14, 15 October 2017 are named CNTRa, CNTRb and CNTRc

---

<sup>1</sup>data available at: <http://www.wind-turbine-models.com/turbines/646-siemens-swt-3.6-120-onshore>, accessed on 5th December 2017

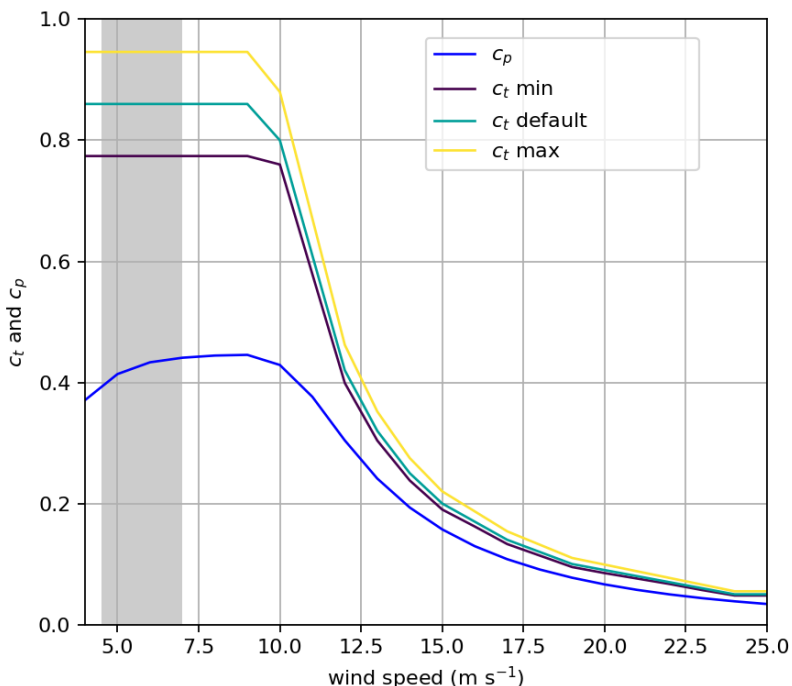


**Figure 9:** Thrust- and power coefficient  $c_t$  and  $c_p$  of the wind turbine SIEMENS SWT 3.6 120 onshore. The  $c_p$  values used in the sensitivity experiments  $c_p$  min and max are shown in purple and yellow.

throughout this thesis. Additionally, we executed simulations with different setups to investigate the sensitivity of our simulations with a focus on 14 October 2017. The different configurations of the sensitivity simulations are presented in section 2.6.2.

### 2.6.1 Control configuration

All simulations are conducted with the Weather Research & Forecasting Model WRF, version 3.8.1 (ARW, SKAMAROCK et al. (2008)). The model uses three domains with a horizontal grid size of 15 km, 5 km and 1.67 km, respectively. The location of the two way nested domains are shown in Fig. 5. The time step is 60 s for the coarsest domain, 20 s and 5 s for the following domains, respectively.

The initial and lateral boundary conditions are defined with operational ECMWF analysis data in 6 hourly intervals for the simulations covering the 10 September 2016, as we obtained best results with this data for this specific day. For all other simulations, we use ERA-interim reanalysis data (COPERNICUS CLIMATE CHANGE SERVICE (C3S) 2018) with a resolution of 0.25 degree in 6 hourly intervals<sup>2</sup>.

The SST affects the stratification of the atmosphere, hence, mesoscale simulations with refined SST data (such as that provided via the Operational Sea Surface Temperature and Sea Ice Analysis (OSTIA) product), can improve mesoscale simulations (SHIMADA et al. 2015). However, the SST data from OSTIA for the case studies

<sup>2</sup>ERA-INTERIM reanalysis data is freely available via the Copernicus Climate Change Service Climate Data Store, hence, the majority of boundary conditions were provided by ERA-interim data

presented here only differ marginally from the SST data provided from ECMWF analysis or the ERA5 data. Therefore, we did not update the SST using an advanced SST dataset. HAHMANN et al. (2015) pointed out that boundary layer winds over land have a spin-up time larger than 12 hours and could, therefore, influence offshore boundary layer wind climatology. Therefore, our model is initialized at 1200 UTC the day before or in the night before the observations at 00 UTC and integrated over 24 hours (i.e., to have a spin-up of more than 12 hours). This is true for all simulations, except for the simulation conducted for the 15 October 2017, here we only have a spin-up time of nine hours as the additional 6 hours spin-up time showed no improvement considering the vertical representation of the atmosphere.

In the control configuration, we use a vertical spacing of 35 m in the lowest 200 m and increasing to 100 m at 1000 m above mean sea level (AMSL) corresponding to one vertical level below the rotor area and three within the rotor area for the wind turbine type installed at the wind farms MSO and ONO (Fig. 8). Four vertical levels are located within the rotor area for the wind farm GW (Fig. 8) due to the larger rotor area.

The following parameterizations are used in all three domains: the WRF double-moment 6-class cloud microphysics scheme (WDMS; LIM and HONG (2010)), the Rapid Radiative Transfer Model for GCM (RRTMG) scheme for short- and longwave radiation (IACONO et al. 2008), the Noah land surface model (CHEN and DUDHIA 2001) and the Mellor-Yamada-Nakanishi-Niino (MYNN) boundary layer parameterization (NAKANISHI and NIINO 2006) interacting with the WFP, as described in section 2.5. In the two innermost domains convection is resolved explicitly, only the first domain uses the cumulus parameterization of KAIN (2004).

### 2.6.2 Sensitivity configurations

Sensitivity simulations were performed for two days: 10 September 2016 and 14 October 2017. The simulations covering 10 September 2016 focus on the uncertainty of the wake simulations (section 4.3 in chapter 4) rooted in the estimated thrust and power coefficients of the simulated wind turbines. In contrast, the sensitivity studies conducted for the 14 October 2017 address the question whether an additional TKE source in a WFP is needed to represent the impact of offshore wind farms during stable conditions on the MABL. All sensitivity studies executed for 14 October 2017 are listed in Table 4.

LEE and LUNDQUIST (2017) obtained the best results with 80 vertical levels - equal to a vertical spacing of 12 m below 400 m AMSL. Therefore, we tested the sensitivity of our results using the vertical levels of LEE and LUNDQUIST (2017) - equal to three full levels below and ten full levels within the rotor area for the wind farms MSO, ONO and two full levels and 13 full levels within the rotor area for the wind farms GW

(Fig. 8).

The vertical levels of LEE and LUNDQUIST (2017) demand smaller time steps due to the higher resolution. Therefore, we use 10 s, 3.33 s and 0.67 s corresponding to the three domains. We named the simulations using 80 vertical levels Vert80.

The sensitivity of our results with respect to the horizontal grid size was tested with simulations of 5 km and 16 km horizontal resolution, respectively. Consequently, the number of turbines within one grid cell changes as it is shown in Fig. 7e-f. We obtained best results using a horizontal grid size of 1.67 km.

Recently, some published studies (e.g., ABKAR and PORTÉ-AGEL 2015; ERIKSSON et al. 2015; VANDERWENDE et al. 2016; PAN et al. 2018) suggested that the mixing induced by the WFP of FITCH et al. (2012) is too high due to the added TKE into the model (see equation 3). Therefore, we tested the sensitivity of our simulations by switching the TKE source off. Three simulations were performed using a horizontal grid spacing of 1.67 km, 5 km and 16 km with a disabled TKE source (noTKEsource, DX5noTKEsource, DX16noTKEsource). As we expect a simulation with more vertical levels to resolve more vertical shear, we performed additionally a simulation using 80 vertical levels with a grid size of 1.67 km and no TKE source (Vert80noTKEsource).

Since WRF version 3.8.1 TKE advection can be activated in the boundary scheme of NAKANISHI and NIINO (2004). In previously published studies (e.g., MANGARA et al. 2019) this option was used. Therefore, we tested the sensitivity of our results with respect to this option.

**Table 4:** Overview of performed numerical simulations and parameter choices for the sensitivity experiments.

simulation	horz. grid size (km)	vertical levels	TKE source	TKE advection	thrust coefficient
CNTRa	16, 5, 1.67	50	on	off	default
CNTRb	16, 5, 1.67	50	on	off	default
CNTRc	16, 5, 1.67	50	on	off	default
DX5	16, 5	50	on	off	default
DX16	16	50	on	off	default
Vert80	16, 5, 1.67	80	on	off	default
noTKEsource	16, 5, 1.67	50	off	off	default
noTKEsourceDX5	16, 5	50	off	off	default
noTKEsourceDX16	16	50	off	off	default
ADV	16, 5, 1.67	50	off	on	default
PERTMIN	16, 5, 1.67	50	on	off	+10 %
PERTMAX	16, 5, 1.67	50	on	off	-10 %

## 2.7 Wind farms implemented in the numerical model

The aircraft measurements and simulations presented in this study focus on the wind farms Amrumbank West (AW), OWP Nordsee One (ONO), Meerwind SuedOst (MSO) and Godewind 1,2 (GW) (Fig. 5, Fig. 6), hence only these wind farms are presented

in detail. For all other wind farms installed at the North Sea, the interested reader is referred to BUNDESNETZAGENTUR (2017).

Within these wind farms, three different types of wind turbines are installed: At the wind farms AW and at MSO the wind turbine SIEMENS SWT 3.6-120, having a nominated power of 3.6 MW, a rotor diameter of 120 m and a hub height of 90 m, resulting in a rotor top of 150 m (Fig. 8). The wind turbines at the wind farms ONO and GW (Fig. 6, Fig. 7) have a nominated power of 6.2 MW and 6.0 MW with a hub height of  $\approx 96$  m and 110 m, and a rotor diameter of 126 m and 154 m, resulting in a rotor top of 159 m and 187 m, respectively.

For approved and wind turbines currently under construction, i.e. wind turbines colored orange in Fig. 5 (April 2018), we assumed the same wind turbine type as installed at AW, the SIEMENS SWT 3.6-120. The locations of these wind turbines were made available by the German Federal Maritime and Hydrographic Agency (BSH) and BUNDESNETZAGENTUR (2017). For potential areas of future wind farms (i.e. red polygons in Fig. 5), the same turbine spacing as at the wind farm AW was assumed - one of the highest wind turbine densities existing at the German Bight.

**Table 5:** Wind turbine types installed in the model according to the data of the BUNDESNETZAGENTUR (2017)

wind farm	wind turbine type	hub height (m)	diameter (m)
Godewind	SIEMENS SWT-6.0-154	110	154
Amrumbank West	SIEMENS SWT 3.6-120	90	120
Meerwind SuedOst	SIEMENS SWT 3.6-120	90	120
OWP Nordsee Ost	SENVION 6.2	95.4-97.04	126

Public information on turbine thrust - and power coefficients is not widely available, and so we also explored the sensitivity of our results to these parameters. We altered the estimated thrust coefficient by  $\pm 10$  %, resulting in two simulations (PERTMIN, PERTMAX) that are expected to introduce more and less TKE into the model than the CNTRb simulation. The results are presented in section 3.3.4. Sensitivity simulations of the same kind were conducted for the 10 September 2017 case study (section 4.3) to investigate the impact of this uncertainty on the far-field.

## 2.8 Energy budget framework

In chapter 5 this work discusses potential impacts of offshore wind farms on the regional climate. Therefore, this section presents a brief overview of the atmospheric energy budget.

According to PORTER et al. (2011) the rate of energy change in a vertical column

of the atmosphere is:

$$\frac{\partial}{\partial t} \frac{1}{g} \int_{p_{top}}^{p_s} (c_p T + \phi + Lq + k) dp = F_{RAD} + F_{SFC} + F_{WALL}, \quad (5)$$

where  $c_p$  is the specific heat capacity of air at constant pressure (1005.7 J K<sup>-1</sup>),  $\phi$  the geopotential,  $L$  the latent heat that is released in case of evaporation (2.501 x 10<sup>6</sup> J kg<sup>-1</sup>) and  $q$  the specific humidity. The vertical column is integrated from the surface pressure  $p_s$  to the top of the atmosphere  $p_{top}$  (in case of a model data analysis  $p_{top}$  refers to the highest pressure level of the model). Following equation 5, the rate of energy change in the vertical column is determined by the radiation budget at the top of the atmosphere  $F_{RAD}$ , and at the surface  $F_{SFC}$  and the divergence of energy within the column  $F_{WALL}$ .

The radiation budget  $F_{RAD}$  at the top of the atmosphere is the difference between the net short- and longwave radiation:

$$F_{RAD} = F_{SW} - F_{LW}. \quad (6)$$

At the surface (i.e. at  $p_{sfc}$ )  $F_{SFC}$  can be expanded to:

$$F_{SFC} = SW_{SFC} + LW_{SFC} + Q_H + Q_E \quad (7)$$

where  $SW_{SFC}$  and  $LW_{SFC}$  is the net short- and longwave radiation at the surface. The third term  $Q_H$  is the sensible heat flux and  $Q_E$  the latent heat flux.

The divergence of energy  $F_{WALL}$  within a vertical column can be written as:

$$F_{WALL} = -\nabla \frac{1}{g} \int_{p_{top}}^{p_s} (c_p T + \phi + Lq + k) \vec{v} dp, \quad (8)$$

where  $\vec{v}$  is the horizontal velocity vector - vertical advection from space and through the surface is physical not possible.

A permanent change in the forcing terms on the right-hand side of equation 5 is equal to a change in the regional climate. Therefore, we are interested in whether offshore wind farms can impact the terms on the right-hand side of equation 5. To simplify the analysis, we extend the vertical column such that the whole wake area of all wind farms is within the vertical column, allowing us to neglect  $F_{WALL}$ . Consequently, energy budget changes are possible due to altered radiation budgets at the top and the bottom of the atmosphere and due to changes in the latent and sensible heat flux at the surface.

### 3 Wind speed and TKE above offshore wind farms

The turbulent vertical momentum transport above large offshore wind farms determines the wake length and the efficiency of large offshore wind farms. As it is unclear whether turbulent kinetic energy (TKE) has to be actively added when wind farms are parameterized in mesoscale models, this work tries to find the ideal WFP configuration of FITCH et al. (2012) in combination with the driving mesoscale model (Weather Research and Forecasting model, WRF) to simulate the impact of large offshore wind farms on the TKE and the wind speed above offshore wind farms. Therefore, this chapter evaluates the simulated impact of the WFP of FITCH et al. (2012) on the TKE by use of aircraft measurements executed above offshore wind farms on 09 August 2017, 14 and 15 October 2017 as described in section 2.1.4. This evaluation gives a sound basis for investing the far-field of offshore wind farms in chapter 4. The results shown in this chapter are under review in *Geoscientific Model Development Discussion* (SIEDERSLEBEN et al. 2019).

#### 3.1 Observations

Here we use ERA5 data to provide overviews of the synoptic situations before and during each case study (section 3.1.1) (COPERNICUS CLIMATE CHANGE SERVICE (C3S) 2018). Additionally, the vertical structure of the atmosphere is discussed by the use of climb flight data (for details see chapter 2 section 2.1.2). Finally, the results of the aircraft measurements over the wind farms for the three case studies are described in section 3.1.2 and 3.1.3.

##### 3.1.1 Synoptics and mesoscale overview

Case study I was stably stratified with wind from the southwest. On 09 August 2017 at 15:00 UTC, a trough approached the German Bight from the North (Fig. 10a) associated with southwesterly winds of 10-12 m s<sup>-1</sup> at hub height near MSO (Fig. 11a, g). Warm air advection was associated with a stably stratified atmosphere according to the climb flight (Fig. 11g) upwind of the wind farm cluster (Fig. 5, black thick line). Despite the stably stratified atmosphere, the sea surface temperature (SST) was higher than the air temperature close to the surface. At the FINO1 tower, a SST of 292 K was measured,  $\approx 2$  K higher than the air temperature. As expected for summer time, the SST was highest closest to the coast (Fig. 10a).

Case study II was also stably stratified, with stronger winds from the west. On 14 October 2017 at 15:00 UTC, a deep trough located over the Atlantic caused a zonal jet over the North Sea (Fig. 10b) associated with wind speeds of up to 15 m s<sup>-1</sup> at hub height (Fig. 11e) at the location of the climb flight (Fig. 5, green thick line). Due to the stably stratified atmosphere, the wind profile was characterized by strong vertical shear between 30 m AMSL and 190 m AMSL (Fig. 11e), corresponding to the rotor area

limits of the wind farm. According to SAR data, the stably stratified atmosphere was associated with wakes longer than 50 km (Fig. 12a). Long wakes are visible downwind of the wind farms located near the German and Netherlands coasts. Further to the north, around the wind farm Sandbank (see annotation in Fig. 12b) only subtle wakes are visible indicating less favorable conditions for wakes.

Case III also experienced a stably stratified flow with  $10 \text{ m s}^{-1}$  wind speed and southerly wind direction (Fig. 11c, f). On 15 October 2017 (case III) the trough over the Atlantic moved further to the west causing a south-westerly warm air advection, that in turn resulted in a pronounced inversion with a temperature difference of 4 K between 30 m AMSL and 190 m AMSL according to the profile recorded by the aircraft (Fig. 11c, magenta thick line in Fig. 5). Associated with the top of the inversion is a wind speed maximum at  $\approx 190 \text{ m AMSL}$  (Fig. 11f). From previous literature (e.g., SMEDMAN et al. 1997; DÖRENKÄMPER et al. 2015; SVENSSON et al. 2016) we would expect a SST lower than the air temperature close to the sea surface. However, a SST of 288.5 K was measured at FINO1 in contrast to a potential air temperature of 285 K at 50 m AMSL according to the airborne measurements, indicating that the SST was higher than the air temperature. The two additional vertical profiles taken before and after the additional flyovers revealed a destabilization of the atmosphere during the observation (Fig. 11c).

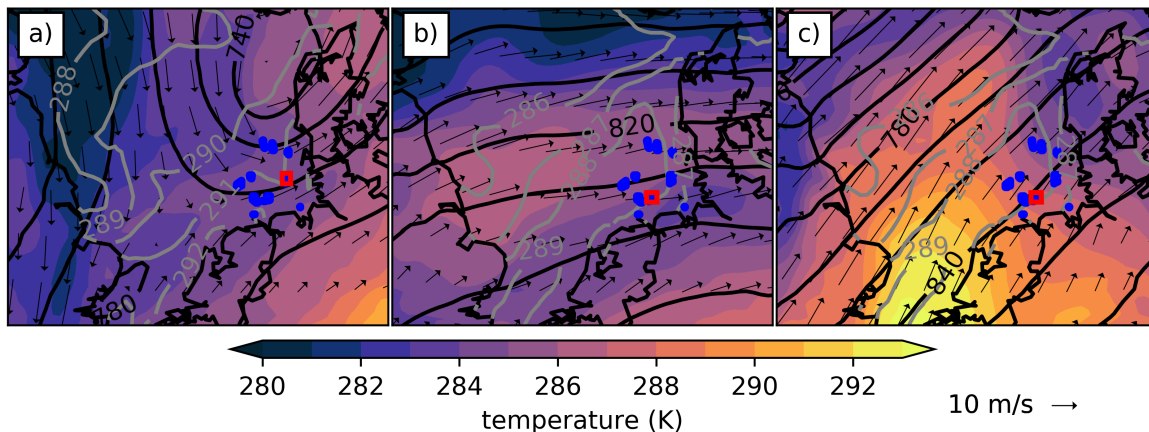


**Figure 10:** ERA5 reanalysis data: Temperature (colored contours (K)) and geopotential height (20-m increments) as black contour lines in 925 hPa for the three case studies as listed at Table 3, at 15:00 UTC 09 August 2017, at 15:00 UTC 14 October 2017 and at 09:00 UTC 15 October 2017 (Table 3). The gray solid contour lines show the SST.

### 3.1.2 Wind speed above and next to the wind farms

For case study I, wind speeds in the order of  $13 \text{ m s}^{-1}$  were observed at 200 m AMSL near the wind farms (Fig. 13a, Fig. 14a). During the four flights above the wind farms, the wind speed varied only by  $\pm 0.5 \text{ m s}^{-1}$  indicating that the weather situation was stationary. However, the variability of the wind speed measurements increases above

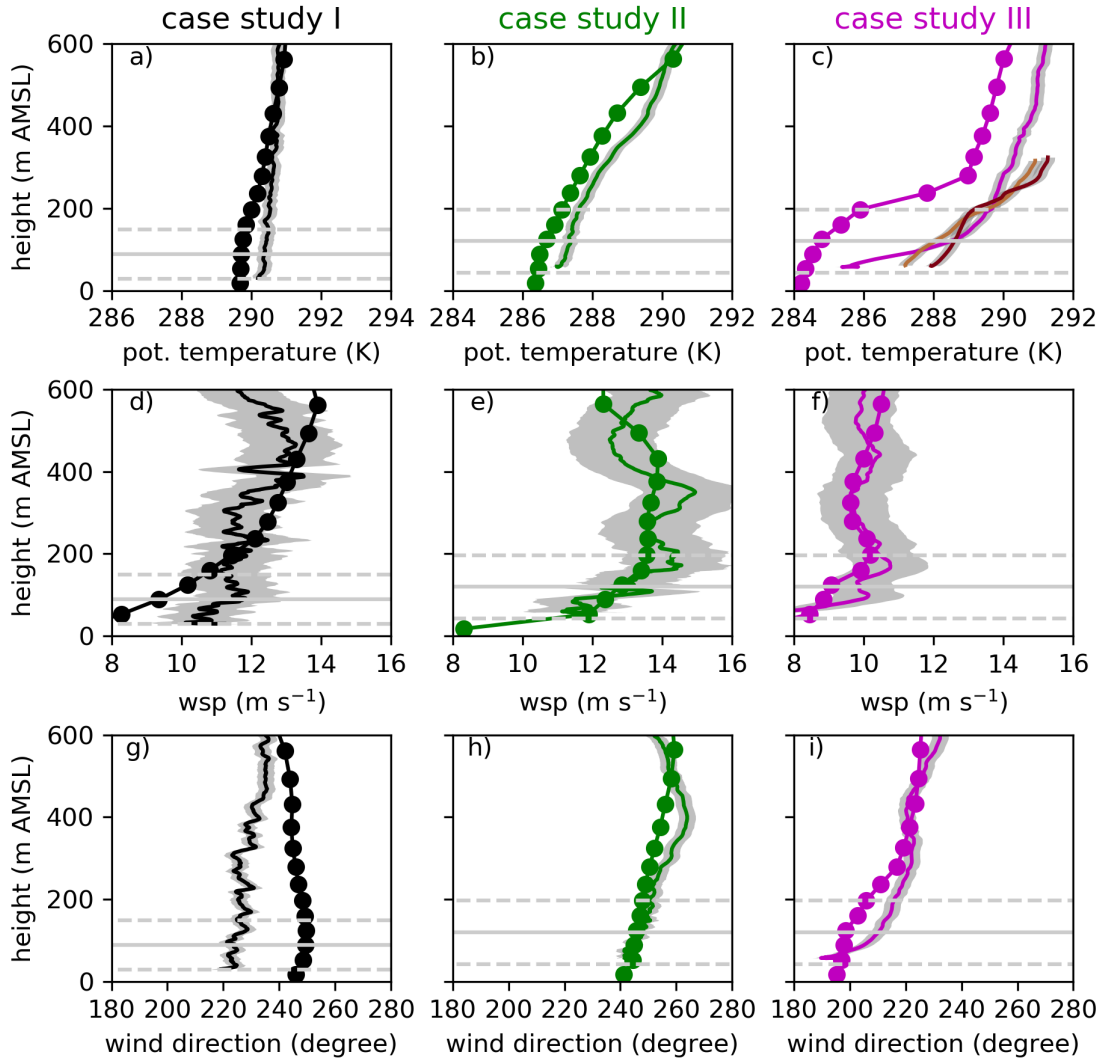


**Figure 11:** Vertical profiles of potential temperature (a-c), wind speed (d-f) and wind direction (g-i) obtained by probing the atmosphere with the research aircraft (solid lines). The interpolated WRF data along the climb flight is shown with the line having the circles on top, whereby each circle represents a vertical level of the WRF control simulation (CNTRa, CNTRb, CNTRc). The gray shadings represent the error bars of the measurements. The dashed and solid gray lines denote the rotor area and the hub height of the wind turbines. As the measurements were conducted at two sites with two different wind turbine types, the height of the hub and rotor areas vary. In (c) two additional vertical profiles are shown (red and light red) that were taken before and after the additional flyovers in case study III, for further details see text. Each column corresponds to one case study, i.e. the column (a, d, g) corresponds to case study I, similar to the coloring of flight tracks in Fig. 5.

the northern edge of the wind farm ONO. At the downwind side of the wind farm, the wind speed decreased in each observation by more than  $1 \text{ m s}^{-1}$ , indicating that the wake of the wind farm extended to a height of 200 m. As the aircraft approached the upwind side of the wind farm (i.e. at  $54.46^\circ \text{N}$  latitude) the wind speed deficit decreased.

During case study II, the distinct wind farm wake was also accompanied by a

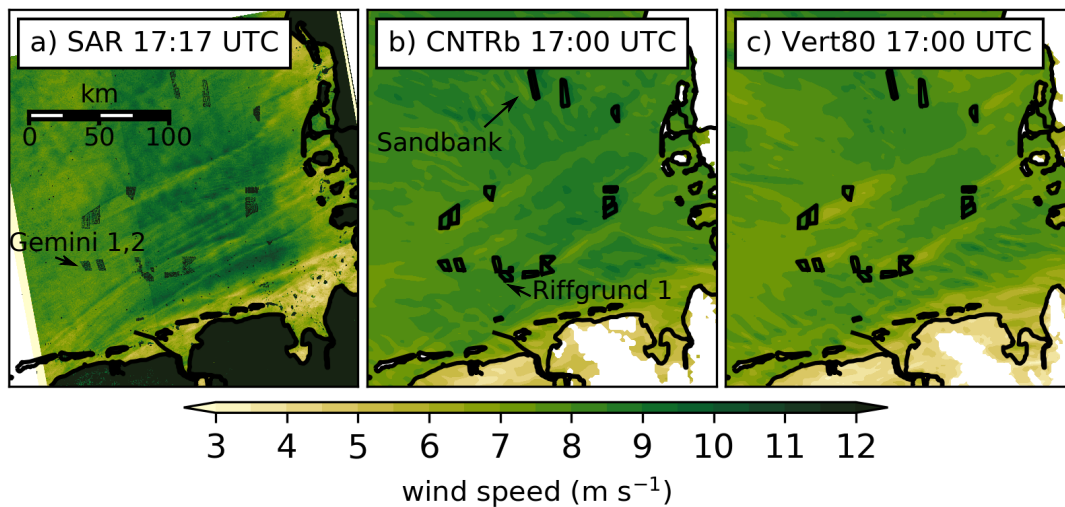


**Figure 12:** A comparison of SAR from Copernicus Sentinel 1A and WRF retrieved wind speed at 17:17 UTC and 17:00 UTC, respectively, on 14 October 2017 (case study II). The SAR data shows the wind speed at 10 m, whereas the model output is taken from the model level closest to 10 m. Therefore, the wind speed in 17 m and in 15 m for the CNTR and Vert80 simulation is shown, respectively.

speed-up around the farm, such as indicated by NYGAARD and HANSEN (2016). We observed a horizontal wind speed of  $\approx 15 \text{ m s}^{-1}$  at 250 m AMSL south of GW and slightly lower wind speeds to the north (Fig. 14b, Fig. 15b). At the southern edge of the wind farm, orientated parallel to the large scale synoptic forcing, the wind speed dropped consistently in all four flight legs by up to  $2 \text{ m s}^{-1}$ , associated with a speed up further south (see annotation of Fig. 14b). We suggest that this acceleration emerges due to an enhanced flow around the wind farm due to the stably stratified atmosphere. Similar to case I, the wind speed showed low variability during the measurements that were performed within a time interval of 50 minutes; the highest variability occurred above the wind farms.

In comparison to the case studies I and II, in III the wind speed was barely influenced by the wind farms GW during the first flight legs. We suggest that this phenomenon is rooted in the strong inversion between 40 m and 180 m AMSL, decoupling the layer the inversion from the surface layer. Consequently, the wind speed measurements showed only weak enhanced variability above the wind farms. However, two additional measurements were taken 40 minutes later. These two flyovers both show an enhanced deceleration above the wind farms, especially the last flight leg (purple line, Fig. 14c). The mean (shown in Fig. 14c) was calculated using only the first four flight legs.

### 3.1.3 TKE above and next to the wind farms

In case I, the airborne measured TKE above the wind farm was a factor of ten higher than in the ambient flow. The TKE above the wind farms MSO and ONO was increased

compared to the surrounding (Fig. 15a, Fig.16a), above the wind farms, the research aircraft measured a TKE of up to  $2.0 \text{ m}^2 \text{ s}^{-2}$ , but  $0.2 \text{ m}^2 \text{ s}^{-2}$  within the undisturbed environment, meaning that the TKE above the wind farms is almost ten times higher 50 m over the rotor top compared to the surrounding environment. This pattern was observed during all four flyovers (Fig. 16a). The mean of all measurements indicates that the highest TKE was observed in the wake region of the wind farm MSO where the shear was greatest (shown in Fig. 14a).

In case II, TKE above the wind farms was a factor of 20 times higher than in the ambient flow. A TKE of up to  $2.5 \text{ m}^2 \text{ s}^{-2}$  was observed at 250 m AMSL above the wind farms GW and  $0.1 \text{ m}^2 \text{ s}^{-2}$  within the background flow (Fig. 15b). The TKE maximum, visible in all four flights (Fig. 16b), corresponds to the southern edge of the wind farms GW - the region with the highest horizontal wind shear (Fig. 14b). In contrast, no TKE maximum can be observed upwind at the northern edge of the farm GW.

In case III, a strong inversion generated a stably stratified environment resulting in the lowest TKE values observed within our three case studies in the background flow and above the wind farm (Fig. 15c and Fig. 16c). Nevertheless, the values of TKE above the wind farms during all six flights were elevated compared to the surroundings. The TKE maximum matched in location with the western edge of the wind farm where the horizontal wind shear was greatest (Fig. 14c) due to the southwesterly background flow. During the last flight leg, the aircraft observed TKE in the order of  $1.6 \text{ m}^2 \text{ s}^{-2}$ , three times higher than in the measurements conducted 40 minutes before (Fig. 16c). This specific flight leg showed also the strongest wind deceleration above the wind farm (Fig. 14c).

In every case, above the wind farm, the aircraft observed values of TKE between five and 20 times larger than the ambient values of TKE.

## 3.2 Control simulations

Herein, we present control simulations for each of the three case studies I, II and III. We start with a comparison of the vertical profiles of the aircraft measurements and the profiles obtained by the simulations. As we want to evaluate the TKE above the wind farms that is in turn highly dependent on wind shear, we compare the wind speed measurements with simulations before we evaluate the simulated TKE in section 3.2.3.

### 3.2.1 Evaluation of the background flow

For case study I, the simulated potential temperature profile and the observations show a weakly stratified atmosphere (Fig. 11a), whereas the model is more stably stratified between 90 m and 250 m AMSL, resulting in stronger vertical wind shear in the model (Fig. 11d). This deviation could be rooted in a dislocation of the incoming trough, causing more westerly winds in the simulations than in the observations.

For case study II, the observed and simulated vertical structure of the atmosphere agree except for a cold bias in the potential temperature. The model predicts a potential temperature profile with a lapse rate similar to the observed one but with a cold bias of 0.5 K. The strong vertical wind shear within the lower rotor area is well represented, so is the wind direction. Consequently, the orientation of the wakes in the SAR satellite observations (Fig. 12a) match with the simulated wakes in Fig. 12b). Note, the SAR image that was taken on 14 October 2017 at 17:17 UTC should be only used to evaluate the orientation of the wakes. The lowest level of the control simulation is at 17 m AMSL. Consequently, interpolating the wind speed to a height of 10 m is difficult. Therefore, we show the simulated wind speed at 17 m in Fig. 12b) for simplicity.

For case study III, the simulations show a less pronounced inversion than the observations (Fig. 11c). This behavior of the model is similar to the case study presented in SIEDERSLEBEN et al. (2018a), where an inversion similar to the one shown in Fig. 11c) developed and the WRF model had also problems to represent the inversion. In this case the inversion is even more pronounced, most likely associated with the proximity of the vertical profile to the coast (Fig. 5, thick magenta line), increasing the challenge for the model to capture the heterogeneity. However, this inversion weakened during the observation but the stratification of the atmosphere in the model did not change with time. Therefore, the simulated profiles before and after additional flights are not shown in Fig. 11c).

### 3.2.2 Impact of wind farm parameterization on wind speed above wind farms

The simulation for case study I generally underestimates the wind speed at 200 m AMSL above and next to the wind farms by up to  $2 \text{ m s}^{-1}$  (Fig. 13a, Fig. 14a). The sharp decrease of  $1 \text{ m s}^{-1}$  within the wake is captured by the model at 15:00 UTC but not at the beginning of the measurements at 14:30 UTC. A weak increase in wind speed similar to the observation is represented above the wind farm (i.e. within the gray shaded area in Fig. 14a), associated with the shorter distance of the upwind edge of the wind farm. A possible explanation for the wind speed bias between model and the observation could be a more unstably stratified atmosphere in the simulations. However, the model adequately represented the stratification of the atmosphere in the vicinity of the wind farms (Fig. 11a). Therefore, we suggest that the atmosphere was more stably stratified to the west during the observation as in the simulations.

The simulations for case study II represent the stationary background flow (i.e. no variance between 14:30 UTC and 15:00 UTC) and the impact of the wind farms GW well. The averaged wind speed matches with the simulated wind speed within  $\pm 0.2 \text{ m s}^{-1}$ , except at the southern edge of the wind farm - there the horizontal wind speed gradient is more pronounced in the observations than in the simulations.

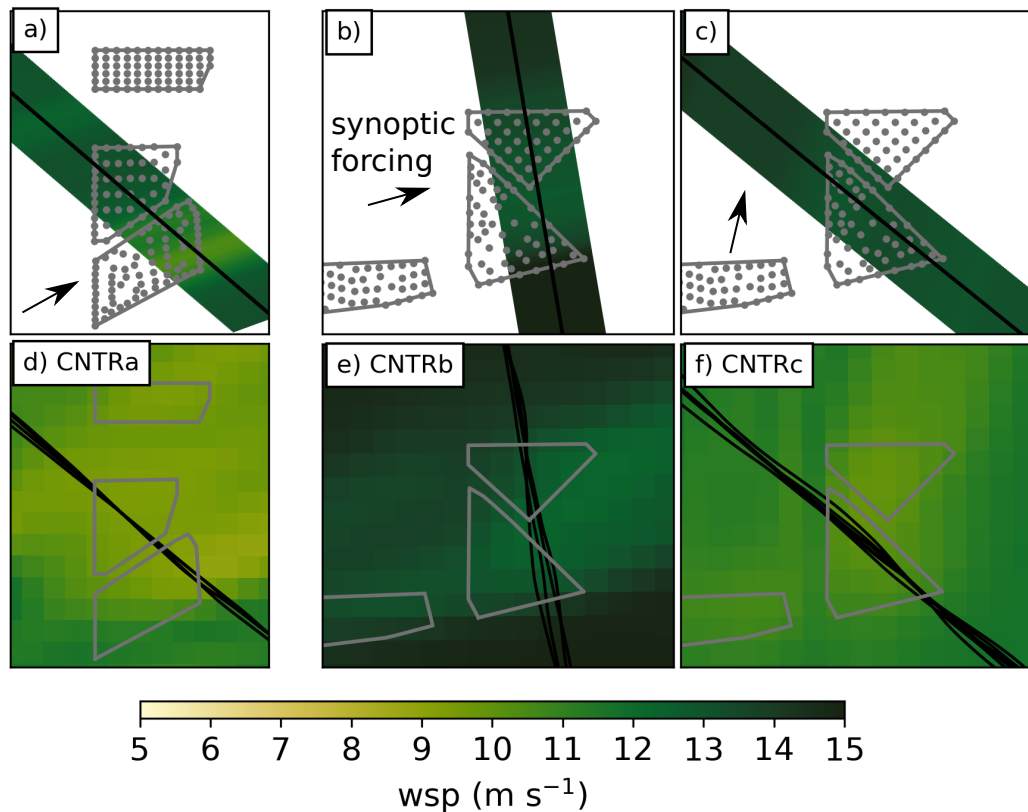


**Figure 13:** Plan view on observed (a-c) and simulated (d-f) horizontal wind speed at 14:30 UTC, 15:00 UTC and 09:00 UTC on 09 August, 14 and 15 October 2017, respectively, horizontal wind speed in colored contours at 200 m AMSL (a, d) and 250 m AMSL (b, c, e, f). Black lines denote the flight path above the wind farms. The observations show the mean of the observed wind speed, similar to Fig. 14a-c). The locations of wind farms and single wind turbines are shown by gray polygons and dots, respectively. Each column corresponds to one case study (i.e. column a,d corresponds to the measurements taken on 09 August 2017).

However, this deviation is likely rooted in the rather coarse horizontal grid size of the model.

The model underestimates the wind speed compared to the measurements conducted during case study III. Above the wind farms, the deviation between simulations and observations are largest for the first four flyovers, indicating a more pronounced impact of the wind farms on the atmosphere in the simulations than in the observations. However, at 10:00 UTC, the observation showed an increased impact on the wind speed above the wind farms similar to simulations with a constant negative bias of  $\approx 2.0 \text{ m s}^{-1}$ .

### 3.2.3 Impact of wind farm parameterization on TKE above wind farms

The increased TKE above the wind farms is captured by the simulations, but not the shape of the TKE profile above the wind farms. For example, in case study I, the WFP simulates a TKE above the wind farms with two peaks (Fig. 15a, Fig. 16a), whereby

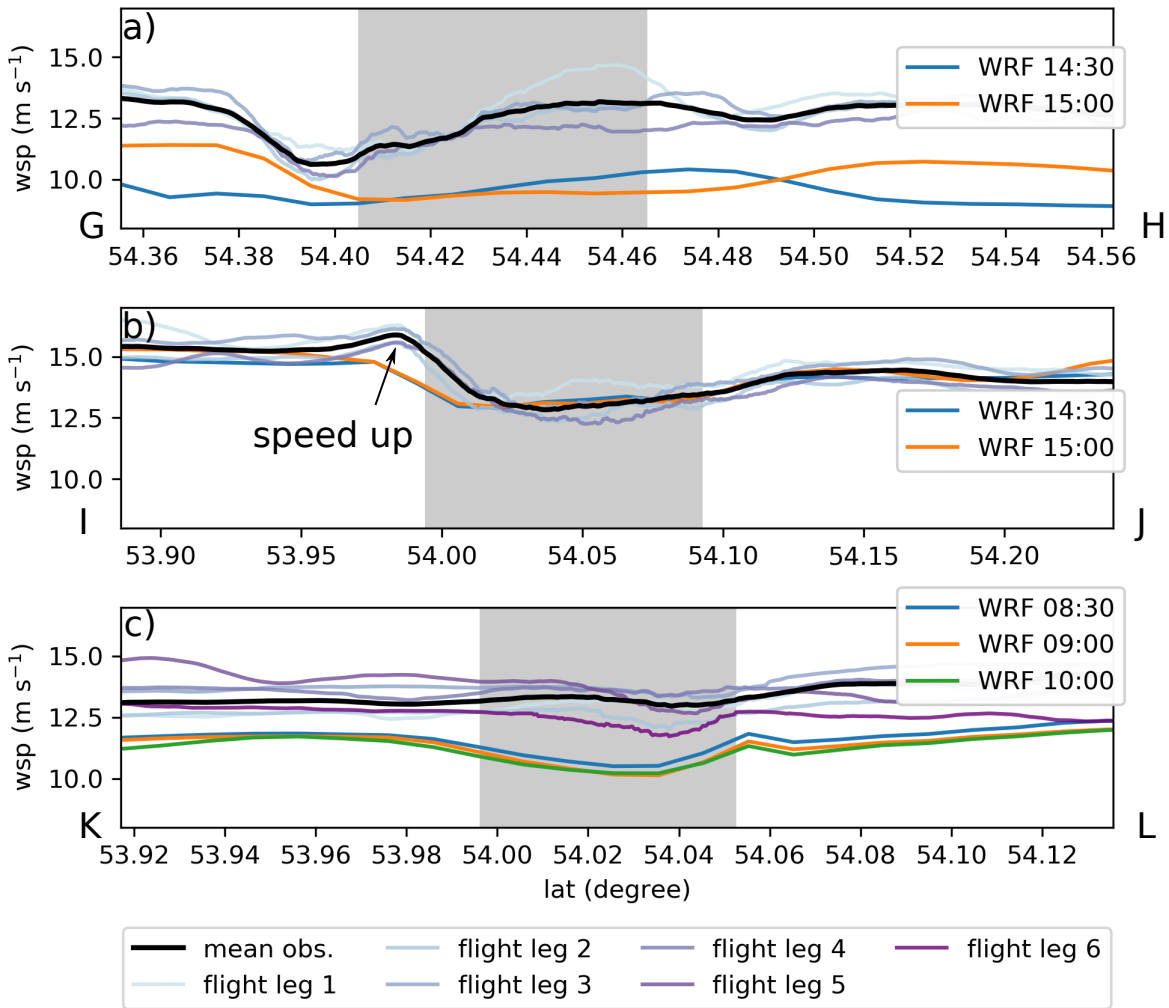


**Figure 14:** Observed (thin blue and purplish lines, the purple amount is increased, the later the flight leg was flown) and simulated wind speed interpolated onto the flight track in blue for the three case studies (a-c) as indicated in Table 3. The black thick line shows the mean of all wind speed measurements above the wind farms similar to the measurements shown in Fig. 13a-c). The gray shaded areas denote the location of the wind farm. The capital letters on the x-axis show the orientation of the axis as indicated in Fig. 5.

the first peak matches with the observed TKE maximum with  $\approx 1.5 \text{ m}^2 \text{ s}^{-2}$ . However, this peak in TKE corresponds in the observations to the southern edge of the wake that developed behind the farm, whereas in the simulations this peak corresponds to the southern edge of the wind farm (Fig. 7a). The second peak at  $54.46^\circ\text{N}$  in simulations with a TKE of  $2.0 \text{ m}^2 \text{ s}^{-2}$  corresponding to the upwind side of the wind farm was not observed.

A similar pattern can be observed for the simulations conducted for 14 October 2017. The TKE maximum at the southern edge of the wind farms is captured by the model (Fig. 15b, Fig. 16b). In contrast, the declining trend of TKE towards the northern edge of the wind farm is interrupted in the model. The TKE of the undis-

turbed flow next to the wind farm is very similar to the observed TKE, increasing the confidence in this simulation.

In contrast to the other case studies, in case study III, the TKE in the observations evolves over time. Initially, the simulated TKE is more than twice as high than the averaged observed TKE above the wind farms,  $1.0 \text{ m}^2 \text{ s}^{-2}$  for the first four flyovers compared to  $2.0 \text{ m}^2 \text{ s}^{-2}$  (Fig. 15c, Fig. 16c). However, 40 minutes later, the measured TKE from the additional two flight legs show a TKE similar to the simulations. Especially, the last flight leg shows a TKE of  $2.0 \text{ m}^2 \text{ s}^{-2}$  at the western edge of the wind farm. This flight leg also has the most pronounced wind speed deficit above the wind farm agreeing best with simulated impact on the horizontal wind speed at 250 m AMSL.

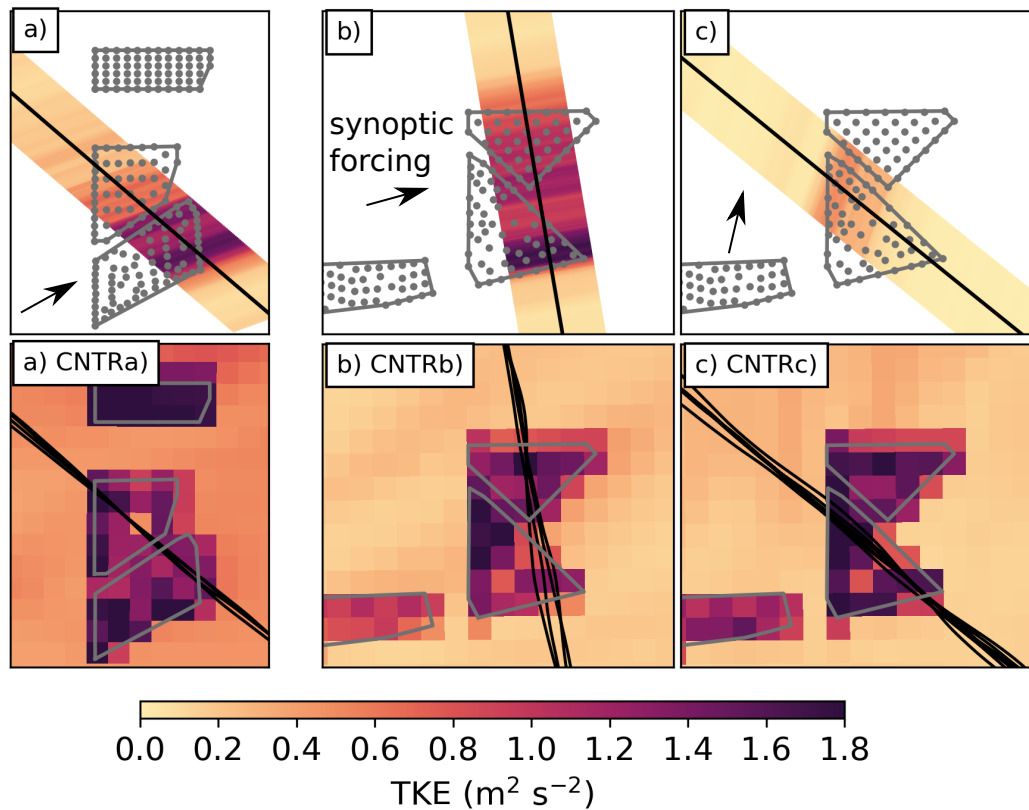


Figure 15: As Fig. 13, but for the TKE.

### 3.3 Sensitivity experiments

In case II, the model captures the background flow providing a sound basis for sensitivity studies. In contrast, the simulations for case study I and III have both a bias in the wind speed at 200 m or 250 m over and next to the wind farms associated with a deviation considering the intensity of an inversion for case III. For case I, we can only suggest that the negative bias in the horizontal wind speed is rooted in the stratification of the model due to the lack of measurements available at the North Sea.

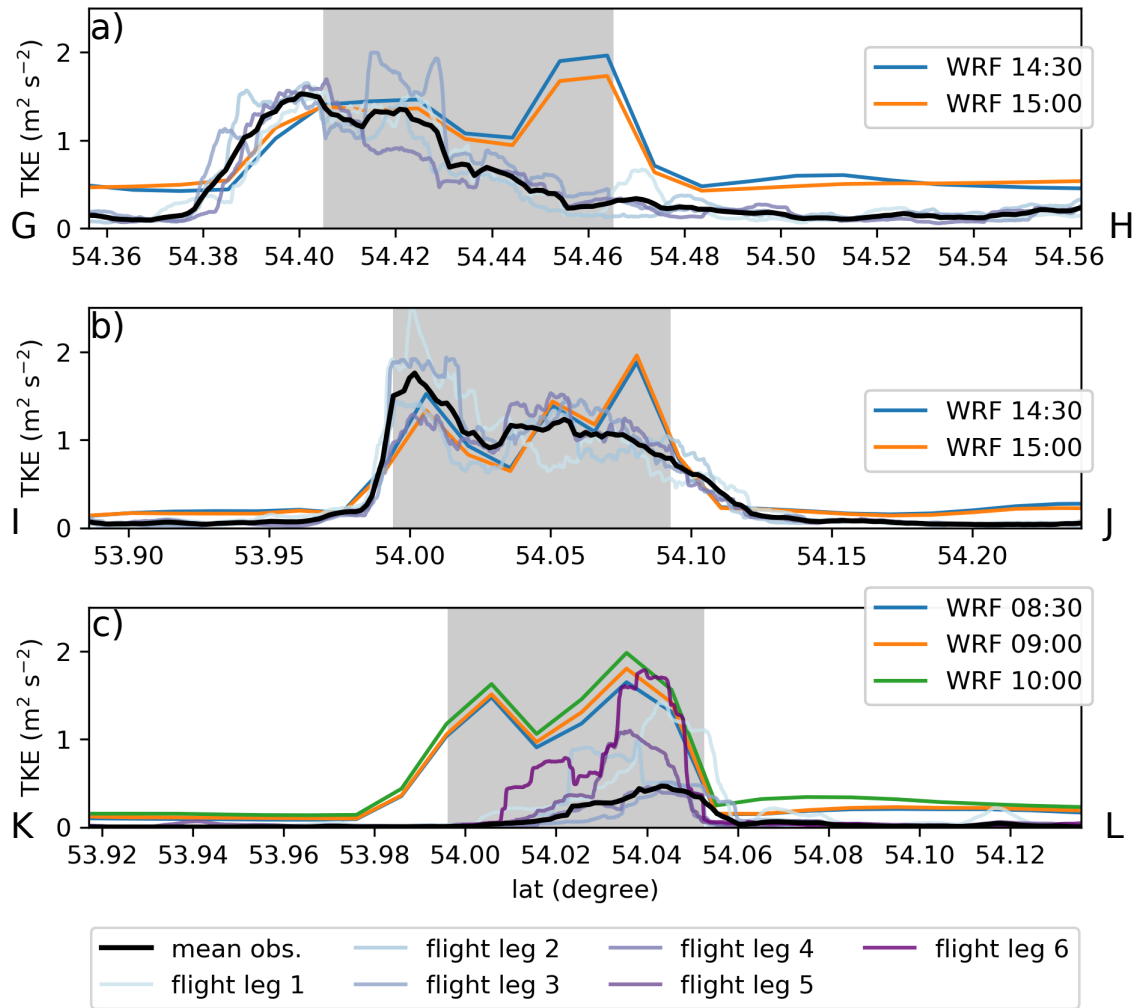


Figure 16: As Fig. 14, but for the TKE.

Given the success with the simulation CNTRb, we explore the sensitivity of the WFP of FITCH et al. (2012) with respect to horizontal grid size, the TKE source, vertical resolution, TKE advection and thrust coefficient in sections 3.3.1, 3.3.2, 3.3.3 and 3.3.4.

### 3.3.1 Sensitivity to horizontal and vertical resolution with an active TKE source

We conducted two additional simulations with a horizontal grid size of 5 km and 16 km with the TKE source of the WFP of FITCH et al. (2012) activated; these simulations are called DX5 and DX16. Additionally, a third simulation was performed with the same configuration as CNTRb but with 80 vertical levels (Vert80). A summary of all sensitivity tests is given in Table 4.

Coarsening the horizontal resolution of the simulations to 5 km resolution degrades the agreement between the simulations and observations. As expected, the sharp drop

in the horizontal wind speed in the observations at the southern edge of the wind farm oriented parallel to the incoming flow cannot be represented in a mesoscale simulation with a horizontal grid size of 5 km, a result similar to the CNTRb simulation (Fig. 18b). However, the wake impact on the horizontal wind speed at 200 m AMSL (i.e. 60 m above the wind farms) is captured well, rooted in a TKE only  $0.3 \text{ m}^2 \text{ s}^{-2}$  lower than the observed mean (Fig. 18a, Fig. 19b), except for the region of strong horizontal shear that can not be captured by a mesoscale model.

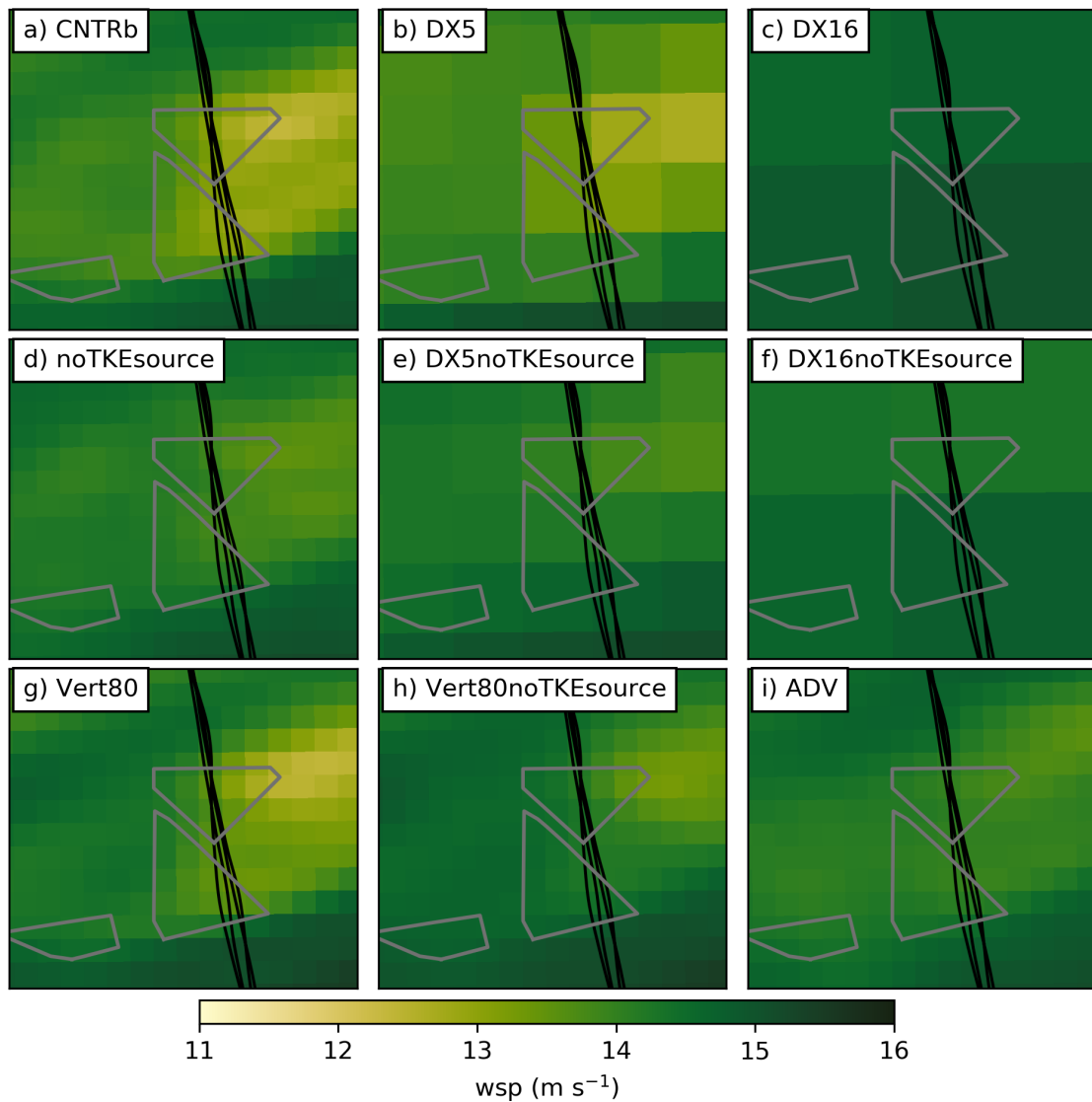


**Figure 17:** As in Fig. 13, but for the sensitivity simulations (b-i) DX5, DX16, noTKESource, DX5noTKESource, DX16noTKESource, Vert80, Vert80noTKESource and ADV at 15:00 UTC 14 October 2017 (case study II). For better comparison the control simulation CNTR is shown in (a).

Simulation DX16 reveals that a grid size of 16 km cannot capture the effect of wind farms with a size in the order of  $100 \text{ km}^2$  by the use of a WFP. Compared to CNTRb

the decrease in wind speed downwind of the wind farms GW is in the order of  $1 \text{ m s}^{-1}$  instead of  $2 \text{ m s}^{-1}$ , suggesting that the vertical mixing is underestimated. Accordingly, Fig. 19c) reveals that the simulated TKE is two times lower than observed.

More vertical levels cause the same amount of TKE above the wind farm compared to CNTRb, (Fig. 18a, Fig. 19g) but the wind speed deficit at the southern edge of wind farm is in better agreement with the observations (Fig. 17g, Fig. 18b) by up to  $0.5 \text{ m s}^{-1}$ . Additionally, the wakes as seen in the SAR image match better with the ones simulated in Vert80 than in CNTRb (Fig. 12). The wakes in Vert80 (Fig. 12c) are more pronounced compared to CNTRb (Fig. 12b) and, hence, fitting better to the observed SAR image.

### 3.3.2 Sensitivity to vertical resolution with a disabled TKE source

For comparison to wind farm parameterizations without an explicit turbulence source (VOLKER et al. 2015), we conducted three simulations with the TKE source switched off using the CNTRb configuration and two coarser horizontal grids than in CNTRb (noTKESource, DX5noTKESource, DX16noTKESource, Fig. 17d-f). Additionally, we performed a simulation having the TKE source disabled with 80 vertical levels, namely Vert80noTKESource (Fig. 17h).

All simulations with the TKE source switched off show larger wind speeds above the wind farms. For example, in the simulation noTKESource, wind speeds are  $\approx 14 \text{ m s}^{-1}$  above the wind farm (Fig. 17d) associated with a lower TKE (Fig. 18a) than in CNTRb. Consequently, we expected even higher wind speeds in DX5noTKESource above the wind farms associated with the lower TKE that can be resolved in a simulation with a grid size of 5 km. Indeed, the wind speed and the TKE over the farms is up to  $0.5 \text{ m s}^{-1}$  and  $0.3 \text{ m s}^{-1}$  lower than in CNTRb (Fig. 17e). Obviously, simulation DX16noTKESource fails to represent the impact of the wind farms on the wind speed (Fig. 17f) and the TKE (Fig. 19f).

Surprisingly, the simulation Vert80noTKESource with 80 vertical levels shows approximately the same TKE as simulated in noTKESource with 50 vertical levels, although more vertical shear should be resolved in Vert80 (Fig. 18a). This amount of TKE is similar to the noTKESource simulation. Consistently, the wind speed reduction above the wind farm is almost similar to the noTKESource simulation (Fig. 17b).

Summarized, all simulations without a TKE source produced too small of TKE compared to the observations. Therefore, we conclude that additional TKE is necessary to parameterize wind farms in mesoscale models in stable conditions.

### 3.3.3 Sensitivity to advection of TKE

The TKE advection option results in a greatly reduced TKE above the wind farm associated with a lower wind speed reduction above the wind farm. The simulated TKE is almost the lowest parameterized in all simulations performed for this study

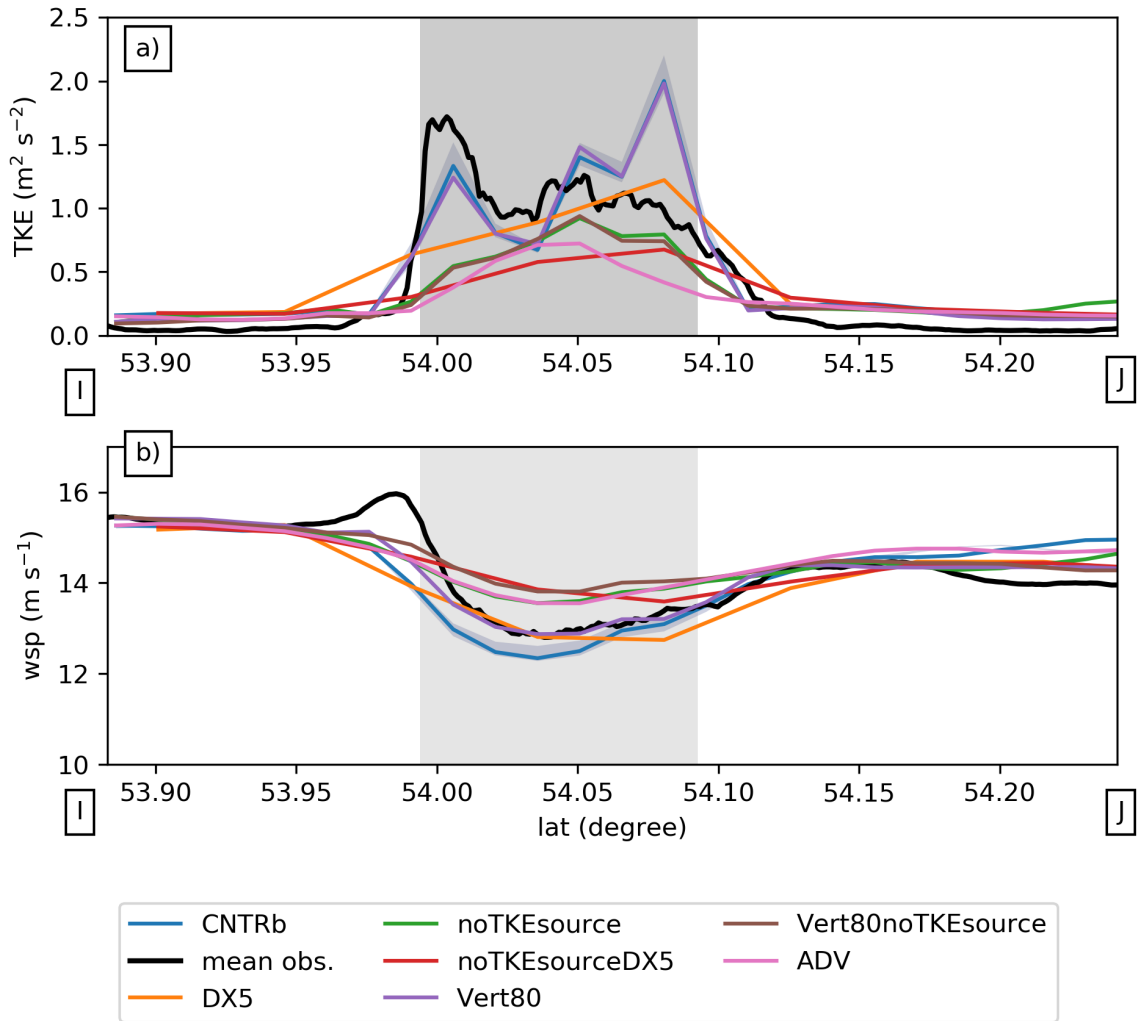


**Figure 18:** As in Fig. 14, but for TKE (a) and wind speed (b) for the sensitivity simulations DX5, noTKESource, DX5noTKESource, Vert80, Vert80noTKESource and ADV conducted for case study II. For better comparison the control simulation CNTRb plotted as well.

(Fig. 18a), resulting in an underestimation of the wind farm impact on the wind speed above the wind farm -  $2 \text{ m s}^{-1}$  less than the observed mean deficit (Fig. 17i, Fig. 18b). However, the ADV (i.e. advection of TKE is active) simulation shows the highest TKE values within the wake of the wind farm GW (Fig. 19i).

### 3.3.4 Sensitivity to thrust coefficient

Two simulations (ThrustMin, ThrustMax) were performed to investigate the uncertainty introduced by the estimated thrust- and power coefficients. The corresponding uncertainty is shown in Fig. 18 as shaded area around the results of the CNTRb simulation. The uncertainty in TKE due to the unknown power and thrust coefficients is smaller than the deviation caused by all sensitivity studies, except for simulation Vert80

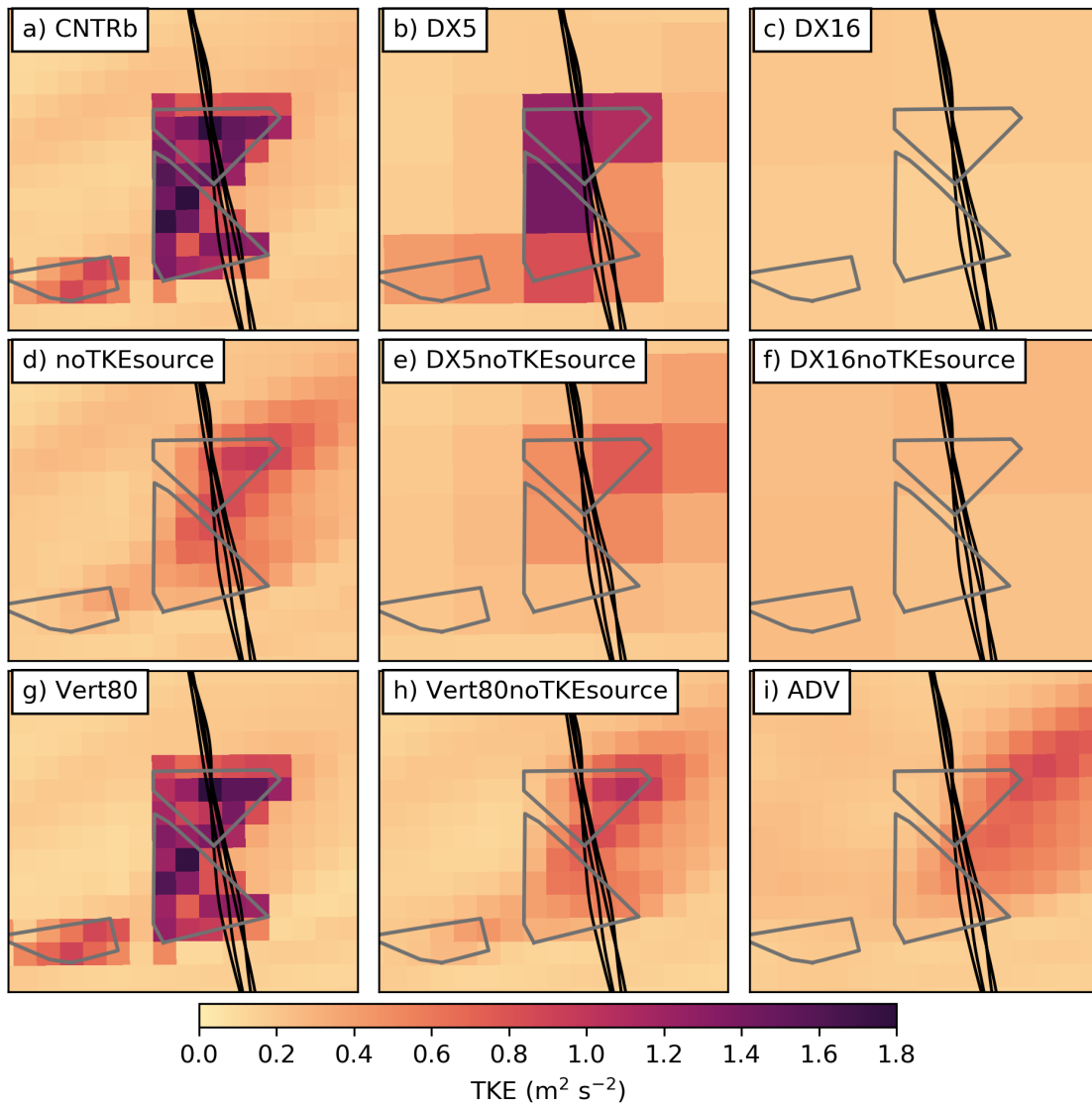


**Figure 19:** As in Fig. 15, but for the sensitivity simulations (b-i) DX5, DX16, noTKESource, DX5noTKESource, DX16noTKESource, Vert80, Vert80noTKESource and ADV at 15:00 UTC. For better comparison the control simulation CNTRb is shown in (a).

(Fig. 18a). The uncertainty resulting from the wind speed deficit is smaller than the effect of all the other physics and numeric permutations tested here, including the effect of vertical level variation. (Fig. 18b).

### 3.4 Discussion

Obviously, the most important ingredient for simulating realistic wind speeds above offshore wind farms is the correct representation of the atmospheric state, regardless of which configuration the WFP is used. In two of the three case studies examined here, the simulations analyzed here failed to represent the atmospheric background correctly.

WRF captured the state of the atmosphere for case II, as the boundary layer upwind of the wind farms GW was not modified by land. In contrast, the upwind conditions were not captured for the case studies I and III. Both cases were characterized by a large-scale flow modified by the land upwind. The model evaluation in section 3.2.1 revealed that the associated inversion in III that developed as warm air masses were advected from the land upwind over the German Bight, which is challenging for the simulation as described in SIEDERSLEBEN et al. (2018a). The inversion almost decoupled the layer at 250 m from any processes below 200 m (i.e. top of inversion height), resulting in a very low signal of the wind farm in the TKE and wind speed (Fig. 15c, Fig. 16c). In contrast, the simulation showed TKE values up to  $2.0 \text{ m}^2 \text{ s}^{-2}$ . However, during the additional two flyovers the TKE increased up to  $2.0 \text{ m}^2 \text{ s}^{-2}$  in the observations associated with a destabilizing MABL as Fig. 11c) reveals. Consequently, the TKE above the wind farms increased corresponding to an increased wind speed deficit during the last flyover. As the destabilization of MABL resulted in a profile with a potential temperature gradient similar to the simulated profile, the simulated and observed TKE have the same magnitude for the last two flyovers, underlining that the upwind conditions are crucial for representing the impact of offshore wind farms.

Our results suggest that under stable conditions mesoscale wind farm simulations should use an additional TKE source, as the mixing and the associated wind deficit above the wind farms are too low otherwise.

Given the success with the TKE source switched on, we recommend for regional climate simulations using horizontal grids in the order of 5 km to use a WFP with an active TKE source. Additionally, the grid size must accommodate the size of the wind farms installed in the region of interest. For example, regional climate simulation using a grid as VAUTARD et al. (2014); MILLER and KEITH (2018a) (i.e. 50 km, 30 km grid, respectively) would be unsuited for determining the climate impact of offshore wind farms on the German Bight, because we have shown that simulations with a horizontal grid size of 16 km are already too coarse to represent the impact on the MABL realistically. In contrast, simulations with a horizontal grid size of 5 km performed adequately when TKE was actively added to the model.

Strong shear lines at the edge of a wind farm or wake cannot be captured by mesoscale models. The strong horizontal shear observed at the wind farm GW at the southern edge oriented parallel to the impinging flow, has a horizontal extent of  $\approx 2$  km. Following SKAMAROCK (2004), realistic solutions only exist for processes having seven times the grid size. Consequently, the horizontal shear with the associated TKE cannot be represented by mesoscale models. However, in the simulation for case study II one could think that the model can present the shear line at the southern edge when considering only the TKE. Both the simulation and the observation show a TKE maximum at the southern edge of the wind farm. However, the peak in the

observations was associated with the horizontal wind shear. In the model, the wind farms GW extend more to the south than in reality, hence, the TKE peak in the simulations is associated with the TKE source of the WFP and not with the horizontal shear.

The WFP's TKE source possibly introduces too much TKE on the upwind edge of a wind farm. Although the simulations did not capture the atmospheric background in case study I, we noticed an important difference between the simulated and observed TKE. In the observations, the TKE above the wind farms increased as the flow penetrated through the wind farms (Fig. 16a), whereas the model adds the most TKE at the upwind side of the wind farm. The amount of TKE added to the model depends on the wind speed, the number of wind turbines, and  $C_{TKE}$  (see Eq. 3). Therefore, the added TKE is highest at the locations with the highest wind speeds within the farm, that is, at the front row of the wind farm. Of course, if the front row is associated with a high wind turbine density, the WFP also adds the most TKE at the upwind side of the wind farm. In case study I, wind turbine density is high with up to five turbines per grid cell at the western edge of the wind farms (Fig. 7a). Additionally, we had south-westerly winds exposing the western edge of the wind farms to the highest wind speeds (Fig. 13a). Consequently, the simulated TKE has a maximum at the upwind side that was not observed in the aircraft measurements (Fig. 15a, Fig. 16a). However, without a TKE source, the deceleration was too low compared to the observations, especially when horizontal grids are larger than or equal to 5 km.

The uncertainty of our simulations for case study II, introduced by the estimated thrust- and power coefficients is smaller than the effect of changing either the horizontal resolution or disabling the TKE source of the WFP of FITCH et al. (2012). Therefore, our sensitivity experiments conducted for case study II give useful and general recommendation for offshore wind farm simulations under stable conditions.

### 3.5 Summary

Using airborne measurements of wind speed and turbulent kinetic energy near offshore wind farms, we evaluate the wind speed and turbulent nature of the wind farm wakes as well as the parameterization of those wind farm wake effects enabled by the Weather Research & Forecasting Model (WRF) Wind farm parameterization (WFP) of FITCH et al. (2012). Our study considered three cases at two different sites. Three case studies were, all characterized by stable conditions. During two case studies, the marine boundary layer was highly influenced by the land upwind, resulting in deviations between observation and simulations. However, during one case study, the impinging flow was coming from the west resulting in an inflow unaffected by any land. Hence, the WRF model represented the state of the atmosphere in the vicinity of the wind farms reasonably well. That allowed us to perform sensitivity studies in terms of horizontal

and vertical resolution. Additionally, we investigated the effect of the TKE source of the WFP of FITCH et al. (2012) on the MABL as well as the option of advecting TKE in the boundary layer scheme of WRF. These are our main findings:

- We recommend using the TKE source of the WFP of FITCH et al. (2012) for offshore wind farm simulations under stable conditions, especially for simulations having a horizontal grid coarser or equal to 5 km. However, we notice that the WFP adds too much TKE at the upwind side of a wind farm. We observed during two case studies that the TKE above the wind farms increased with the path of the air through the wind farm, meaning that the TKE is higher at the downwind side of a wind farm than on the upwind side. In contrast, the WFP simulated the highest TKE at the upwind side of the wind farm associated with the highest wind speeds and wind farm density at the front row turbines. Nevertheless, the wind speed deficit is underestimated with the disabled TKE source. Therefore, we suggest using the TKE source for stable conditions.
- Simulations using the WFP of FITCH et al. (2012) using a grid size of  $\approx 15$  km or more underestimate the impact of wind farms on the MABL under stable conditions, regardless of the mode of the TKE source. Given the fact that the impact of offshore wind farms is largest during stable conditions, we suggest that climate simulations assessing the impact of offshore wind farms should use a horizontal grid in the order of 5 km or finer. This horizontal resolution is difficult to achieve for global simulations, but feasible for regional climate simulations.
- In terms of the vertical resolution, we obtained best results with 80 vertical levels, equal to a spacing of 12 m below 400 m AMSL as in LEE and LUNDQUIST (2017). We tested two sets of vertical levels resulting in 3(1) and 13(4) levels below and within the rotor area. In case of an activated TKE source only minor differences were observed between the two sets of vertical levels. However, the wind speed deficit was captured better with the finer vertical resolution. Additionally, the simulated wakes agreed better with SAR data due to the smaller spacing of the vertical levels close to the surface. Therefore, we recommend a spacing of the vertical levels in the order of  $\approx 12$  m for offshore simulations. In case computational resources are limited, simulations with a horizontal and vertical resolution of 5 km and 35 m below 100 m also captured the most important features above the wind farms.
- Activating the TKE advection in the boundary layer scheme was associated with too low TKE above the wind farms that, in turn, resulted in an underestimation of the wind speed deficit above the wind farm.

These results support the hypothesis that the TKE source in the WFP of FITCH et al. (2012) is necessary under stable conditions at offshore wind farm sites, although we suggest that the added TKE is overestimated at the upwind side of the wind farms, suggesting possible future improvements. Given the results of this study, previously published studies assessing the impact of offshore wind farms have possibly underestimated the impact on the marine boundary layer, hence, we suggest regional climate simulations for offshore sites with a grid size of 5 km or finer. However, the skill of such regional climate simulations is lessened when the flow is from onshore due to the difficulty of parameterizing coastal effects. Thus future work should primarily focus on boundary layer parameterizations that can capture the transition from land to open sea and vice versa.

## 4 The far-field of large offshore wind farms

The processes above an offshore wind farm influence the MABL downwind. Therefore, the model setup is used as suggested in the previous chapter to investigate in this chapter the far-field of offshore wind farms. This chapter focuses mainly on observations recorded on 10 September 2016 (more details are provided in section 2.1.3) and the simulations for this particular day. A synoptic overview is given in section 4.1 followed by an evaluation of the simulations upwind (section 4.2). Based on these results, this work presents wake measurements and simulations for 10 September 2016 (section 4.2.3) and compares this case to all other measurements recorded downwind of large wind farms in the framework of the WIPAFF project (section 4.4.2). The results shown in this chapter were published in SIEDERSLEBEN et al. (2018a) and SIEDERSLEBEN et al. (2018b).

### 4.1 Observation

First, an overview of the meteorological conditions prior to and during the field experiment is given in section 4.1.1, followed by section 4.1.2, where the vertical structure of the atmosphere is examined. Due to advection of warm air over the cold water surface from the nearby land surface, the atmosphere at the wind farms was stably-stratified.

#### 4.1.1 Synoptic and mesoscale overview

A trough centered over the Faroe Islands at 0600 UTC 10 September 2016 (i.e., 2 hours before the research flight started) was associated with a southwesterly flow at the German Bight and a cold front at 925 hPa, extending from southern England to the southern end of Norway (Fig. 20a). The front was orientated parallel to the mean flow and was therefore almost stationary and did consequently not directly influence the German Bight. The southwesterly flow caused warm air advection over the North Sea at 925 hPa (Fig. 20b).

The flow upwind of the wind farms of interest was highly influenced by the land surface. From 0600 UTC to 1200 UTC the wind direction changed from southwesterly to southerly. As the wind rotated, the distance from the wind farms to the coast decreased. Therefore, the rapidly-warming land surface exerted a stronger influence on the boundary layer upwind of the wind farms. Especially, in the second half of the field experiment, warm air was advected from the warmer land surface - the northern part of Germany. This pattern typically causes a stably-stratified atmosphere over the Baltic Sea (e.g. DÖRENKÄMPER et al. 2015; SVENSSON et al. 2016) and is therefore also relevant for the North Sea. Therefore, this study investigates the vertical stratification of the atmosphere in detail in the following section.

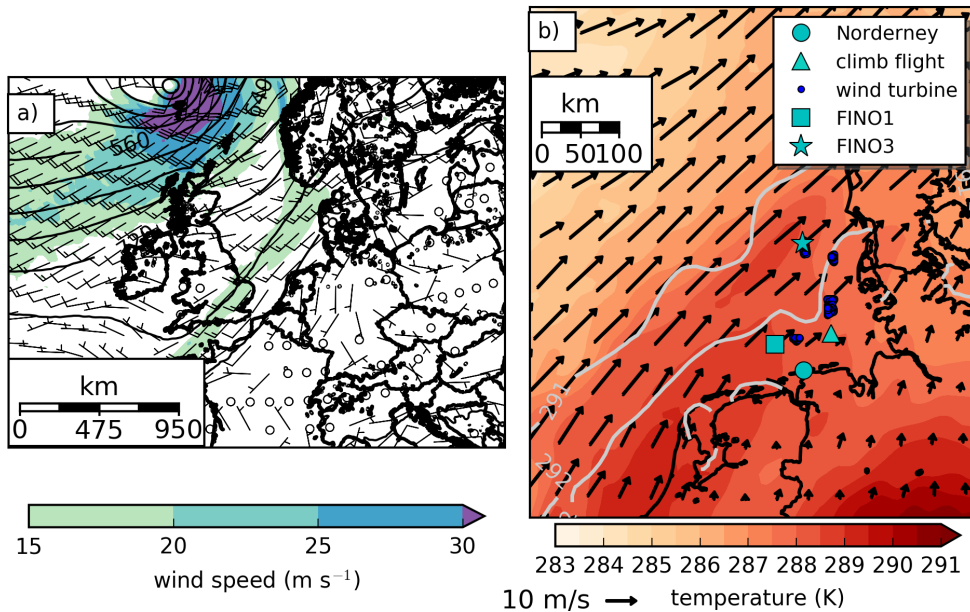


**Figure 20:** ECMWF analysis at 0600 UTC 10 September 2016: (a) 925-hPa analysis of geopotential height as black contour lines (40-m increment), wind barbs (half and full barbs for  $2.5 \text{ m s}^{-1}$  and  $5 \text{ m s}^{-1}$ , respectively, circles denote wind speeds below  $2.5 \text{ m s}^{-1}$ ) for the horizontal wind field. (b) The 925-hPa analysis of potential temperature as colored contours (0.5-K increment).

#### 4.1.2 Vertical structure of the atmosphere

According to analytical models, the vertical and lateral transport of momentum determines the wake recovery (EMEIS 2010b). The vertical transport of momentum is in turn heavily influenced by the stratification of the atmosphere. Therefore, this section assesses the vertical state of the atmosphere during the field experiment.

Stable conditions occurred between 60 m and 100 m AMSL in the ascent portion of the flight leg, as seen in the potential temperature profiles (Fig. 21). Above 100 m, a strong inversion (i.e.  $0.02 \text{ K m}^{-1}$ ) extends to rotor-top (150 m) associated with a decrease in the water vapor mixing ratio of  $11.0 \text{ g kg}^{-1}$  below the inversion to  $8.5 \text{ g kg}^{-1}$  above (Fig. 21d). Above the rotor area, the atmosphere is still stably stratified but with a weaker vertical positive potential temperature gradient (i.e.  $0.003 \text{ K m}^{-1}$ ) than within the rotor area.

Further upwind of the ascent flight, at FINO1, the atmosphere was weaker stratified below 40 m AMSL at 0800 UTC. Figure 22 shows the vertical temperature profile of FINO1 and FINO3 at 0800 UTC, 0900 UTC and 1000 UTC. The SST at FINO1 was 292.5 K at 0800 UTC whereas the air temperature at 40 m was 292.2 K. When the measurement uncertainties are considered, these measurements suggest that the atmosphere was either slightly stably stratified or neutrally stratified below 40 m.

It is most likely that the weakly stratified layer was caused by cold air advection stemming from the nocturnal inversion of the land surface located approxi-

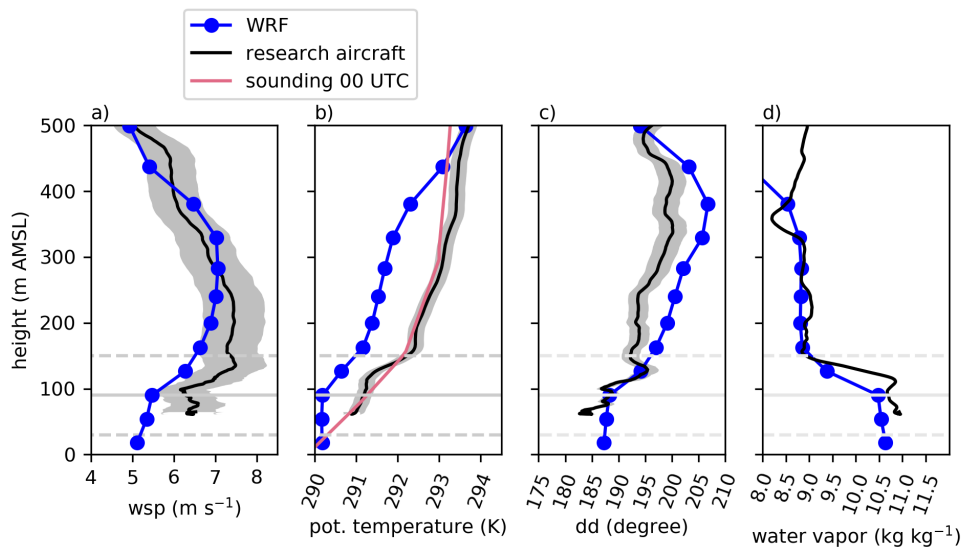


**Figure 21:** Vertical profile of (a) wind speed, (b) potential temperature, (c) wind direction and (d) water vapor measured by the aircraft at the location indicated in Fig. 20. The simulation results were spatially interpolated onto the flight track and are plotted in blue colors. Every blue dot denotes a full WRF level. The sounding for Norderney at 0000 UTC 10 September 2016 is indicated by a red line. Grey shadings indicate the relative errors of the measurements. The climb flight and sounding location are shown in Fig. 5 and Fig. 20. The rotor area of the turbines is marked with dashed grey lines and the hub height (90 m above AMSL) with a grey solid line.

mately 100 km upwind, as indicated by the sounding of Norderney that was taken at 10 September 00 UTC (i.e. 8 hours before the climb flight). The potential temperature profile of the sounding matches the one taken by the aircraft. This emphasizes that the nocturnal inversion of the land surface was advected by the large scale southerly flow. However, the absence of a weakly stratified layer in the sounding indicates that the ocean warmed the lower atmosphere over the ocean and destabilized the lower atmosphere at FINO1.

From 0900 UTC onward, warm air advection dominated the stratification of the atmosphere upwind of the wind farms. Therefore, the weakly stratified layer below 40 m experienced a stabilization at FINO1. For example, at 1000 UTC a SST of 292.7 K was observed at FINO1 and 292.7 K at 40 m, indicating a stably stratified layer in the lowest 40 m of the atmosphere.

In contrast, at FINO3 the lower atmosphere was stably-stratified during the whole measurement campaign. This was mainly caused by a lower SST further away from the coast (Fig. 20) and the fact that FINO3 was not affected by the cold air advection of the nocturnal inversion. This is evident from Fig. 22, over the whole observational period the SST was lower than the lowest air temperature measured at FINO3 at 23 m AMSL. Consequently, the lower atmosphere was stably stratified at FINO3.

Over the course of the day, the air above land warmed faster than the marine

boundary layer. This warm air reached the marine boundary layer close to the coast around 0900 UTC (Fig. 22b), hence, the lower boundary layer at FINO1 became also stable.

The stably-stratified atmosphere, 60 m AMSL, was associated with a weak low-level jet between 100-300 m (Fig. 21). Below hub height, the wind speed varied between  $6 \text{ m s}^{-1}$  and  $7 \text{ m s}^{-1}$ ; above hub height, the wind speed increased up to  $7.3 \text{ m s}^{-1}$  at 150 m AMSL, the height of the top of the inversion. At 250 m AMSL the wind speed decreased to  $5 \text{ m s}^{-1}$ .

## 4.2 Control run

In this section the results of the control run (i.e. WRF configuration as described in section 2.6.1) are presented. First, the upwind flow is verified to provide a sound basis for the error discussion of the wind farm parameterization presented in section 4.4. Then the wake measurements are compared with our simulations.

### 4.2.1 Verification of the background flow

As described in section 2.1.2, the research aircraft probed the atmosphere approximately 20 km upwind of the wind farms (Fig. 20). The measured wind speed and potential temperature are shown in Fig. 21a) and b), respectively. To evaluate the upwind flow, the WRF data is interpolated spatially onto the track of the climb flight of the research aircraft. Every blue dot in Fig. 21 represents the value of a single vertical level.

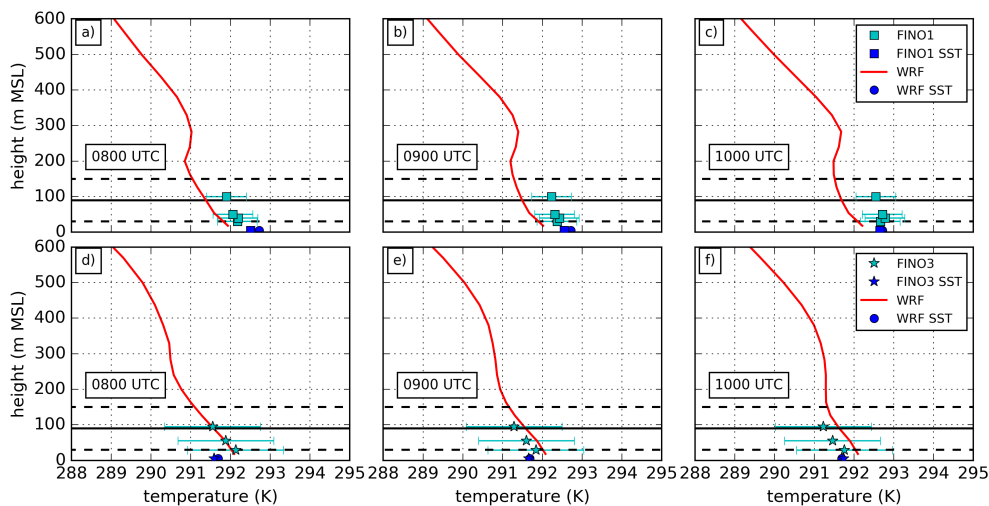


**Figure 22:** Evaluation of the stratification up- and downwind of the wind farms at FINO1 (top three panels) and FINO3 (bottom three panels) at 0800 UTC, 0900 UTC and 1000 UTC 10 September 2016. The location of these measurement towers are indicated in Fig. 20. The simulated profiles are plotted in red. The rotor area and hub height are indicated as in Fig. 21.

Figure 21b) reveals that WRF captures the inversion at the rotor area height but has a bias of approximately 1 K up to a height of 400 m. However, the decreasing

water vapor mixing ratio associated with the inversion is represented well in the simulations. Above 400 m, the model represents the atmosphere well. Below hub height, the model shows a neutrally-stratified layer, which could not be evaluated by aircraft measurements as the aircraft was not allowed to fly below 60 m AMSL. However, the contrast between SST and the lower atmosphere influences the marine boundary layer (FRIEHE et al. 1991). Therefore, we use data from FINO1 and FINO3 to evaluate the marine boundary layer close to the surface (Fig. 22).

Figure 22 reveals the same problem as the flight measurements, an offset of approximately 1 K close to the surface during the whole flight campaign. However, in both the measurements and in the simulation the SST is higher than the air temperature at 0800 UTC and 0900 UTC. Nevertheless, one hour later at 1000 UTC, the lower marine boundary layer warmed faster than in the simulation (Fig. 22c). Measurements at FINO1 (Fig. 22c) show an almost isothermal atmosphere with a temperature equal to the SST, whereas the model has a negative vertical temperature gradient with a temperature lower than the SST. Consequently, the model was not as stably stratified as reality at 1000 UTC.

With increasing fetch from the coast, the model performance improves. Vertical temperature profiles of FINO3 and WRF match, especially at 0800 UTC and 0900 UTC. At 1000 UTC the simulation is 0.2 K higher than FINO3.

Wind speed measurements agree well with the model results (Fig. 21), showing an increase in wind speed up to a height of 250 m AMSL. However, within the rotor area, the model underestimates the wind speed by up to  $1.0 \text{ m s}^{-1}$ . Above the rotor area, simulation and observation agree well. Above 250 m, the model overestimates the wind speed by  $1 \text{ m s}^{-1}$ , corresponding to a more pronounced inversion in the model compared to the observations. Above 400 m, model and observation agree within  $0.5 \text{ m s}^{-1}$ .

The model simulates the wind directions well. However, during the second half of the measurement flight, the mean flow shows more southerly flow than the simulations (discussed later).

#### 4.2.2 Evolution of the wind field upwind of the wind farms

The simulated horizontal wind field at hub height (Fig. 23) shows higher wind speeds over the open ocean than over land, due to lower surface friction over the ocean and the incoming trough (Fig. 20a) approaching the German Bight from the north-west.

Near to the coast of the German Bight, streaks of reduced wind speeds can be observed as in DÖRENKÄMPER et al. (2015). In their study, these streaks are caused by the varying surface roughness at the coastline. Consequently, the wind field upwind of the wind farms is not homogeneous in space.

Further, the wind speed in the observational area decreased during the flight campaign, as seen in Fig. 24a-c) and from the measurements at FINO1 (not shown). Up-

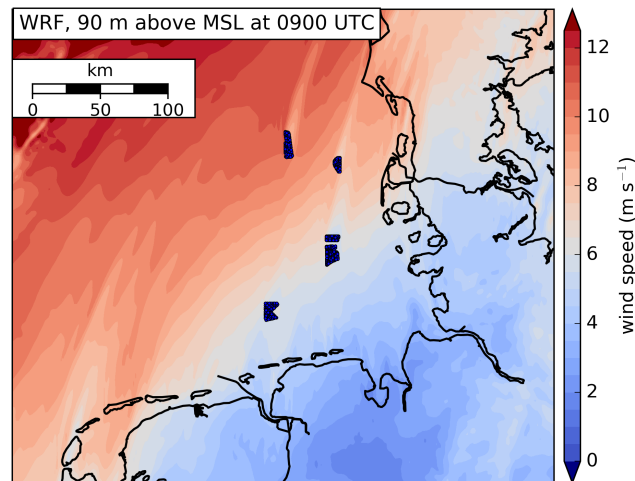


**Figure 23:** Coastal effects on the wind field 90 m above AMSL at 0900 UTC, 10 September 2016. The horizontal wind speed is shown with colored contours. The locations of the wind turbines are marked with blue dots. A more detailed look on the wind turbine distribution within the wind farms Meerwind SuedOst, NordseeOst and Amrumbank West is provided in Fig. 6.

wind of the wind farms, the simulated wind speed decreases from  $6.0\text{--}6.5\text{ m s}^{-1}$  down to  $5.5\text{--}6.0\text{ m s}^{-1}$ . This decrease is likely due to the sea breeze circulation aligned with the large scale flow in the morning hours opposite to the large-scale flow as soon the adjacent land warmed. Consequently, the wind farms AW, MSO and ONO experienced lower upwind wind speeds at the end of the flight campaign.

In summary, the wind field was inhomogeneous in time and space. To compare the model output to the observations at nearly-simultaneous times, the model output is used that was averaged over all simulated time steps (available for every 5-minute interval) from the time over which the data collection occurred. For example, the first flight leg collected data from 0820–0830 UTC. Therefore, in Fig. 24e), the WRF simulations for the first leg consider only WRF model output averaged from 0820–0830 UTC. The second flight leg consists of data collected from 0835–0845 UTC, and so the model data pictured in Fig. 24e). Panel f) is simply the difference between the data visualized in d and e. The results of this method are presented in detail in the following section.

### 4.2.3 Wake simulations

This section presents the spatial extent of the measured and simulated wake, whereby the wake is characterized with respect to wind speed, potential temperature and water vapor.

#### Wind speed

**Horizontal extent of the wake** The spatial dimensions of the modeled and observed wakes agree well. Figure 24 compares the observed and the simulated wake

that was obtained with the wind farm parameterization of FITCH et al. (2012). The simulated wind speed at hub height at 0830 UTC, 0900 UTC and 0930 UTC is shown in Fig. 24a-c) to suggest the development of the wake and the upwind conditions. The observed wake is shown in Fig. 24d), the simulated wind speed interpolated onto the flight track in Fig. 24e) and the deviation between WRF and observation, in Fig. 24f).

Both the model and the observation show a wake extending 45 km downwind of the wind farm. According to the simulation, this wake was long enough to reach the wind farm Butendiek located 50 km downwind of Amrumbank West. In the spanwise direction, the wake has dimensions of approximately 12 km, similar to the maximal width of the wind farms AM, MSO and ONO. The width of the simulated wake decreases with increasing distance from the wind farms but not the observed wake. For example, 35 km downwind of the wind farm, the simulations show a narrowing wake compared to the first flight leg by approximately 5 %.

The model underestimates the wind speed upwind of the wind farm, consequently, the wind speed downwind of the wind farm is expected to be lower in the simulations than the observed one. Indeed, the difference WRF (interpolated onto the flight track) minus observation shows mostly negative values, indicating that the WRF simulation underpredicts the wind speed in and outside of the wake (Fig. 21d and Fig. 24e). The deviation outside of the wake is greater than inside the wake. Inside the wake, the model underpredicts the wind speed by up to  $-0.6 \text{ m s}^{-1}$  whereas outside of the wake, the deviations are more than three times larger by up to  $-1.7 \text{ m s}^{-1}$ . This is especially true for the wind field located on the western side of the wake. A strong gradient in the wind field is present between the wake and the undisturbed flow in the observations. This gradient is not resolved in the simulations, consequently, a large error is observed on the western edge of the far-field.

Within the wake, the errors are much lower: for example, at the first flight leg downwind of the wind farm, the simulated wake has a wind speed of  $6.0 \text{ m s}^{-1}$ , whereas  $6.5$  to  $7.0 \text{ m s}^{-1}$  were observed. Corresponding to this result, the difference WRF - observation (Fig. 24f) is between  $-0.8 \text{ m s}^{-1}$  to  $-0.2 \text{ m s}^{-1}$  within the wake region. Further downwind, at the second and the third flight leg, the error decreases within the wake region and errors of around  $-0.2 \text{ m s}^{-1}$  and  $0.2 \text{ m s}^{-1}$  are observed.

From the third flight leg downwind, the wake is shifted more to the east in the model compared to the flight measurements. Therefore, the model overestimates the wind speed within the observed wake region by up to  $0.5 \text{ m s}^{-1}$  and underestimates the wind speed outside of the observed wake region by up to  $0.4 \text{ m s}^{-1}$ .

**Vertical extent of the wake** The research aircraft flew at five different heights 5 km downwind of the wind farms to capture the vertical wind speed deficit as explained in section 2.1.2. This study focuses on the actual ability of the model to simulate the vertical dimensions of the wake. Therefore, the difference between wind speed

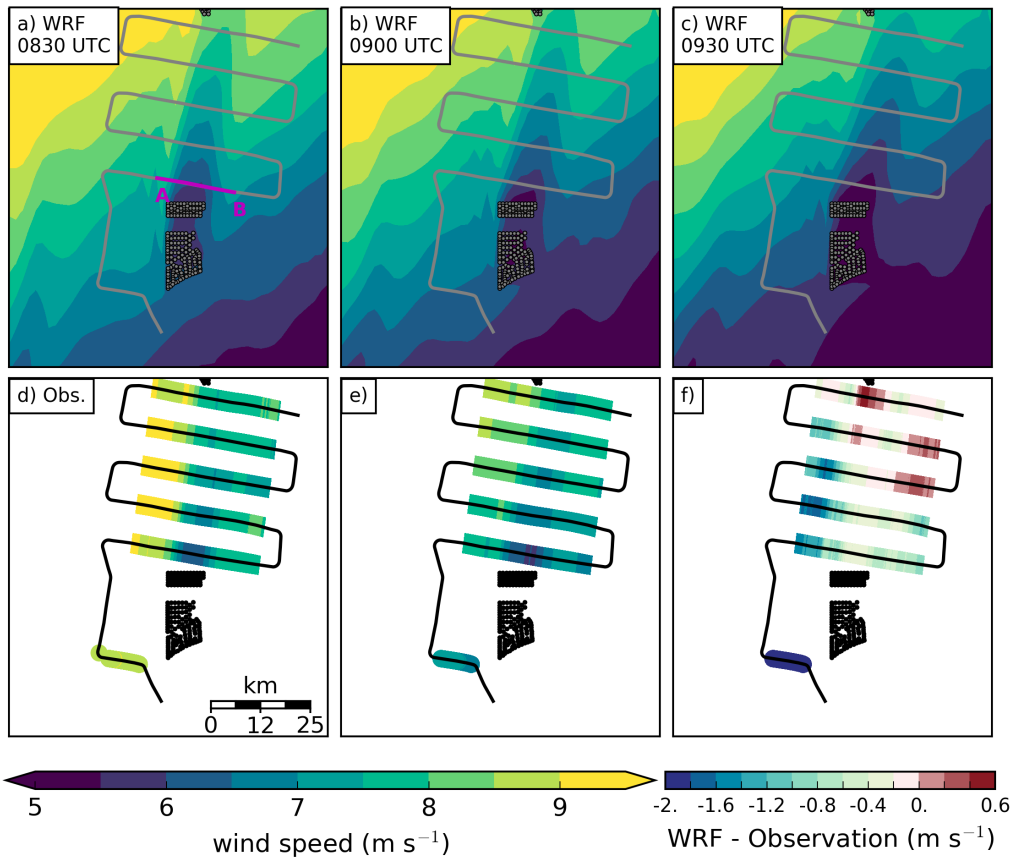


**Figure 24:** Comparison of simulated and measured wind speed at hub height in the far-field of the wind farm. The simulated wind speed at hub height during the observational period (a) 0830, (b) 0900 and (c) 0930 UTC is shown in colored contours. The observed wind speed at hub height is shown in (d) in the same colored contours as the simulation results (e). The black line denotes the flight track. Black dots indicate the locations of the single wind turbines. In (e) the simulation results were interpolated onto the flight track, spatially and timely, for details - see text. In (f) the difference, WRF (e) - observation (d) along the flight track is plotted. The vertical cross-section shown in Fig. 25 is shown by a pink line, with the beginning and end of cross-section annotated with A and B, respectively.

minimum within the wake and the surrounding wind speed is shown in Fig. 25 a,c,e). For simplicity, this difference is called *wind deficit recovery* throughout this study.

The wind speed reduction is also shown in percent. For the simulation, the wind speed reduction was calculated by comparison of a simulation without and with wind farms. To estimate an observed wind speed reduction, an undisturbed wind speed of  $8.5 \text{ m s}^{-1}$  is assumed, corresponding to the wind speed on the western side of the wake (Fig. 24d). However, it has to be kept in mind that a wind speed gradient extended from east to west. Therefore, the wind speed reduction values on the eastern edge of the wake are biased. Further, wind speed is most of the time increasing with height. Hence, the observed wind reduction values at 60 m and 220 m should be considered carefully.

The measurements and the model show both a wind speed reduction well above the rotor area (Fig. 25). The model overestimates the width of the wake at the western flank of the wake at 1000 UTC (Fig. 25c). This error is rooted in the stronger horizontal wind speed gradient in the observations than in the simulations (Fig. 24).

The minimum in the observed wake is more pronounced in the observations than in the simulations (Fig. 25). Within the center of the wake, the wind deficit recovery has values between 0 and  $0.5 \text{ m s}^{-1}$  between 60 m and 90 m in the observations, compared to values of over  $0.5 \text{ m s}^{-1}$  in the simulations (Fig. 25a,c,e). The wake recovers faster in vertical directions in the simulations at 1000 UTC (Fig. 25c). However, at 1100 UTC the simulation shows a wake exceeding the vertical dimensions of the observed one (Fig. 25e).

When wind speed deficit is shown in percent, the model seems to overestimate the vertical extent of the wake. Further, the wake center is located 20 m higher than in the measurements and underestimated by 5 percent. In contrast, the horizontal gradient of the relative wind reduction matches the observed one at the western flank of the wake, which is not the case for the wind deficit recovery.

## Temperature

Behind the wind farms, warmer air was observed and simulated at hub height within the wake even 45 km downwind of the last turbine (Fig. 26a and c). According to the simulations, the potential temperature in the wake is 0.4 K warmer than the air upwind. This effect is more pronounced in the observations. At hub height in the upwind climb flight, a potential temperature of 291.2 K was measured (Fig. 21) compared to maximal 291.8 K within the wake, indicating a warming of up to 0.6 K at hub height. Additionally, the observations show a stronger horizontal difference between wake and no-wake region downwind of the wind farm cluster. At the eastern flank a potential temperature gradient of 0.8 K was observed, in contrast to a difference of 0.4 K in the simulations.

The model has a cold bias of  $\approx 0.6 \text{ K}$  compared to the observations. However, the model is stably-stratified above hub height, corresponding to the observations. As this study wants to investigate the impact of wind farms on the MABL and not the bias of the simulations, we add 0.6 K to all shown potential temperature figures in this study.

The potential temperature wake was associated with a mixed layer, as seen in the cross-section 5 km downwind of the wind farm cluster (Fig. 27a and c). However, both cross-sections from observation and simulation indicate that warmer air was mixed downward. The mixed layer extends up to 120 m AMSL in the observations (Fig. 27a); in the simulation, this neutral layer is only 100 m thick.

Mixing warmer air downward corresponds to an enhanced sensible heat flux downward (Fig. 27e). In the observations, the atmosphere was stably stratified, conse-

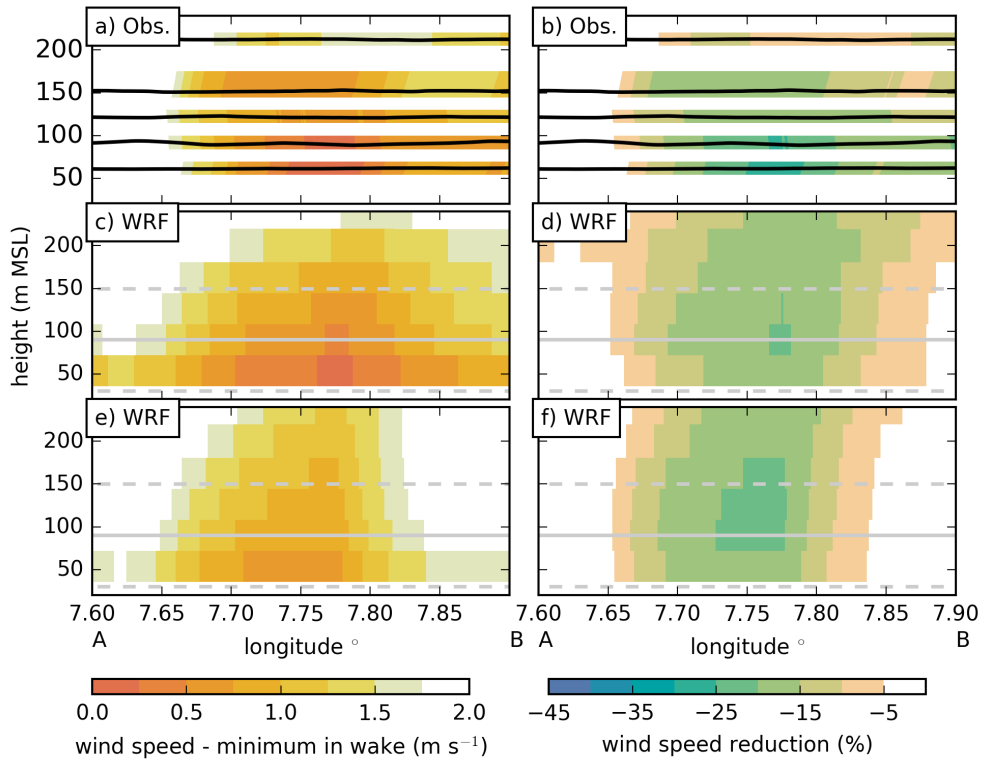


**Figure 25:** A comparison between aircraft measurements (a-b) and WRF simulation (c-d 1000 UTC and e-f 1100 UTC) along the vertical cross-section perpendicular to the main flow, 5 km downwind of the wind farms as indicated in Fig. 24a). Panels (a), (c) and (e) show the wind speed difference between wind speed minimum within the wake and surrounding wind speed in colored contours, indicating a measure of wind deficit recovery (as larger the difference as faster the wind speed recovers). Panels (b), (d) and (f) show the relative wind speed reduction in percent using colored contours. In the observational panels (a) and (b) the flight tracks are denoted as black thick lines. In the simulation panels (c-f), the hub height is indicated by a grey solid line, the upper and lower end of the rotor area is made visible by the grey dashed line. The simulation results (c-f) are shown by using a pixel plot to highlight the resolution of the model.

quently, a sensible heat flux towards the surface is expected (i.e. a negative sensible heat flux). Figure 27e) shows the difference in sensible heat flux between a WF and a NWF simulation along the cross-section C-D. The blue contours indicate that the wind farms caused a greater downward heat flux above and within the farm, hence, explaining the warming below  $\approx 180$  m AMSL (Fig. 27e). The simulations show cooling aloft right above the farm area and warming within the farms but starting half-way through the farm area and extending much farther downwind than the cooler area Fig. 27f).

### Water Vapor

Within the wake of the wind farm cluster, the air is dryer than in the ambient air outside of the wake (Fig. 26b and d). Similar to the wake in the potential temperature, the dryer air is still visible 45 km downwind of the wind farm cluster. Within the wake region, the air has a minimum water vapor mixing ratio of  $9.8 \text{ g kg}^{-1}$  compared to

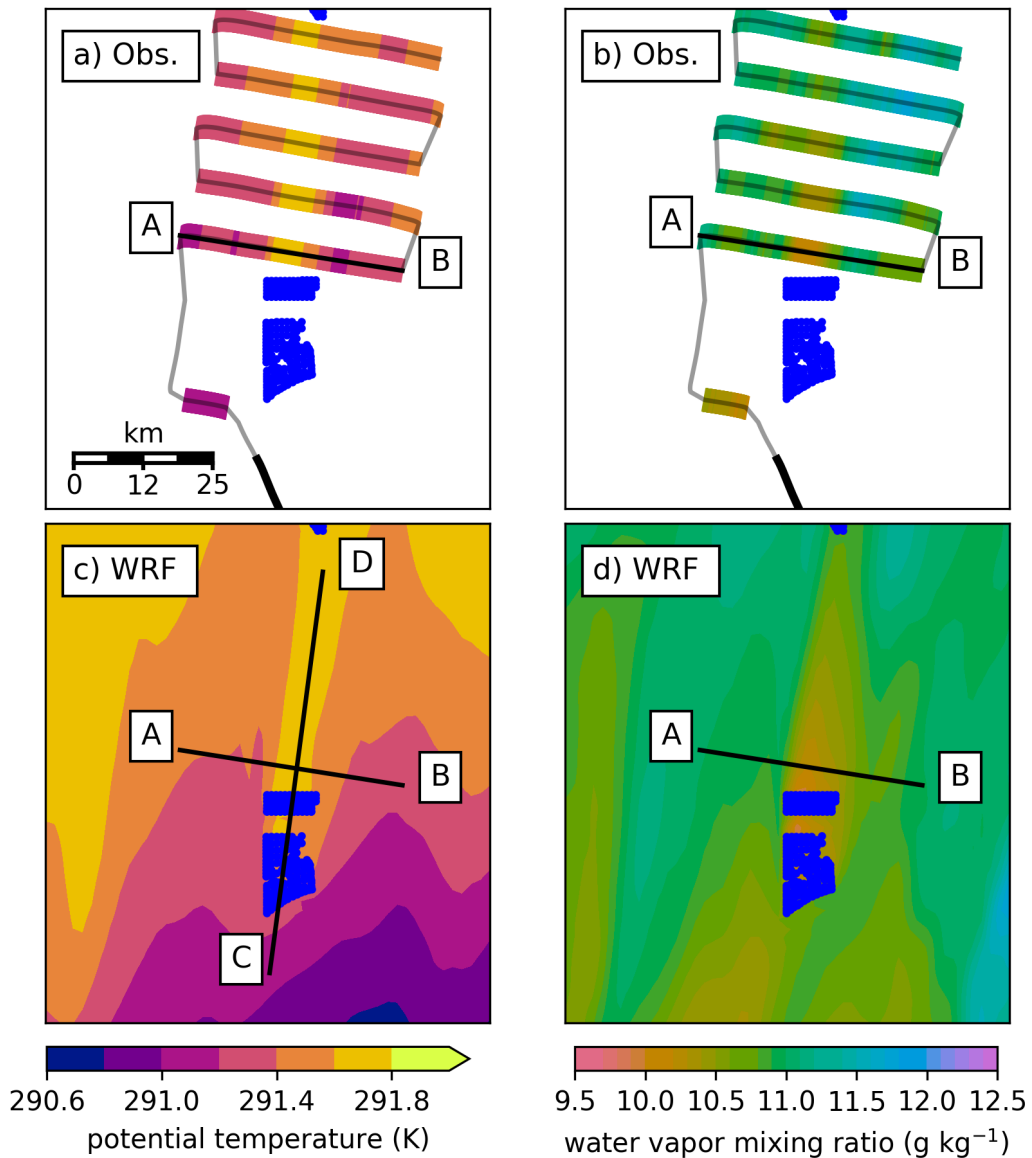


**Figure 26:** Potential temperature (a, c) and water vapor mixing ratio (b, d) on 10 September 2016 at hub height. The observations are shown in the top row (a-b) whereas the simulations are shown in the bottom row (c-d). Note that the model simulations have a bias of 0.6 K. Therefore, this value is added to the simulations to allow the reader to focus on the wake structure and not on the bias. The black lines along A-B and C-D denote the locations of the vertical cross-sections shown in Fig. 27(a-d) and (e-f). The black thick line in (a-b) shows location of the vertical profile of Fig. 21 appearing as a horizontal line and not as a dot because the aircraft needed  $\approx 10$  km in horizontal direction to climb from 60 AMSL to 1500 AMSL.

maximal values of  $11.8 \text{ g kg}^{-1}$  outside of the wake. Corresponding to the observations, the model simulates dryer air within the wake region with values around  $9.8 \text{ g kg}^{-1}$ . However, the simulations suggest lower water vapor mixing ratios to the west of the wake. The observations show values up to  $11.5 \text{ g kg}^{-1}$  whereas the model predicts values in the order of  $11 \text{ g kg}^{-1}$  (Fig. 26b).

Associated with the neutrally-stratified layer, dryer air is evident in the vertical cross-section A-B (Fig. 27b and d) 5 km downwind of the wind farm cluster. Similar to the potential temperature, it is most likely that the dryer air originated from the dryer layer aloft above 150 m AMSL. This height corresponds to the upper limit of the rotor area, emphasizing that air stemming from above the rotor area is mixed downwards. The mixing of air above the rotor area seems to be more pronounced in the model than in the observation. Within the upper rotor area, the model simulates a water vapor concentration of  $9.5 \text{ g kg}^{-1}$ , whereby the observations show concentrations in the order of  $10.2 \text{ g kg}^{-1}$ , indicating that dry air was entrained into too low elevations, due to enhanced vertical mixing into the farms as described in (e.g. ABKAR and PORTÉ-AGEL 2015; PAN et al. 2018).

### 4.3 Sensitivity experiment

In this section, the uncertainty of the simulations regarding the estimated thrust and power coefficients is assessed. The difference between the power and the thrust coefficients alone determines the fraction of energy that is extracted from the mean flow to turbulent kinetic energy by the wind farm parameterization (see equation 3). Consequently, varying only one coefficient within a large enough interval should cover the uncertainty that stems from the estimated wind farm coefficients.

Two sensitivity studies were conducted, by increasing and decreasing the thrust coefficient with respect to the thrust coefficient of the control simulation by ten percent, resulting in the thrust coefficients curves, denoted as  $c_{Tmax}$  and  $c_{Tmin}$  in Fig. 9. The WRF model simulates for the observational period, upwind of the wind farms, wind speeds within the interval of  $4.5 \text{ m s}^{-1}$  and  $7.0 \text{ m s}^{-1}$ . Therefore, the uncertainty of the power and thrust coefficient is restricted to this wind speed interval (see grey marked wind speed interval in Fig. 9). The empirical thrust coefficient function of MAGNUSSON (1999) gives for this wind speed interval, a thrust coefficient in the order of 0.8 and 0.85, whereby JIMÉNEZ et al. (2007) assume a thrust coefficient of 0.75 for winds speeds within  $7\text{-}10 \text{ m s}^{-1}$ . Therefore, our thrust coefficient interval from 0.776 to 0.946 should encompass the uncertainty.

The results of the sensitivity studies are shown in Fig. 28. To emphasize the effect of the varying thrust coefficient the difference between simulation without and with a wind farm parameterization is shown (i.e. simulation with wind farms - simulation without wind farms). The difference was calculated with hourly averaged data to achieve a clear signal of the wind farm parameterization.

All three simulations show similar results. All simulated wakes extend beyond 45 km downwind of the wind farms. Additionally, they do not differ much in their intensity. They all show a maximum wind speed reduction of  $-1.4 \text{ m s}^{-1}$ . As expected the simulation with the highest thrust coefficient  $c_{Tmax}$  shows the most pronounced

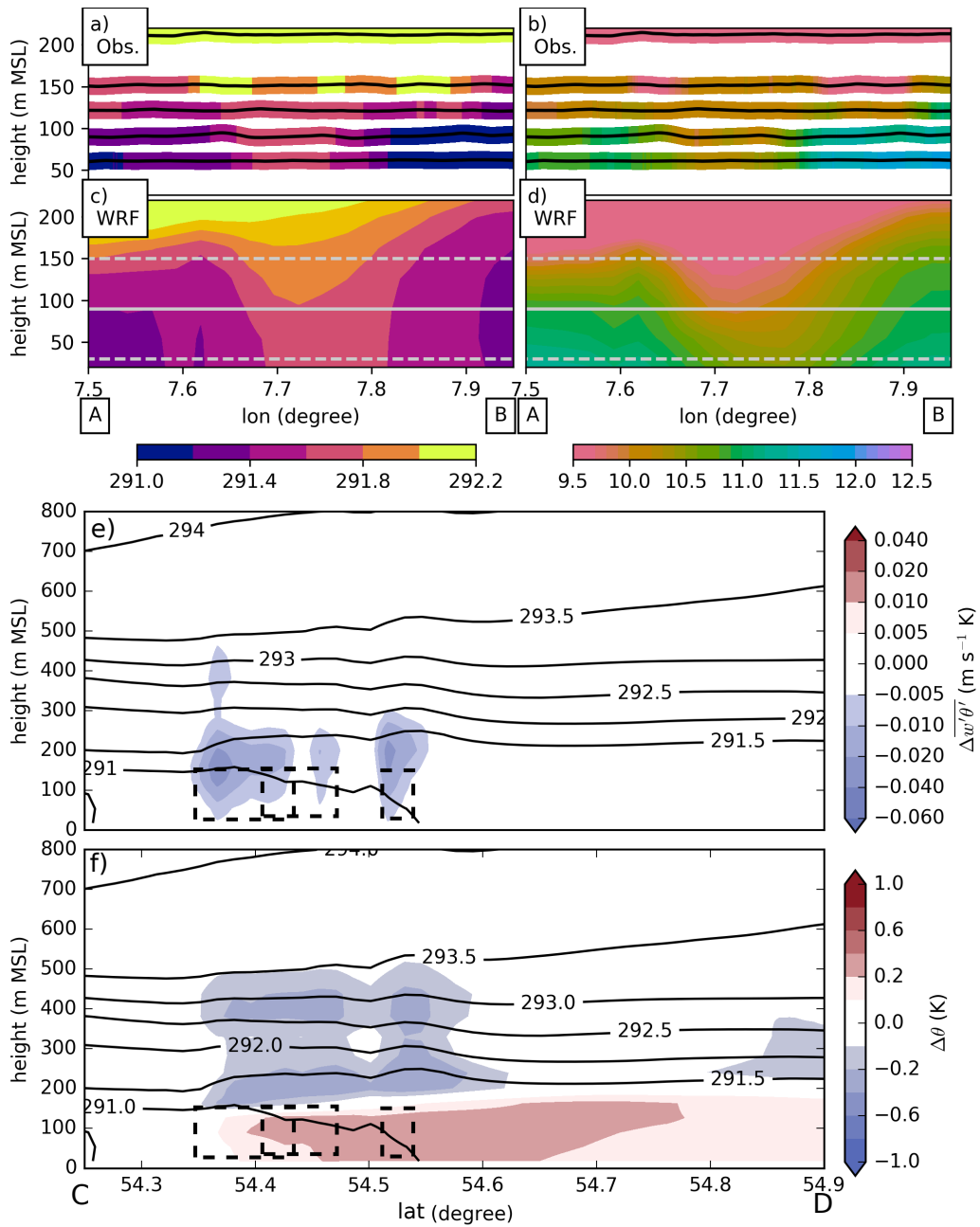


**Figure 27:** A comparison of observed (a-b) and simulated (c-d) potential temperature (a, c) and water vapor ratio (b, d) along the vertical cross-section A-B perpendicular to the mean flow. The simulations are shown at 10:00 UTC corresponding to the start of the observations. Further, the difference in sensible heat flux (e) and potential temperature (f) between a WF and NWF simulation is shown averaged from 08:00 UTC to 09:00 UTC. In (e) blue colors indicate an enhanced sensible heat flux downward, whereas in (f) blue contours indicate a cooling and red contours a warming caused by the existence of wind farms. Black lines in (a-b) denote the flight track whereas in (e-f) they show the potential temperature isolines of the WF simulation. The black and thick dashed boxes in (e-f) show the rotor area of the three wind farms.

wind speed reduction of  $-1.4 \text{ m s}^{-1}$ . However, the wind speed reduction differences in the simulations are not bigger than  $0.2 \text{ m s}^{-1}$ . From 30-45 km downwind, all simulations

show a wind speed reduction of 5 % (or  $-0.4 \text{ m s}^{-1}$ ).

All three simulations show an acceleration at the flanks of the wakes, whereby the acceleration at the left flank is more defined than on the right side looking into flow direction. Further, the acceleration is more pronounced for a higher thrust coefficient indicating that the acceleration is rooted in the mass continuity. The simulation  $c_{Tmin}$  shows only accelerations on the left flank with speed-ups of maximum  $0.4 \text{ m s}^{-1}$ , increasing to a defined streak with an increasing thrust coefficient. On the right flank of the wake, an acceleration is also visible, but the acceleration is below  $0.2 \text{ m s}^{-1}$  (i.e. below 5 %) and twice as broad as the wake.

The streak of wind speed reduction shown in all three simulations in the southwest is caused by the wind farm Godewind. This wake was not measured by the aircraft and is therefore not discussed in this study. However, the wind farm was considered in our simulations so as to be accommodate of any wake interactions.

## 4.4 Discussion

Herein, the results of section 4.2 and 4.3 are discussed and compared the observations executed on 10 September 2016 to all other observation conducted during the WIPAFF project downwind of large offshore wind farms to outline conditions that are favorable for wakes associated with an impact on temperature or water vapor (section 4.4.2).

### 4.4.1 Discussion of the wake simulations

The WRF model with the WFP of FITCH et al. (2012) simulated the wake generated by the wind farms AW, MSO and ONO reasonably well. The length and width of the wake were simulated correctly, although the upwind wind speed was too low.

Most likely, this wind speed deviation between model and observation is rooted in the neutrally stratified lower atmosphere (see Fig. 21) in the simulation. A more stable-stratified atmosphere would result in a more pronounced low-level jet and, hence, a vertical wind profile with higher wind speeds at hub height.

This neutrally stratified atmosphere is, in turn, caused by the overestimated cold air advection close to the coast (at FINO1). As shown in Fig. 21 the vertical potential temperature profile obtained by the aircraft was similar to the sounding of the island Norderney measured eight hours earlier at 0000 UTC, located approx. 100 km upwind of the wind farm ONO. Therefore, the upwind potential temperature profile was characterized by the nocturnal cooling over the land. The too-cold simulated upwind vertical potential temperature profile emphasizes that the WRF model overestimates the nocturnal cooling over land. Consequently, too cold air masses are advected over the North Sea in the model. This, in turn, causes a delayed warming of the atmosphere close to the coast and explains the model's temperature deviation at FINO1. Hence, the wrong stratification at FINO1 is most likely rooted in the overestimated night time cooling over land.

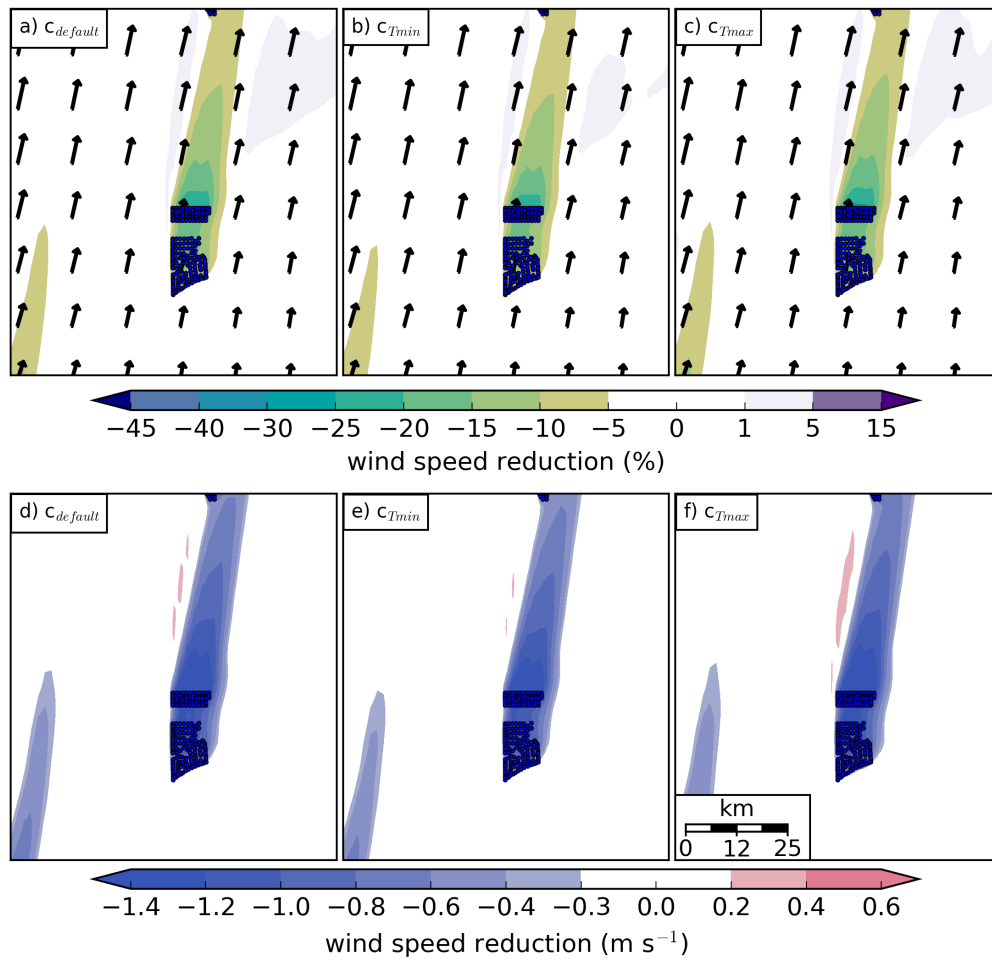


**Figure 28:** The sensitivity of the wind farm parameterization with respect to the varying thrust coefficients shown in Fig. 9. Panel (a), (b) and (c) show the relative wind speed deficit and speed up (colored contours) compared to a simulation without wind farms at 0900 UTC 10 September 2016. Panel (d)-(f) show the corresponding total change in wind speed in colored contours whereby blue and red contours indicate a wind speed deficit and speed up, respectively. All data used for this figure was averaged over one hour.

Another reason for the cold bias of the WRF model could be too enhanced mixing introduced by the boundary layer parameterization. According to SANDU et al. (2013) turbulent diffusion in numerical weather prediction models is mostly unrealistically high, resulting in difficulties representing stable boundary layers in atmospheric models. However, enhanced turbulent diffusion is, especially in operational models, necessary to obtain a correct deepening of cyclones and realistic high-pressure systems (SANDU et al. 2013). Summarized, high turbulent diffusion is necessary to capture the large scale flow but results in a weak representation of stable boundary layers. Whether this could be a reason for the cold bias or not is beyond the scope of this study, but is of major interest.

This deviation between the model and observed stratification at FINO1 raises the

question of whether the simulated wake is realistic. As the model has only difficulties capturing the stratification of the marine boundary layer close to the coast and not further downwind (i.e. the WRF model performed well at FINO3, see section 4.2.1) the modeled wake is asserted to be realistic.

An underestimation of the wind speed in the WRF model was already reported in previous works. HASAGER et al. (2015) compared wakes of wind speeds upwind and downwind of Horns Rev 1 from SAR images and WRF results. WRF captured the wind speed distribution around Horns Rev 1, but also underestimated the wind speed in the undisturbed flow and, hence, also within in the wake region. They noticed a deviation between WRF and SAR images outside of the wake in the order of  $1.5 \text{ m s}^{-1}$ , whereby within the wake they reported a deviation below  $1 \text{ m s}^{-1}$ . They compared 10 m winds retrieved from the satellite images against simulated winds at 10 m AMSL. These results correspond to our observations where a deviation of  $1.7 \text{ m s}^{-1}$  outside of the wake and  $0.5 \text{ m s}^{-1}$  inside the wake is present. Also HAHMANN et al. (2015) showed that regardless of the boundary conditions, WRF underestimates the wind speed at FINO1 for a simulation covering the year 2010. That indicates that the most potential for improvement of forecasting offshore wakes for this specific case is rooted in a better representation of the marine atmospheric boundary layer and not in the wind farm parameterization. This finding agrees with the result of chapter 3 and LEE and LUNDQUIST (2017), who also found that the main error is rooted in the background flow and not in the wind farm parameterization.

The simulated warming would have been warmer in case of a more pronounced inversion within the simulations. A stronger inversion over hub height would allow an enhanced sensible heat flux towards the surface resulting in a more pronounced warming at hub height similar to the observations.

Two reasons could be responsible for the too dry air at the lower portion of the wake. The lower neutrally stratified part of the atmosphere could be responsible for an overestimated mixing resulting in too dry air close to the surface. Secondly, although in chapter 3 it was shown that a TKE source of the WFP is necessary to obtain realistic results over wind farms under stable conditions, this work cannot proof whether the TKE source emits too much TKE at hub height causing exaggerated entrainment of dry air.

Deviations between observation and simulations that are introduced due to estimated thrust- and power coefficients are minor compared to the deviations caused by the background errors. This insensitivity was demonstrated by varying the thrust coefficient by  $\pm 10 \%$  and the wind speed deficit in the wake increased (decreased) by  $0.2 \text{ m s}^{-1}$ . Compared to a background deviation of up to  $1.9 \text{ m s}^{-1}$  this is a rather small source of error.

Our results showed that forecasting wind direction correctly is important for re-

alistic power predictions for offshore sites. This is in contrast to the finding of LEE and LUNDQUIST (2017) for an onshore site. They showed that the forecasted wind direction did not significantly influence the quality of the wind power forecast. This can be explained by the rather long wakes possible over the North Sea (as in this case study) compared to onshore sites. For example, the observed wake reached a length of up to 45 km. That means that a deviation between observed and simulated wind direction of 5 degrees leads to a 5 km displacement of the wake. These 5 km can be crucial as they can decide whether a downwind wind farm is affected by a wake or not.

Not all features in the observed wake can be resolved by a mesoscale model. For example, the strong gradient in wind speed and potential temperature at the western flank in the observed wake (Fig. 24) is a detail that cannot be resolved in a mesoscale simulation, because the grid size is too large. Similar to the findings in chapter 3 the argument of SKAMAROCK (2004) can be applied that physical solutions only exist for processes that have the size, seven times the grid spacing of the model. Consequently, a wind shear extending over 3 km can not be resolved by a mesoscale model. For such purposes, RANS, URANS, or large-eddy-simulations need to be applied.

#### 4.4.2 Comparison to other cases

Given the results from the case study of the 10 September 2016, one could conclude that an inversion in the vicinity of the rotor area is a sufficient constraint to observe a warming and drying at hub height downwind of large offshore wind farms. However, this assumption does not hold when analyzing the remaining 25 cases. For example, in the afternoon of the 10 September 2016, the aircraft flew a similar pattern as shown in Fig. 26, but did not observe any change in temperature and humidity although the atmosphere was characterized by an inversion at hub height (Fig. 29p) and a wake in wind speed was visible in the observations (not shown). The vertical profiles taken in the morning and afternoon differ mainly in terms of wind speed. In the afternoon the wind speed at hub height decreased from  $7 \text{ m s}^{-1}$  to values below  $6 \text{ m s}^{-1}$  compared to the measurements in the morning, suggesting that the wind speed has to be above a certain threshold to generate enough turbulence to mix the air and induce a warming or drying. Applying these two constraints - an inversion in the vicinity of the rotor area and wind speeds over  $6 \text{ m s}^{-1}$  at hub height to all 26 cases, eleven cases fulfill both criteria. Indeed, in eight of the eleven cases, a change was observed in temperature and wind speed (Fig. 30) and in all of them a clear change in wind speed deficit was observed downwind (Fig. 31). In two of the remaining cases a temperature change did not occur for certain. In the first case (Fig. 30f) a strong background gradient in potential temperature is present, hindering the observation of a change in temperature. In the second case (j, not shown) only measurements along the wake and, hence, measurements of any difference between wake and none wake air were not possible. In

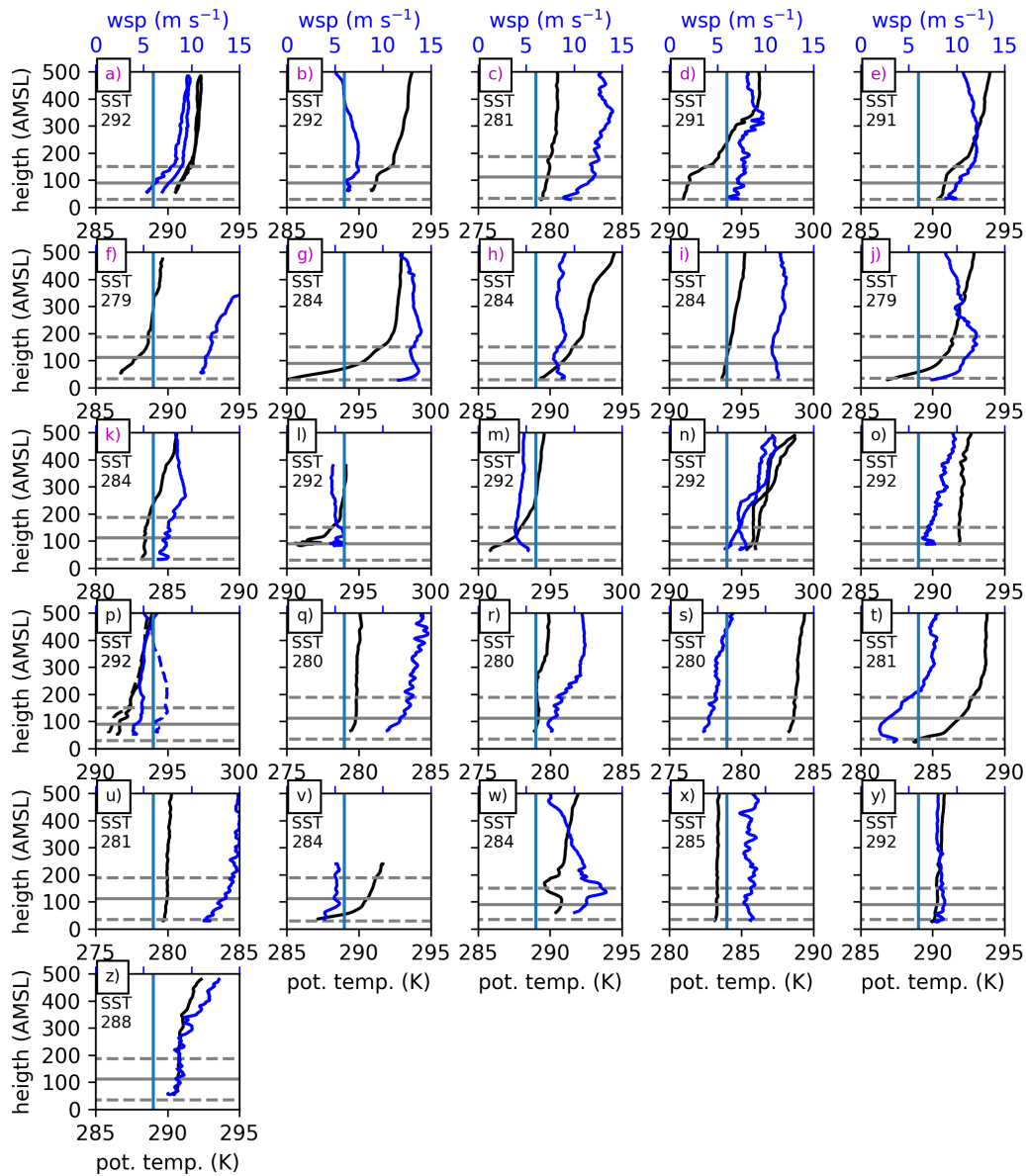


**Figure 29:** 26 vertical profiles taken by the aircraft corresponding to the 26 aircraft measurements used in this study as listed in table 2 with the SST measured at FINO1 (see location in Fig. 5). Black and blue lines show the potential temperature (K) and wind speed ( $\text{m s}^{-1}$ ), whereby the potential temperature refers to the x-axis at the bottom and the wind speed to the x-axis at the top (the coloring of the axis matches the coloring of the data). For a better comparison between the profiles, the wind speed limits are kept constant ( $0 \text{ m s}^{-1} - 15 \text{ m s}^{-1}$ ) and the spread of the potential temperature axis is always 10 K. The dashed and the solid gray lines indicate as in Fig. 27 the rotor area and the hub height. Note that the rotor areas and hub heights are not always the same because not all aircraft measurements were conducted at the same wind farm. The vertical light blue line marks the  $6 \text{ m s}^{-1}$  threshold. In (n) the dashed and solid lines show the measurements taken on 10 September 2016 in the morning and in the afternoon, respectively. The locations of the vertical profiles taken in (a-i) are shown in Fig. 29a-i) by a black thick line. The vertical profiles (a-k) fulfill the criteria defined in section 4.4 and are hence marked by a magenta numbering.

the third case (k, not shown) an impact on temperature was not observed, even though that the wind speed was above our defined threshold of  $6 \text{ m s}^{-1}$  and the atmosphere was stably stratified at rotor height (Fig. 29k). However, the measurements were conducted downwind of Godewind (see location in Fig. 6), a wind farm with fewer wind turbines than the wind farm cluster around Amrumbank West. Consequently, higher wind speeds are necessary to achieve the same amount of mixing, indicating that higher wind speeds would have been necessary to observe a change of temperature at hub height in this case. This assumption is underscored by the observation conducted on the 11 April 2017 (case c), where a warming was observed at Godewind associated with wind speeds of over  $10 \text{ m s}^{-1}$  at hub height.

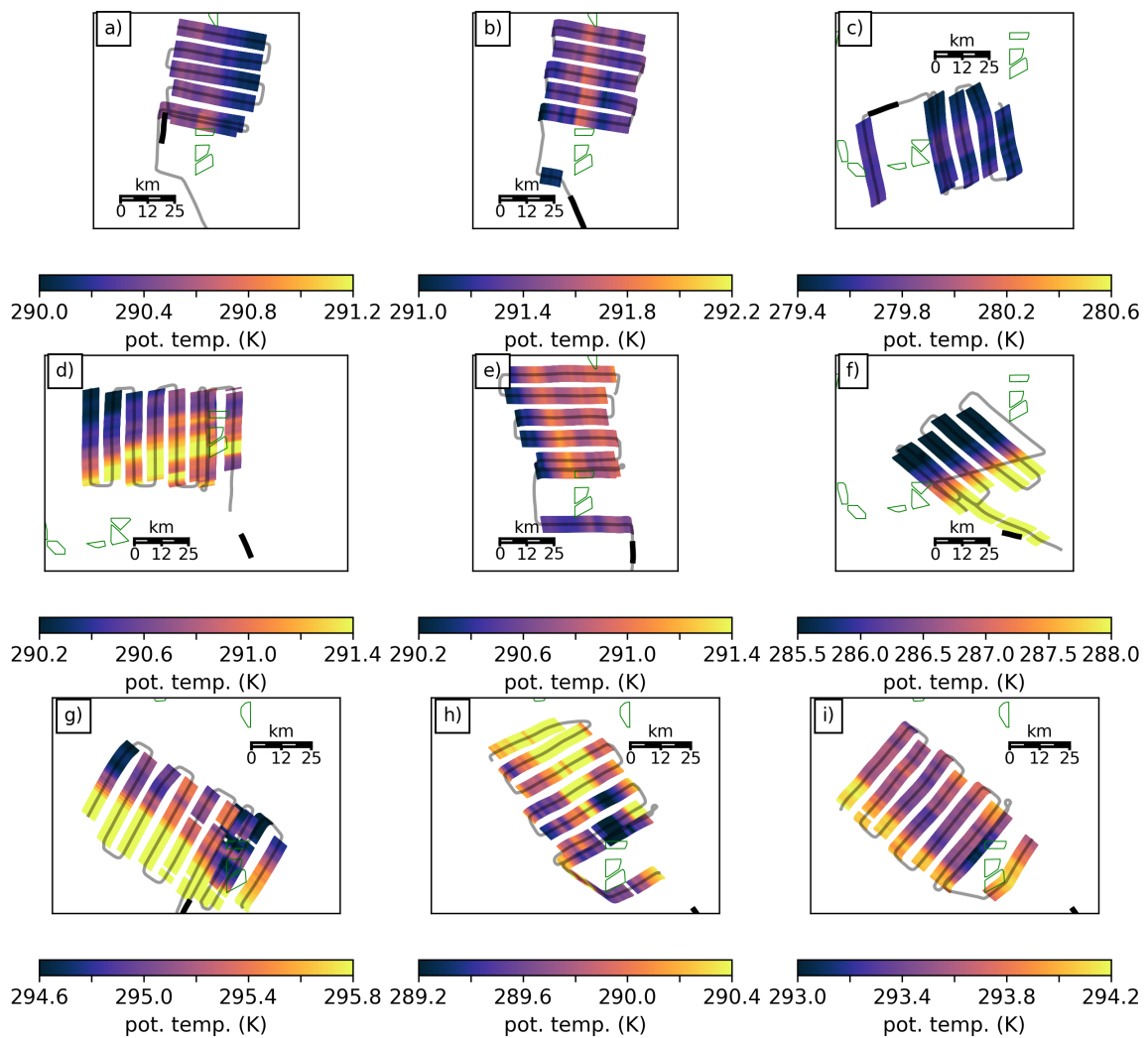


**Figure 30:** Potential temperature measured by the aircraft at hub height (i.e. 90 m for (a), (b), (d), (e), (g-i) and 111 m for (c) and (f)). An exception is the flight pattern shown in (g), in this case, the aircraft flew at 200 m AMSL. The potential temperature interval shown in all subplots is kept constant at 1.2 K for better comparison between the different measurements, except in (f). The corresponding vertical profiles of these observations are shown in Fig. 29 (a-i), whereby the locations of the profiles are marked by a black thick line.

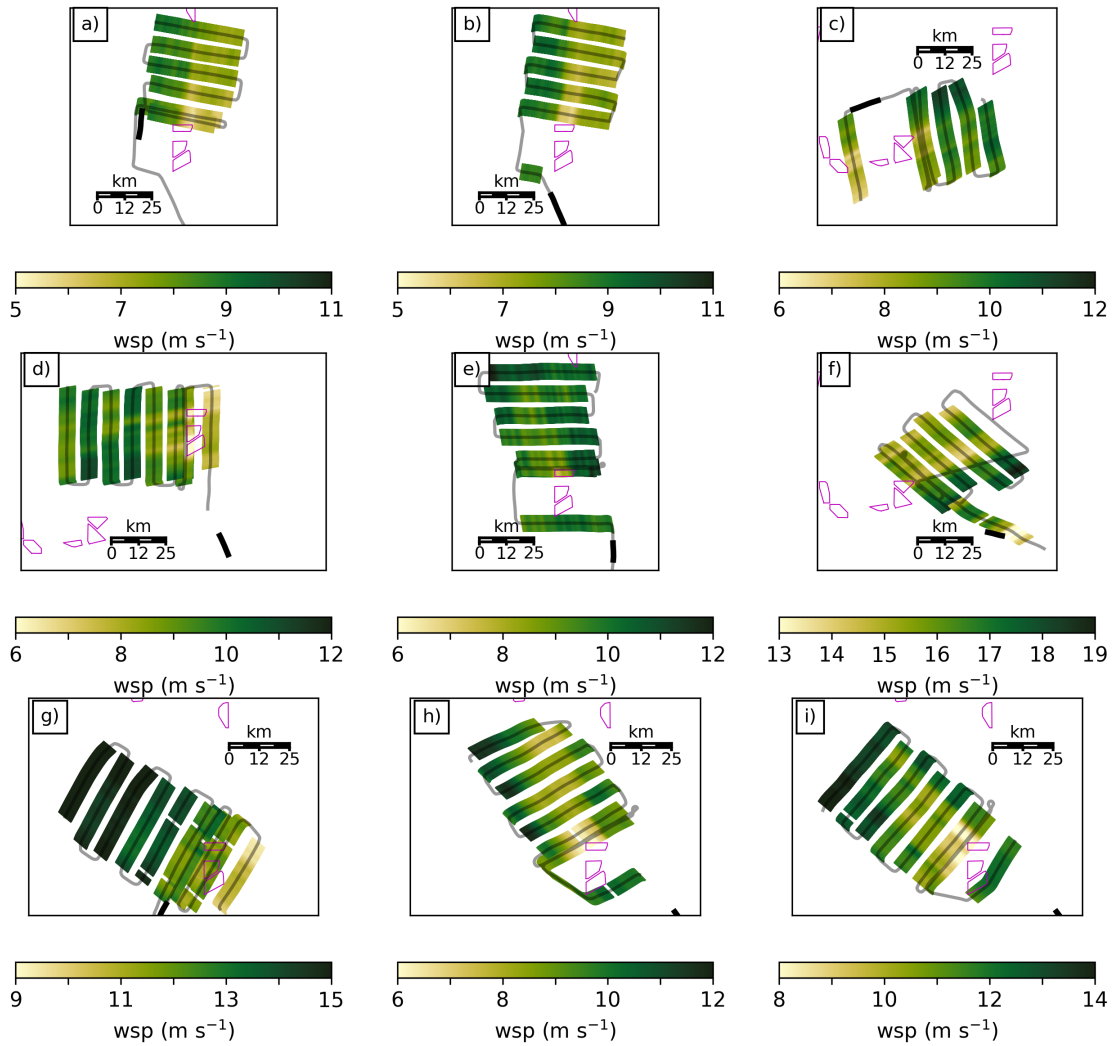


**Figure 31:** As Fig. 30, but for the wind speed. The wind speed interval shown in all subplots is kept constant at  $6.0 \text{ m s}^{-2}$ . The corresponding vertical profiles of these observations are shown in Fig. 29 (a-i), whereby the locations of the profiles are marked by a black thick line.

The height of the inversion (which is partially driven by SST) determines whether the wind farms warm or cool the atmosphere at hub height in stable conditions. In the cases shown in Fig. 30a-e) a warming is observed at hub height whereby in Fig. 30g-i) a cooling of the atmosphere was measured. In the warming cases, a pronounced inversion occurred above hub height accompanied by a less stable layer below, indicating that the enhanced negative heat fluxes in the wakes were stronger above than below the hub height. As a result, mixing of dry and warm air from above hub height dominates and causes an overall warming at hub height, as schematically indicated in Fig. 32a). In contrast, in Fig. 30g-i) cold SSTs were accompanied by inversions (Fig. 29g-i) located below rotor height, emphasizing that the enhanced negative heat fluxes in the wakes were stronger below than above the hub height, thus causing a net cooling at hub height (Fig. 32b).

These inversions that cause a cooling at hub height are suggested to be less than 30 m thick. For example, in Fig. 30i) we observe a cooling of up to 0.6 K although there is a constant lapse rate within most of the rotor area. However, the SST at FINO1 (see location in Fig. 6) was 284 K compared to a potential temperature of  $\approx 294$  K at 30 m AMSL, indicating that a shallow cold layer close to the ocean surface caused an inversion through the lower portion of the rotor area and below, thus cooling due to the enhanced mixing of this cool air within and partly below the rotor area caused the observed cooling.

The observed warming or cooling is decoupled from the drying downwind. For example, a warming in Fig. 30a-e) is observed and cooling in Fig. 30i) but in all measurements dryer air is seen downwind, meaning that the moisture flux is decoupled from the heat flux - a result in agreement with the findings of FOREMAN et al. (2017). However, in nine of the cases that fulfill the criteria for a potential change in temperature at hub height, six times a drying and only one time a humidification is observed at hub height. In the remaining two cases no change in humidity could be measured (case g-h), whereby in case (g) the aircraft was flying at 200 m AMSL - a height too high to detect any impact on the humidity (Fig. 27b).

MILLER and KEITH (2018a) simulated a warming due to onshore wind farms in the US. They even conclude that the warming caused by wind farms superimposes the cooling in the 2 m temperature due to a reduction of CO<sub>2</sub> emissions. However, as we have seen in this study, the warming results from a pure redistribution of air. However, a pure redistribution of air cannot superimpose the cooling in the 2 m temperature due to a reduction of CO<sub>2</sub> emissions. A more detailed look at the potential impacts of wind farms on the regional climate is provided in chapter 5.

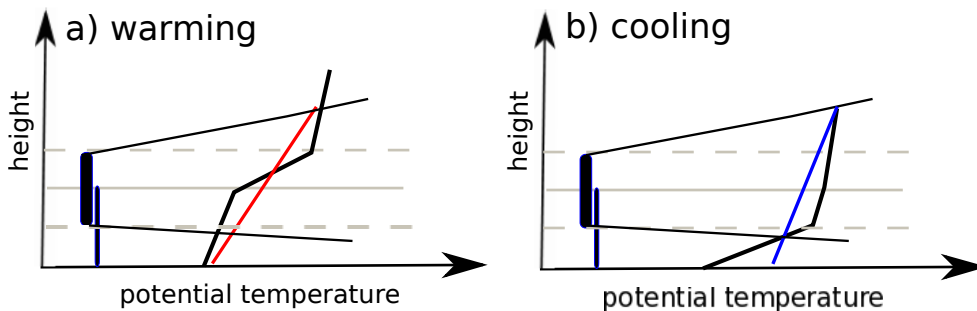


**Figure 32:** A schematic description of the observed (a) warming and (b) cooling at hub height downwind of large offshore wind farms. The dashed and the solid gray line indicate as in Fig. 27 the rotor area and the hub height. The potential temperature profiles upwind of the wind farms are shown with a black thick line, the impact on the potential temperature profiles of the wind farms is indicated in red (a) and blue (b).

## 4.5 Summary

The WFP of FITCH et al. (2012) has been evaluated for a cluster of offshore wind farms based on aircraft measurements. The aim was to test the WFP for a real case simulation. Therefore, it was also necessary to evaluate the model's ability to simulate the boundary layer upwind of the wind farms as the wake highly depends on the configuration of the upwind flow. These are the key findings:

- The deviation in background flow considering the wind speed dominates the deviation of the observed and simulated wake. A large scale southerly forcing advected continental air masses over the North Sea. These air masses were characterized by a nocturnal inversion at the beginning and by a mixed layer during the second half of our observation. Consequently, the stratification of the marine boundary layer was influenced by the boundary layer of the land upwind. The advection of the nocturnal inversion caused a weakly stratified marine boundary layer close to the coast as the advected air masses were colder than the SST. Later, air warmer than the SST was advected and a stable marine atmospheric boundary layer developed. The mesoscale Weather Research and Forecasting Model had problems resolving the transition of the marine boundary layer from stably to weakly stratified upwind of the wind farms. As the wind profile depends on the stability, the upwind wind speed was underestimated (i.e. up to  $1.9 \text{ m s}^{-1}$ ).
- The wind farm parameterization simulates the spatial dimensions of the wake well. Although, a deviation in the upwind flow at the transition area between land to open sea is observed, the model represents the atmosphere in the far wake region - 150 km away from the coast - well. Therefore, the parameterization represents the wind deficit measurable 45 km downwind of the wind farms. Additionally, the parameterization can represent the horizontal and vertical expansion of the wake 5 km downwind of the wind farms. In the observation and the simulations, a wind speed deficit and a change in temperature and water vapor is still clearly visible approximately 70 m above the upper end of the rotor area. However, the model tends to overestimate the vertical dimensions of the wake due to a too unstable boundary layer in the model. However, although the spatial dimensions agree with the observed ones, the absolute wind speed values disagree with the measurements. As the model underestimates the upwind wind speed, the wind speed within the wake is also lower than in the observations.
- Further, it was shown that deviations that are introduced due to uncertainties in the thrust and power coefficients only cause small deviations compared to the aforementioned deviation in the upwind flow. Underlining the findings of

chapter 3, showing that the processes above a wind farm are best represented in case of correct upwind conditions.

- Large offshore wind farms can have an impact on the MBL. Besides the obvious impact of wind farms on wind field, an increase in potential temperature by up to 0.6 K was observed within the wake of a large offshore wind farm 45 km downwind. This warming was associated with a decrease in the total water vapor mixing ratio by up to  $0.5 \text{ g kg}^{-1}$ . In contrast, a shallow inversion below hub height associated with a cold SST causes a cooling of the same magnitude above and at hub height downwind, as observed during three measurement flights.
- These micrometeorological impacts exist only in case of an inversion below or at rotor area. Only in the presence of such inversions can warmer air be mixed downward by the rotors. Depending on the height of the inversions, this process is causing either a warming or cooling at hub height. As an inversion acts as a lid for the water vapor evaporating from the ocean, the water vapor concentration is higher underneath the inversion. Consequently, a breakup of the inversion results in a mixing of dryer air downward and, hence, in dryer air within the wake. This process was observed regardless of a warming or cooling, indicating that the moisture flux is decoupled from the heat flux.

These results indicate that the performance of wind farm parameterizations is for stably stratified atmospheres limited by the performance of the driving mesoscale model in agreement with the findings in chapter 3. As many existing and planned wind farms are within 100 km the coast, boundary layer parameterizations that better represent the transition between land and the open sea are necessary.

## 5 Potential micrometeorological and regional climate impacts of large offshore wind farms on the atmospheric boundary layer

This chapter focuses on the impact of all potentially planned offshore wind farms in the North Sea. Two case studies characterized by stable conditions are presented, i.e. 10 September 2016 and 14 October 2017. These two case studies are chosen to be able to constrain the maximal possible impact of offshore wind farms on the MABL as the impact of offshore wind farms seems to be largest on the far-field in stably stratified atmospheres (see chapter 4). These results are partly based on the results published in SIEDERSLEBEN et al. (2018b). However, a more extensive future scenario is presented here, i.e. this thesis also takes into account the wind farms that were in the application process according to plans of the BSH in 2015 (i.e. red polygons in Fig. 5).

A single wind farm cluster can cause a warming of up to 0.6 K and a drying of  $\approx 0.5 \text{ g kg}^{-1}$  at hub height in the MABL according to the observations (chapter 4) in case of an inversion in vicinity of the rotor area. Consequently, the overall effect of all wind farms that are planned, operational and approved or under construction as they are shown in Fig. 5 (i.e. red polygons, orange and blue wind farms) is, hence, of interest. To answer this question, simulations for 10 September 2016 and 14 October 2017 were conducted including all potential areas of planned, accepted and existing offshore wind farms as they are shown in Fig. 5 (i.e. red polygons, orange and blue wind farms). The 10 September 2016 was characterized by offshore winds, whereas on 14 October 2017 the wind blew onshore arising the question of whether the land downwind was affected by the wakes of offshore wind farms.

For 10 September 2016 and the 14 October 2017 measurements along the cross-section A-B (Fig. 26) and I-J (Fig. 14, Fig. 16) were performed, agreeing with the simulated vertical and horizontal impact on temperature and humidity in the far-field and the impact on wind speed and TKE above the wind farm, respectively, making it possible to simulate the potential impact of existing and planned offshore wind farms.

### 5.1 Offshore winds and stable conditions

This section presents the possible impact of all potentially planned offshore wind farms under the weather conditions as observed on 10 September 2016 characterized by offshore winds.

The difference between the wind farm (WF) and no wind farm simulation (NWF) (Fig. 33) suggests a similar warming response (within  $\pm 0.1\text{K}$ ) to the case of September 10, 2016 in the presence of more wind farms. For example, downwind of the large wind farm cluster around Riffgrund, a wide area with a warming of up to 0.5 K is found (Fig. 33), while downwind of the large westernmost cluster the warming is less

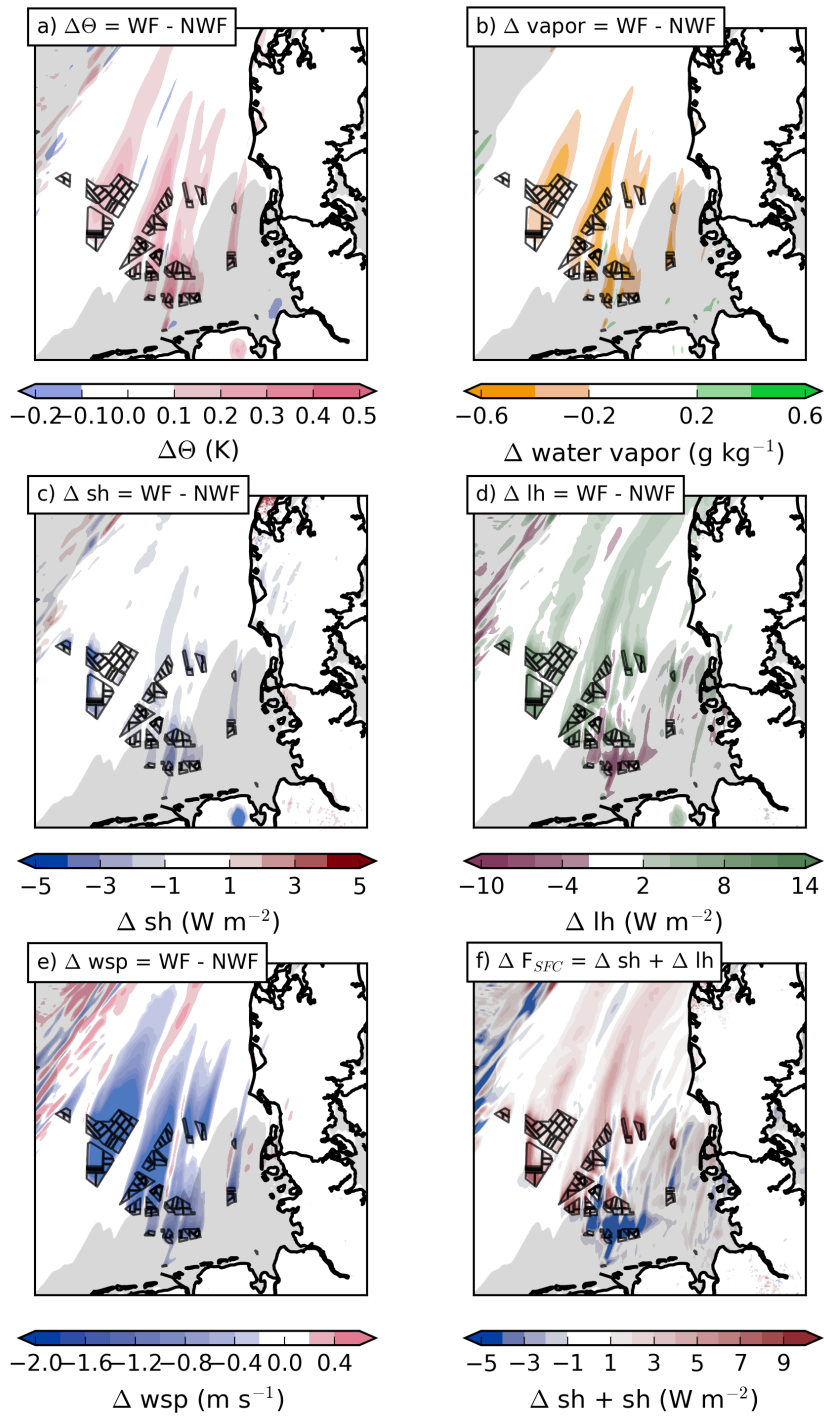


**Figure 33:** The impact of all potentially planned offshore wind farms at the North Sea on 10 September 2016 averaged from 08:00 UTC to 09:00 UTC. Shown is the difference at hub height of (a) potential temperature, (b) water vapor and (e) wind speed between a simulation with wind farms (WF) and a simulation with no wind farms (NWF). The resulting changes of sensible heat flux (sh) and latent heat flux (lh) are shown in (c) and (d). The sum of differences in sensible and latent heat flux is shown in (f). The gray shading depicts areas where the SST is higher than the air temperature.

than 0.4 K. However, not only the size of a wind farm seems to determine the degree of warming. The wind farm Riffgat with only 30 wind turbines causes also a warming

of up to 0.5 K. The simulation suggests a stronger warm air advection aloft at Riffgat and, hence, the inversion at Riffgat is even more pronounced and that in turn allows an even more enhanced downward mixing of warm air. In contrast, the warming at Riffgat is associated with a cooling on the eastern flank of the wake.

The impact of these large offshore wind farms on the water vapor at hub height is similar to the one observed on 10 September 2016. In contrast, to the simulated warming which extends over 150 km in length, the water vapor wakes reach a maximal length of 100 km. However, the super composition of the wakes of the already existing wind farms AW and Butendiek result already in a wake exceeding 100 km. Therefore, the future scenario here suggests no fortification of the drying effect.

The length of the wakes grows with the size of the wind farms. The largest offshore wind farm cluster having the westernmost location of all wind farms has the most pronounced wind deficit downwind associated with a wake exceeding 150 km. The wind speed deficit exceeds  $2 \text{ m s}^{-1}$  over large areas. However, also regions with increased wind speeds are present. The blocking of the large wind farms clusters causes an acceleration of the flow between their wakes due to mass continuity.

## 5.2 Onshore winds and stable conditions

Given the length of wakes during stable conditions, the question arises whether wakes of offshore wind farms can affect the boundary layer on land during an onshore wind event. Such conditions were observed on 14 October 2017 as shown in the satellite image Fig. 12, hence the impact of all potential wind farms is explored at the North Sea for this case study.

The difference between WF and NWF suggests a more pronounced warming on land than within the MABL (Fig. 34a). A warming is visible downwind of the northern wind farms, whereby the warming fortifies as soon the wakes reach the coast, i.e. from 0.3 K up to 0.5 K. Surprisingly, these areas do not correspond to the areas with a wind deficit as observed in the simulations of 10 September 2016.

The fortification of the warming onshore during onshore winds is rooted in the enhanced mixing over land as it is indicated in the cross-section along X-Y (corresponding to the mean wind direction) shown in Fig. 35. As expected, an enhanced sensible heat flux (Fig. 35a) is visible over and within the rotor areas (black boxes in Fig. 35). Corresponding to the enhanced sensible heat flux a warming is visible above hub height downwind of the wind farm AW (Fig. 35b). As this higher air is advected over land, the increased turbulence over land mixes the higher air towards the surface. Consequently, the warming seen in Fig. 34a) is most pronounced over land as the warming before is mostly pronounced above hub height.

Besides the enhanced sensible heat flux, the descending air masses downwind of the large offshore wind farm clusters contribute to the warming observed onshore. Although

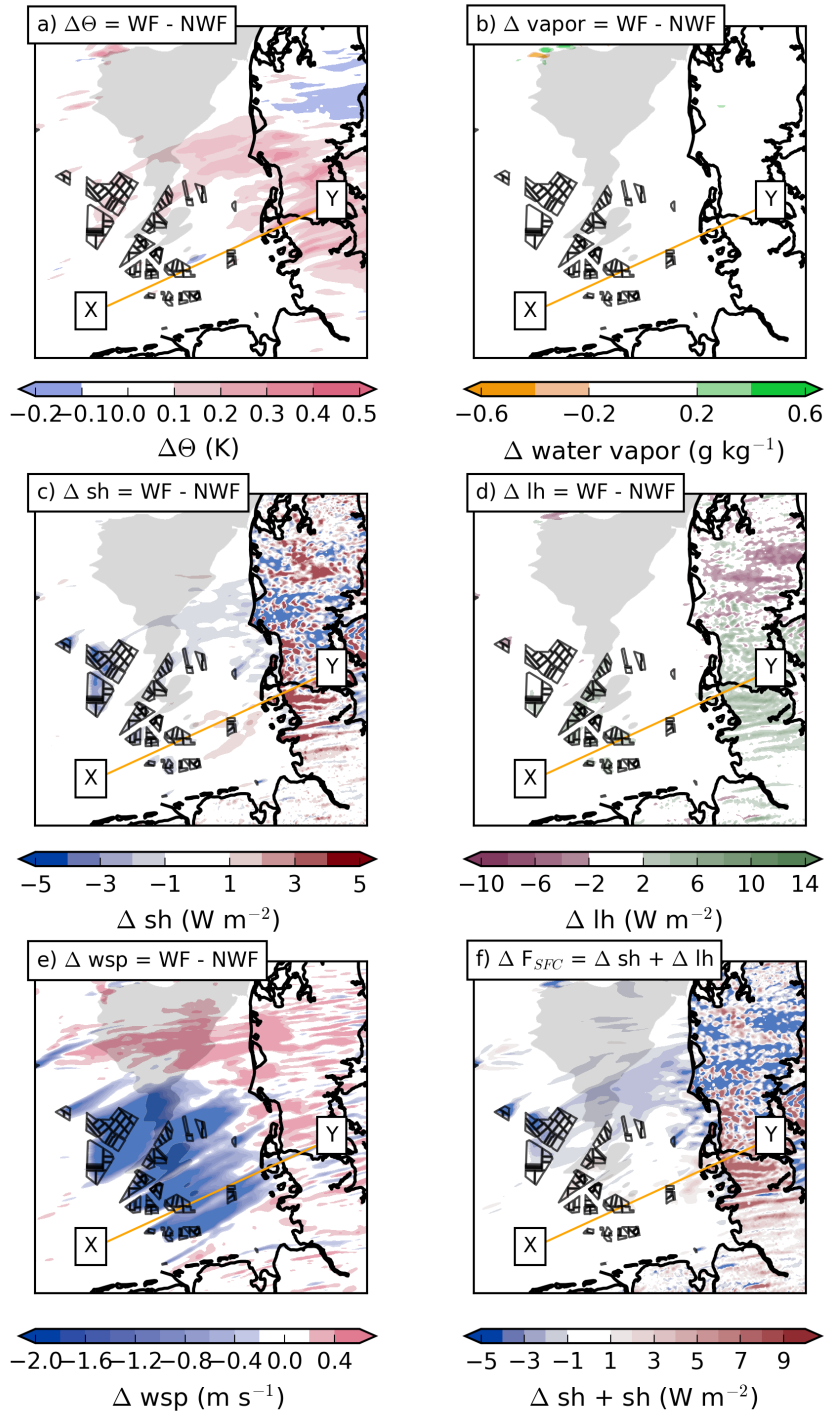


**Figure 34:** As Fig. 33, but on 14 October 2017, averaged from 14:00 UTC to 15:00 UTC. Additionally, the location of the cross-section along X-Y as shown in Fig. 35 is indicated by an orange solid line.

an enhanced sensible heat flux is simulated at the wind farm located between  $6.5^\circ$  E and  $7.0^\circ$  E (Fig. 35a) no warming is visible in Fig. 35b) compared to the wind farm AW. The upward and downward curvature of the lines of constant potential temperature indicate that deceleration induced by the wind farms (Fig. 34e) results in an enhanced flow over the wind farms, cooling and warming the air adiabatically upwind and downwind of

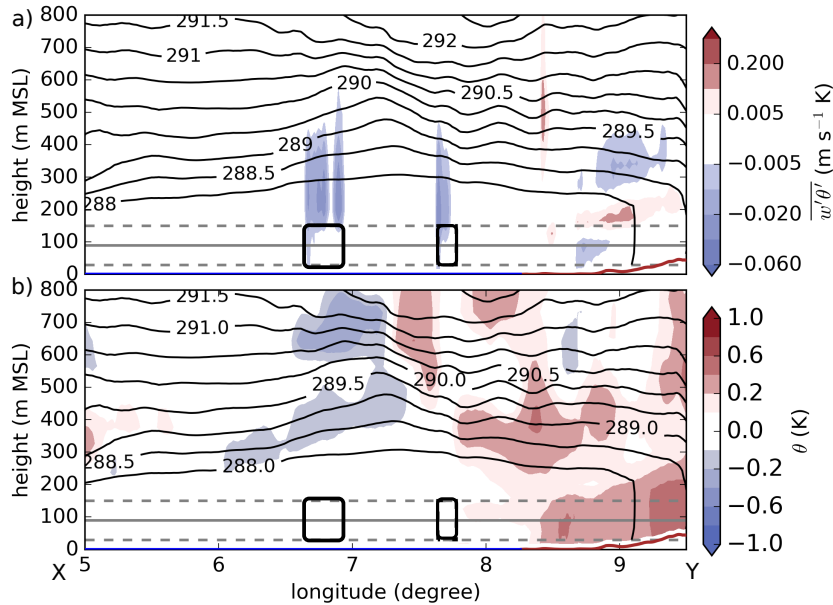


**Figure 35:** The difference in sensible heat flux (a) and potential temperature (b) between a WF and NWF simulation along the cross-section along X-Y as indicated in Fig. 34 averaged from 14:00 UTC to 15:00 UTC. In (a) blue colors indicate an enhanced sensible heat flux downward, whereas in (b) blue contours indicate a cooling and red contours a warming caused by the existence of wind farms. The black boxes in (a) and (b) indicate the rotor areas intersecting the cross-section. The blue and brown line indicate sea and topography, respectively.

the wind farm clusters, respectively, explaining the missing warming at the wind farm located between  $6.5^\circ$  E and  $7.0^\circ$  E corresponding to the upwind region. As the land corresponds to the area of descending air masses, the warming is more pronounced onshore than offshore.

In contrast to 10 September 2016, the wind farms had no impact on the water vapor concentration (Fig. 34b). A reason for this result is most likely rooted in the nonexistence of an inversion within the rotor area as it was the case on 10 September 2016. An inversion acts like a lid on the atmosphere, increasing the water vapor concentration below the inversion. As the lapse rate on 14 October 2017 was constant, no heterogeneity in the water vapor profile developed as seen in Fig. 21. Consequently, no water vapor could be mixed upward resulting in an unaffected water vapor concentration.

The wakes developing downwind of the large offshore wind farm clusters are 50 km shorter (Fig. 34e) than the wakes simulated on 10 September 2016 in terms of wind speed deficit most likely associated with the missing inversion on 14 October 2017 (Fig. 29). Nevertheless, the wake of the wind farms around AW are long enough to reach the islands south of Sylt.

### 5.3 Discussion

Given the simulated and observed impacts on temperature and water vapor, the question arises whether offshore wind farms can alter the regional climate. As pointed out in section 2.8, the pure redistribution of air and water vapor does not change the energy within a vertical column of the atmosphere (equation 5). However, as soon the redistribution of air and water vapor alters the sensible and latent heat flux at the surface, the energy changes within the atmosphere (equation 5). Therefore, the impact of all potential wind farms on the sensible (Fig. 33c, Fig. 34c) and latent heat flux (Fig. 33d, Fig. 34d) is discussed.

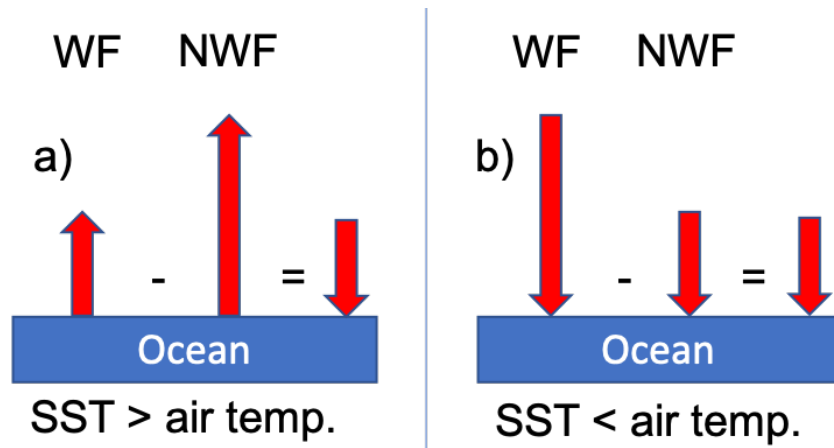


**Figure 36:** Schematic sketch of impact of offshore wind farms on the sensible heat flux in case of (a) a SST higher than the air temperature and (b) vice versa. WF is a wind farm simulation whereby a NWF is a simulation with the wind farm parameterization switched off - no wind farms.

The simulations show both a decreased sensible heat flux associated with the warming (Fig. 33c, Fig. 34c). Two different processes drive the reduction of the sensible heat flux rooted in the different temperature gradients between the SST and the lowest model level located at 17 m AMSL (Fig. 36). In Fig. 33c) and Fig. 34c) the area with an air temperature at the lowest model level lower than the SST is shaded in gray. In these regions, under undisturbed conditions the sensible heat flux is orientated upward, i.e. the ocean is warming the lower portion of the atmosphere (Fig. 36a). Warming near the ocean's surface induced by the wind farms results in these regions in a reduction of the sensible heat flux, hence, the difference between WF and NWF is negative (Fig. 36a). In contrast, the ocean areas having a lower SST than the ambient air temperature are characterized by sensible heat flux pointing downward, resulting in a warming of the ocean (Fig. 36b). In this case, a warming of the lower atmosphere results in an enhanced sensible heat flux towards the ocean. Consequently, the difference between WF and NWF simulation result in a net negative sensible heat flux, as well (Fig. 36b). Therefore, a warming of the air at the ocean's surface results,

regardless of the temperature gradient between SST and the air temperature, in a net cooling of the atmosphere.

The wind farms alter the sensible heat flux on land in the future scenario of 14 October 2017 but not on in the future scenario of 10 September 2016, except in the north-westerly part of Denmark (Fig. 34e). As expected, due to the onshore winds on 14 October 2017 and the associated warming on land downwind, the sensible heat flux is increased in the southern and the northern part of Denmark and Germany, respectively. This increase is accompanied by an unclear signal of the sensible heat flux at center and northern part of Denmark, suggesting more convective conditions to the northern part of the domain.

The latent heat flux is only altered in the future scenario of 10 September 2016, corresponding to the simulated changes in the water vapor concentration (Fig. 33d). In the northern part of the domain, the drying of the atmosphere corresponds to an increased latent heat flux into the atmosphere, i.e. moisture is transported from the ocean towards the atmosphere. However, in the regions with a higher SST than at the lowest model level, a negative difference between the WF and NWF is simulated, although the latent heat flux is supposed to increase due to the simulated drying. Hence, this study suggests, that in the areas with a higher SST than air temperature, the warming induced by the wind farms at the surface weakens the latent heat flux more than the enhancing effect due to the drying of the wind farms.

Despite the absence of changes in the water vapor concentration in the simulation of 14 October 2017, changes in the latent heat flux are visible on the land located downwind of the wind farms. The missing changes in the water vapor concentration suggest that the enhanced latent heat flux is rooted in the warming as seen in Fig. 34a). Warmer temperatures on land increase the evaporation and, hence, the latent heat flux.

Although both the 10 September 2016 and 14 October 2017 were characterized by stable conditions, the net impact of the offshore wind farms on sensible and latent heat flux have opposite signs (Fig. 33f, Fig. 34f). The simulated net impact (i.e. the sum of net latent and sensible heat flux) for 10 September 2016 suggest a net cooling within the regions where the SST is higher than the ambient air, whereas a net warming is simulated in the regions with a higher air temperature than SST. In contrast, the simulation of the 14 October 2017, show a dominating net cooling effect over the ocean associated with the nonexistent impact on the water vapor concentration. Additionally, on 14 October 2017, a net warming impact is visible on the land located downwind of large offshore wind farm clusters.

In contrast to XIA et al. (2019), this study could not identify any changes in the net longwave radiation. XIA et al. (2017, 2019) investigated the impact of an onshore wind farm on the land surface temperature (LST) by the use of MODIS data and a numerical setup similar to the one used in this study. For cloud-free conditions (i.e.

the integrated cloud liquid path had to be below  $0.02 \text{ kg m}^{-2}$  over and next to the wind farm), they observed a clear warming within the wind farm region and a cooling downwind, resulting in an increased net longwave radiation (pointing upward) during night-time. Given the high water vapor mixing ratios above the North Sea, the net longwave radiation is also influenced by the water vapor, hence, we suggest that the high water vapor content causes the noisy signal in the radiation budget terms.

Summarized, the net effect of offshore wind farms on the regional climate during stable conditions cannot be answered with this model setup. The two cases investigated here are characterized by a warming as schematically sketched in Fig. 32a), hence the sensible heat flux is altered such, regardless of the temperature gradient between SST and the ambient air, that a net decrease of the sensible heat flux is caused by the wind farms. In case the enhanced mixing induced by the wind farms results in a cooling of the air over the ocean, a net increase in the sensible heat flux is expected. The impact of the wind farms on the latent heat flux is determined by the temperature gradient between SST and the ambient air. Consequently, the net impact of offshore wind farms is dependent on the temperature gradient between SST and the air temperature and whether a cooling or a warming is induced by the mixing of offshore wind farms, that, is in turn, related to the inversion height (see chapter 4). As the SST underlies the yearly cycle only year-long observations and simulations can investigate the overall impact of offshore wind farms on the regional climate. However, to represent the inversion height correctly with a mesoscale model is challenging due to the complex interactions between coastal regions and open oceans as discussed in chapter 4. Additionally, it was not possible with the used model setup to obtain a clear impact of wind farms on the radiation at the surface and at the top of the atmosphere, although these terms impact the energy content of a vertical column (equation 5). For this purpose, idealized simulations may give a clearer result.

## 5.4 Summary

Based on the evaluations conducted in the chapters 3 and 4, this chapter explored the impact of all potentially planned and existing wind farms on the boundary layer and discussed potential implications for the regional climate, by presenting two case studies, the 10 September 2016 and 14 October 2017. The impact on the boundary was determined by considering the difference of a simulation with wind farms (WF) and no wind farm (NWF). As the impacts of wind farms on the regional climate are not driven by the pure redistribution of air and water vapor, the sensitivity of the latent and sensible heat flux with respect to offshore wind farms was explored. Additionally, this study tried to investigate the impact of offshore wind farms on the radiation budget at the top and bottom of the atmosphere, but obtained no clear results, hence, these results are omitted in this thesis. These are the main findings:

- The net impact on the sensible heat flux on the MABL is determined by the inversion height. This study has shown that wind farms can warm and cool the air temperature at the surface depending on the inversion height in chapter 4. Consequently, the net effect on the sensible heat flux is determined by the inversion height. A cooling above the ocean's surface results in a net increase of the sensible heat flux, and a warming vice versa.
- A change in the latent heat flux within MABL is only observed in case of a strong inversion in the vicinity of the rotor area, allowing a drying within the wakes of the wind farms. An inversion over the ocean acts as a lid, allowing an increase of the water vapor mixing ratio below as observed on 10 September 2016. The enhanced mixing induced by the wind farms transports dryer air downward, resulting in an increased latent heat flux in regions with a higher air temperature than SST. In contrast, in regions with an opposite temperature gradient a decreased latent heat flux was simulated, indicating that the weaker temperature gradient, induced by the enhanced mixing, predominates the simulated change in the latent heat flux.
- The latent and sensible heat flux on land were only affected during onshore winds as simulated for the 14 October 2017 case study. Although, the simulations show only subtle warming downwind of the wind farms within the marine boundary layer, a clear warming signal was simulated on land located downwind associated with a cooling further north. Consistently, the warming corresponds with areas of increased sensible and latent heat flux. However, the cooling does not result in a clear decrease of the sensible or latent heat flux, indicating a more convective atmosphere to the north indicated additionally by the higher SST than the air temperatures further north.

Whether wind farms impact the regional climate or not can not be answered with the used method of just two simulations, covering only one day. How wind farms affect the regional climate is not only dependent on the frequency of stable conditions offshore, additionally the temperature gradient between air temperature and SST and the inversion height, in case of any, is of major importance. This degree of freedom is not covered with the two case studies executed in this thesis, hence, no conclusion on possible impacts of offshore wind farms on regional climate is given here.

## 6 Conclusion and outlook

This chapter summarizes this thesis based on the open questions formulated in chapter 1 (section 1.2) and points out possible future research in the field of mesoscale wind farm modeling.

### 6.1 Main results and conclusions

This study analyzed the impact of the wind farm parameterization (WFP) of FITCH et al. (2012) on the marine atmospheric boundary layer (MABL) by the use of airborne measurements, focusing on three scales: wind farm scale (100 m – 10 km), wake scale (i.e. 1 km – 100 km) and regional scale (20 km – 250 km). As the processes above large offshore wind farms are crucial to represent the far-field of offshore wind farms, this thesis started with an evaluation of the simulated turbulent kinetic energy above offshore wind farms to obtain the most suited numerical setup to capture the enhanced turbulent kinetic energy on a wind farm scale followed by an evaluation of the far-field (i.e. wake scale). Given the success with the representation of the impacts of large offshore wind farms on the MABL on a wind farm and wake scale, we explored the potential impact of all offshore wind farms that will be possibly installed at the North Sea on a regional scale - during on- and offshore winds. These are the main findings of this thesis:

- a) The impact of offshore wind farms on the turbulent kinetic energy above wind farms can only be represented for simulations capturing the background flow. Three case studies were investigated at two different sites, all characterized by stable conditions. During two case studies, the impinging flow was influenced by the land upwind causing deviations between the observed and simulated vertical wind- and temperature profiles. However, during one case study, the marine boundary layer was not influenced by any land upwind resulting in simulations capturing the background flow. Based on these simulations, the optimal model configuration for the WFP was obtained. Sensitivity experiments revealed that mesoscale simulations with horizontal grids in the order of 5 km and finer can represent the effect of offshore wind farms on the marine atmospheric boundary layer (MABL) in combination with the WFP of FITCH et al. (2012). However, due to the not sufficiently resolved enhanced TKE induced by the wind farms, it is necessary to add additional TKE into the atmospheric model during stable conditions, otherwise, the enhanced mixing of the wind farms is underestimated, consistently corresponding with an overestimation of the wind speed above the wind farms.

The impact of offshore wind farms was not represented for simulations with a horizontal grid spacing of 16 km although the additional TKE was induced by

the WFP. Consequently, studies based on simulations estimating the impact of large offshore wind farms with a horizontal grid spacing larger than 16 km (e.g., VAUTARD et al. 2014; MILLER et al. 2015) underestimate the impact of offshore wind farms during stable conditions.

- b) The WFP of FITCH et al. (2012) represents the impact of large offshore wind farms on the far-field in terms of wind speed, potential temperature and water vapor at hub height. Simulations representing the wake of the wind farms around Amrumbank West (AW) were executed and evaluated by aircraft measurements taken in the wake region at hub height (i.e. 90 m AMSL). Besides a wind speed deficit in the order of  $0.5 \text{ m s}^{-1}$ , a warming and a drying was observed and simulated at hub height 45 km downwind of the wind farms. The simulated warming and drying were in the same order of magnitude as observed, 0.5 K and  $0.5 \text{ g kg}^{-1}$ , respectively. However, the atmosphere was neutrally stratified below 60 m AMSL in the simulations, in contrast, the observation showed stable conditions below 60 m AMSL in proximity to the coast. Therefore, the vertical wake structure was more pronounced in the simulations than in the observations. Additionally, the deviations in the stratification explain the underestimated wind speed in the simulations upwind of the wind farms as the vertical momentum flux is more pronounced during neutral conditions resulting in a vertical wind profile with less vertical shear. The simulations with such deviation between observed and simulated stratification of the MABL close to the coast were all characterized by offshore winds, indicating that the simulations have problems representing the transition from the shore to the open sea during offshore winds. Nevertheless, the length and vertical extent of the wake can be simulated with a WFP during stable conditions, using the WFP configuration as described above.

An analysis of 23 additional airborne measurements executed in the far-field of offshore wind farms revealed that offshore wind farms have an impact on the potential temperature at hub height only in case of stable conditions and an inversion in the vicinity of the rotor area. The height of such inversion determines whether a warming or a cooling is observed at hub height in the far-field of offshore wind farms. Shallow inversions close to the surface are most likely to result in a cooling whereas inversions located over hub height result in a warming with the constraint that the wind speed is high enough to enable sufficient turbulent vertical mixing by the rotors of the wind farm. This wind speed threshold depends on the wind turbine density and size of the wind farm. For the wind farms considered in this thesis, wind speeds over  $6 \text{ m s}^{-1}$  were necessary to observe an impact on temperature. Impacts on potential temperature were not always accompanied by impacts on the water vapor concentration at hub height.

- c) Based on the successful evaluation of the wind farm parameterization above and downwind of offshore wind farms we explored a future scenario including all potentially planned offshore wind farms of the German Bight to discuss potential regional climate impacts. This thesis investigated two case studies, both characterized by stable conditions, as the evaluations revealed that the impact of offshore wind farms on the MABL is largest during stable conditions. These two case studies were chosen as they are different in their synoptic pattern: offshore vs. onshore winds, raising the question of whether wakes can influence the boundary layer on land during onshore winds. The simulations revealed that in both case studies the interactions of several wakes results in wakes exceeding a length of 100 km, as planned offshore wind farm clusters have a width of more than 50 km, the horizontal extent of the wakes have similar dimensions. According to the simulations the impact on temperature and water vapor at hub height is in the same order of magnitude as observed for the wind farms around Amrum-bank West. Consequently, more wind farms result only in a larger area affected by the temperature and moisture changes during stable conditions, but not in a fortification of the impacts.

Offshore wind farms only have an influence on the regional climate in case they influence the turbulent fluxes at the surface, i.e. the redistribution of the air masses observed at hub height is also effective at the surface resulting in a change of temperature and moisture gradients between air and sea surface and consequently in a change of the sensible and latent heat flux. The net impact of offshore wind farms on the sensible and latent heat flux depends in turn on the sign of the gradient between SST and air temperature and the height of the inversion, in case of any. A warming induced by wind farms at the sea surface results in a net cooling regardless of the temperature gradient between SST and air temperature. In contrast, a net warming is most likely in case of an inversion, located such that a cooling is induced at the sea surface within the far-field of offshore wind farms. The latent heat flux is influenced by offshore wind farms especially in case of an inversion in the vicinity of the rotor area. An inversion acts like a lid for the water vapor, i.e. the water vapor concentration is larger below the inversion than above. Consequently, a breakup of the inversion induced by the enhanced mixing of the wind farms results in dryer air at the surface increasing the latent heat flux, i.e. increasing the transport of water vapor into the boundary layer. However, the enhancement of the latent heat flux is not purely driven by the water vapor gradient but also by the temperature gradient between air temperature and SST. Thus, also the effect of offshore wind farms on the surface air temperature affects the net impact on the latent heat flux. In case of a warming, the simulations suggest an increased latent heat flux for regions with a higher air temperature

than SST and vice versa.

The overall impact of offshore wind farms on the regional climate could not be answered in this study due to the large variability of impacts. As pointed out above, the net impact of offshore wind farms depends on the lapse rate in the vicinity of the rotor height, wind speed and temperature gradient between SST and air temperature. This degree of freedom was not covered by investigating only two case studies. Additionally, implications of the water vapor concentration on the radiation budget were not studied in detail as the background noise in the radiation was larger than the impact of the wind farms on the radiation scheme.

## 6.2 Suggestions for further studies

Given the fact that a lot of offshore wind farms are built in proximity to the coast, boundary layer schemes that can resolve the transition from coastal regions to the open sea are necessary. In all simulations conducted within the framework of this thesis, simulations that were characterized by offshore winds struggled to represent the transition of the boundary layer from on- to offshore sites. The deviations increased with the strength of the inversion. For example, the inversion for case study III (chapter 3) was observed at rotor height (Fig. 29), in contrast, the simulated inversion was located above the rotor area. However, the location of the inversion is crucial for simulating the correct length of the wake and estimating the impact on the MABL as discussed in chapter 4 and 5. Hence, improving the boundary layer scheme at the shore would result by now in a greater improvement of the wake simulations than improving the WFPs in case of offshore winds.

To be able to improve a boundary scheme in the proximity of the shore the source of error has to be identified. All simulations with offshore winds had a cold bias. Several processes could lead to such a cold bias. First of all, too cold air advected from land upwind could cause such a cold bias. Thus, weather stations located onshore should be used to evaluate the performance of the model onshore. Secondly, enhanced turbulent diffusion could lead to a too neutrally stratified atmosphere resulting in a cold bias at hub height and a warm bias at the surface (Fig. 21), as pointed out by SANDU et al. (2013). Thirdly, a finer representation of the land use classes could be necessary to represent the processes onshore realistically. This suggestion is motivated by the results of DÖRENKÄMPER et al. (2015) who showed that the wind field offshore is highly influenced by the surface roughness onshore in case of offshore winds. Further, it is known that the land type influences the sensible and latent heat flux onshore (e.g. SHAO et al. 2013). Vertical profiles taken by the aircraft, as shown in this study, downwind of different land types could be taken to determine the influence of different land surface types on the MABL. However, preliminary sensitivity tests using the same land surface classification as in DÖRENKÄMPER et al. (2015) indicated no improvements

considering the cold bias.

Based on the results of this study the impact of offshore wind farms on the marine boundary layer should be studied based on simulations having a resolution of 5 km or finer, ideally with a boundary layer scheme that can reproduce shallow inversions as the height of the inversions is driving the net impact of offshore wind farms on the temperature at the surface, i.e. an overall warming or cooling of the boundary layer. Such simulations should cover ideally a period of 30 years. However, given the high computational cost of such simulations, a first step would be to cover periods of two years similar to the simulations of PRYOR et al. (2018b) and SUN et al. (2018) investigating the impact of onshore wind farms. Such regional climate simulations should not only identify the regions that are affected by a temperature or water vapor change, additionally, they should identify whether a high number of offshore wind farms clusters as shown in Fig. 33 and Fig. 34 impacts regional circulations like the sea breeze. For example, it could be possible that a warming due to offshore wind farms onshore, as seen in chapter 5 in section 5.1 could result in an earlier start of the sea breeze circulation during daytime.

Wind energy research should focus on the interactions of wind farm clusters and coastal areas due to the rising number of wind farms and their close proximity to the coast. In the North Sea the wind farm Gemini 1,2 and the wind farm Godewind mark the start and end point of a wind farm cluster that is approximately 80 km long orientated along a west-east axis. The minimum distance between the wind farms within this wind farm cluster is smaller than 15 km when taking the wind farms into account that are planned or under construction along this axis (Fig. 5). All wind farms that are planned, approved or potentially build to the north of these wind farms will be exposed to wakes or pronounced shear lines for wind direction from south-west to south-east. Note, this wind direction is typical for warm air advection resulting in stable conditions as it was observed for the case study presented in chapter 4. Based on the findings of this thesis, it can be expected that the wind farms located downwind of this wind farm cluster will experience higher fatigue and lower wind speeds resulting in lower yields. Additionally, the satellite image taken on 14 October 2017 reveals that even nowadays wind farm clusters are large enough to experience different wind speeds either due to varying distances to the shore or land surface types. For example, the wind farm Riffgrund 1 is exposed to streaks of increased wind speeds most likely due to surface roughness variability of islands located north of the Netherlands. Therefore, it should be investigated whether changes in the surface roughness (i.e. urbanization of coastlines) could influence the energy harvesting of offshore wind farm clusters.

Given the large size of offshore wind farm clusters, large scale wind speed reduction of wind farm clusters could trigger gravity waves. Due to mass continuity a deceleration induced by wind farm clusters and the associated blocking results in an enhanced flow

over and/or around wind farm clusters depending on the height of the turbines installed within the wind farms, size of the cluster, wind speed and atmospheric stability. The enhanced flow over wind farm clusters is equal to a vertical lift for air parcels going over the wind farms as indicated in Fig. 35 that in turn can trigger gravity waves. Gravity waves transport momentum and, hence, could interact with wakes of offshore wind farm clusters. Consequently, gravity waves should be considered in case wakes of offshore wind farm clusters are investigated.

Summarized, capturing the upwind state of the atmosphere is the most important ingredient to simulate the interactions between wind farms and the MABL on the wind farm, wake and regional scale.

## Bibliography

- ABKAR, M., F. PORTÉ-AGEL, 2015: A new wind-farm parameterization for large-scale atmospheric models. – *Journal of Renewable and Sustainable Energy* **7**, 013121, DOI: 10.1063/1.4907600.
- ALLAERTS, D., J. MEYERS, 2018: Gravity waves and wind-farm efficiency in neutral and stable conditions. – *Boundary-Layer Meteorol* **166**, 269–299, DOI: 10.1007/s10546-017-0307-5.
- ARMSTRONG, A., R.R. BURTON, S.E. LEE, S. MOBBS, N. OSTLE, V. SMITH, S. WALDRON, J. WHITAKER, 2016: Ground-level climate at a peatland wind farm in Scotland is affected by wind turbine operation. – *Environ. Res. Lett.* **11**, 044024.
- BEAUCAGE, P., M. BROWER, N. ROBINSON, C. ALONGE, 2012: Overview of six commercial and research wake models for large offshore wind farms. – *Proceedings of the European Wind Energy Associate (EWEA)*
- BODINI, N., J.K. LUNDQUIST, A. KIRINCICH, 2019: U.s. east coast lidar measurements show offshore wind turbines will encounter very low atmospheric turbulence. – *Geophysical Research Letters* **46**, 5582–5591, DOI: 10.1029/2019GL082636.
- BOETTCHER, M., P. HOFFMANN, H.J. LENHART, K.H. SCHLÜNZEN, R. SCHOETTER, 2015: Influence of large offshore wind farms on north german climate. – *Meteorologische Zeitschrift* **24**, 465–480, DOI: 10.1127/metz/2015/0652.
- BROWER, M.C., N.M. ROBINSON, 2012: The openwind deep-array wake model: development and validation. Technical report, AWS Truepower, Albany (NY), USA.
- BRÜMMER, B., G. MÜLLER, D. SCHRÖDER, A. KIRCHGÄSSNER, J. LAUNIAINEN, T. VIHMA, 2003: The eight balticos field experiments 1998–2001 over the baltic sea. – *International BALTEX Secretariat, Publication Series 138*.
- BUNDESNETZAGENTUR, 2017: Anlagenregister. Available online at [https://www.bundesnetzagentur.de/DE/Sachgebiete/ElektrizitaetundGas/Unternehmen\\_Institutionen/ErneuerbareEnergien/ZahlenDatenInformationen/EEG\\_Registerdaten](https://www.bundesnetzagentur.de/DE/Sachgebiete/ElektrizitaetundGas/Unternehmen_Institutionen/ErneuerbareEnergien/ZahlenDatenInformationen/EEG_Registerdaten).

- CALAF, M., C. MENEVEAU, J. MEYERS, 2010: Large eddy simulation study of fully developed wind-turbine array boundary layers. – *Physics of Fluids (1994-present)* **22**, 015110, DOI: 10.1063/1.3291077.
- CALAF, M., M.B. PARLANGE, C. MENEVEAU, 2011: Large eddy simulation study of scalar transport in fully developed wind-turbine array boundary layers. – *Physics of Fluids (1994-present)* **23**, 126603, DOI: 10.1063/1.3663376.
- CHARNOCK, H., 1955: Wind stress on a water surface. – *Quarterly Journal of the Royal Meteorological Society* **81**, 639–640.
- CHATTERJEE, F., D. ALLAERTS, U. BLAHAK, J. MEYERS, VAN N. LIPZIG, 2016: Evaluation of a wind-farm parametrization in a regional climate model using large eddy simulations. – *Quart. J. Roy. Meteor. Soc.* **142**, 3152–3161, DOI: 10.1002/qj.2896.
- CHEN, F., J. DUDHIA, 2001: Coupling an Advanced Land Surface-Hydrology Model with the Penn State-NCAR0 MM5 Modeling System. Part I: Model Implementation and Sensitivity. – *Mon. Wea. Rev.* **129**, 569–585, DOI: 10.1175/1520-0493(2001)129;0569:CAALSH;2.0.CO;2.
- CHRISTIANSEN, M.B., C.B. HASAGER, 2005: Wake effects of large offshore wind farms identified from satellite SAR. – *Remot. Sens. of Environ.* **98**, 251–268, DOI: 10.1016/j.rse.2005.07.009.
- COPERNICUS CLIMATE CHANGE SERVICE (C3S), 2018: ERA5: Fifth generation of ECMWF atmospheric reanalyses of the global climate. – Copernicus Climate Change Service Climate Data Store (CDS)
- CORSMEIER, U., R. HANKERS, A. WIESER, 2001: Airborne turbulence measurements in the lower troposphere onboard the research aircraft Dornier 128-6, D-IBUF. – *Meteorol. Z.* **10**, 315–329, DOI: 10.1127/0941-2948/2001/0010-0315.
- DJATH, B., J. SCHULZ-STELLENFLETH, B. CAÑADILLAS, 2018: Impact of atmospheric stability on X-band and C-band synthetic aperture radar imagery of offshore windpark wakes. – *Journal of Renewable and Sustainable Energy* **10**, 043301.
- DÖRENKÄMPER, M., M. OPTIS, A. MONAHAN, G. STEINFELD, 2015: On the Offshore Advection of Boundary-Layer Structures and the Influence on Offshore Wind Conditions. – *Boundary-Layer Meteorol* **155**, 459–482, DOI: 10.1007/s10546-015-0008-x.
- EMEIS, S., 2010a: Meteorological explanation of wake clouds at Horns Rev wind farm. – *DEWI Magazin* **37**, 52–55.

- EMEIS, S., 2010b: A simple analytical wind park model considering atmospheric stability. – *Wind Energ.* **13**, 459–469, DOI: 10.1002/we.367.
- EMEIS, S., 2018: *Wind energy meteorology: atmospheric physics for wind power generation* – Springer, 114–115.
- EMEIS, S., S. SIEDERSLEBEN, A. LAMPERT, A. PLATIS, J. BANGE, B. DJATH, J. SCHULZ-STELLENFLETH, T. NEUMANN, 2016: Exploring the wakes of large offshore wind farms. – *J. Phys.: Conf. Ser.* **753**, 092014.
- ERIKSSON, O., J. LINDVALL, S.P. BRETON, S. IVANELL, 2015: Wake downstream of the lillgrund wind farm—a comparison between les using the actuator disc method and a wind farm parametrization in wrf. – In: *Journal of Physics: Conference Series*, volume 625, 012028. IOP Publishing, DOI: 10.1088/1742-6596/625/1/012028.
- FITCH, A.C., J.B. OLSON, J.K. LUNDQUIST, J. DUDHIA, A.K. GUPTA, J. MICHALAKES, I. BARSTAD, 2012: Local and Mesoscale Impacts of Wind Farms as Parameterized in a Mesoscale NWP Model. – *Mon. Wea. Rev.* **140**, 3017–3038, DOI: 10.1175/MWR-D-11-00352.1.
- FITCH, A.C., J.K. LUNDQUIST, J.B. OLSON, 2013: Mesoscale influences of wind farms throughout a diurnal cycle. – *Mon. Wea. Rev.* **141**, 2173–2198, DOI: 10.1175/MWR-D-12-00185.1.
- FOREMAN, R., B. CAÑADILLAS, T. NEUMANN, S. EMEIS, 2017: Measurements of heat and humidity fluxes in the wake of offshore wind turbines. – *Journal of Renewable and Sustainable Energy* **9**, 053304, DOI: 10.1063/1.5003811.
- FRANSEN, S., R. BARTHELMIE, S. PRYOR, O. RATHMANN, S. LARSEN, J. HØJSTRUP, M. THØGERSEN, 2006: Analytical modelling of wind speed deficit in large offshore wind farms. – *Wind Energ.* **9**, 39–53, DOI: 10.1002/we.189.
- FRIEHE, C., W. SHAW, D. ROGERS, K. DAVIDSON, W. LARGE, S. STAGE, G. CRESCENTI, S. KHALSA, G. GREENHUT, F. LI, 1991: Air-sea fluxes and surface layer turbulence around a sea surface temperature front. – *J. Geophys. Res.* **96**, 8593–8609, DOI: 10.1029/90JC02062.
- FRUEHMANN, R., 2016: Relative calibration process for long term thermal stratification measurements in the lower atmospheric boundary layer. – *DEWI Magazin*
- HAHMANN, A.N., C.L. VINCENT, A. PEÑA, J. LANGE, C.B. HASAGER, 2015: Wind climate estimation using WRF model output: method and model sensitivities over the sea. – *Int. J. Climatol.* **35**, 3422–3439, DOI: 10.1002/joc.4217.

- HASAGER, C.B., M. NIELSEN, P. ASTRUP, R. BARTHELMIE, E. DELLWIK, N.O. JENSEN, B.H. JØRGENSEN, S. PRYOR, O. RATHMANN, B. FUREVIK, 2005: Offshore wind resource estimation from satellite sar wind field maps. – *Wind Energ.* **8**, 403–419, DOI: 10.1002/we.150.
- HASAGER, C.B., L. RASMUSSEN, A. PEÑA, L.E. JENSEN, P.E. RÉTHORÉ, 2013: Wind farm wake: The Horns Rev photo case. – *Energies* **6**, 696–716.
- HASAGER, C.B., P. VINCENT, J. BADGER, M. BADGER, A. DI BELLA, A. PEÑA, R. HUSSON, P.J. VOLKER, 2015: Using Satellite SAR to Characterize the Wind Flow Around Offshore Wind Farms. – *Energies* **8**, 5413–5439, DOI: 10.3390/en8065413.
- HASAGER, C.B., N.G. NYGAARD, P.J. VOLKER, I. KARAGALI, S.J. ANDERSEN, J. BADGER, 2017: Wind farm wake: The 2016 Horns Rev photo case. – *Energies* **10**, 317.
- HUNTER, J.D., 2007: Matplotlib: A 2d graphics environment. – *Computing In Science & Engineering* **9**, 90–95, DOI: 10.1109/MCSE.2007.55.
- IACONO, M.J., J.S. DELAMERE, E.J. MLAWER, M.W. SHEPHARD, S.A. CLOUGH, W.D. COLLINS, 2008: Radiative forcing by long-lived greenhouse gases: Calculations with the AER radiative transfer models. – *J. Geophys. Res.* **113**, DOI: 10.1029/2008JD009944.
- IVANOVA, L.A., E.D. NADYOZHINA, 2000: Numerical simulation of wind farm influence on wind flow. – *Wind Engineering* **24**, 257–269, DOI: 10.1260/0309524001495620.
- JACOBSON, M.Z., C.L. ARCHER, 2012: Saturation wind power potential and its implications for wind energy. – *Natl. Acad. Sci.* **109**, 15679–15684, DOI: 10.1073/pnas.1208993109.
- JENSEN, N.O., 1983: A note on wind generator interaction. Technical report, Risø National Laboratory (Risø-M-2411), Risø, Roskilde, Denmark.
- JIMÉNEZ, A., A. CRESPO, E. MIGOYA, J. GARCIA, 2007: Advances in large-eddy simulation of a wind turbine wake. – *J. Phys.: Conf. Ser.* **75**, 012041.
- JIMÉNEZ, P.A., J. NAVARRO, A.M. PALOMARES, J. DUDHIA, 2015: Mesoscale modeling of offshore wind turbine wakes at the wind farm resolving scale: a composite-based analysis with the Weather Research and Forecasting model over Horns Rev. – *Wind Energ.* **18**, 559–566, DOI: 10.1002/we.1708.

- KAIN, J.S., 2004: The Kain–Fritsch Convective Parameterization: An Update. – *J. Appl. Meteor. Climatol.* **43**, 170–181, DOI: 10.1175/1520-0450(2004)043;0170:TKCPAU;2.0.CO;2.
- KEITH, D.W., J.F. DECAROLIS, D.C. DENKENBERGER, D.H. LENSCHOW, S.L. MALYSHEV, S. PACALA, P.J. RASCH, 2004: The influence of large-scale wind power on global climate. – *Proc Acad Sci USA* **101**, 16115–16120, DOI: 10.1073/pnas.0406930101.
- LADWIG, W., 2019: wrf-python (version 1.3.0) [software]. Technical report, UCAR, NCAR, Boulder, Colorado, USA.
- LANGE, B., S. LARSEN, J. HØJSTRUP, R. BARTHELMIE, 2004: The influence of thermal effects on the wind speed profile of the coastal marine boundary layer. – *Boundary-Layer Meteorology* **112**, 587–617.
- LEE, J.C.Y., J.K. LUNDQUIST, 2017: Evaluation of the wind farm parameterization in the Weather Research and Forecasting model (version 3.8.1) with meteorological and turbine power data. – *Geosci. Model Dev.* , DOI: 10.5194/gmd-2017-128.
- LI, X., L. CHI, X. CHEN, Y. REN, S. LEHNER, 2014: Sar observation and numerical modeling of tidal current wakes at the east china sea offshore wind farm. – *Journal of Geophysical Research: Oceans* **119**, 4958–4971, DOI: 10.1002/2014JC009822.
- LI, Y., E. KALNAY, S. MOTESHARREI, J. RIVAS, F. KUCHARSKI, D. KIRK-DAVIDOFF, E. BACH, N. ZENG, 2018: Climate model shows large-scale wind and solar farms in the Sahara increase rain and vegetation. – *Science* **361**, 1019–1022, DOI: 10.1126/science.aar5629.
- LIM, K.S.S., S.Y. HONG, 2010: Development of an effective double-moment cloud microphysics scheme with prognostic cloud condensation nuclei (CCN) for weather and climate models. – *Mon. Wea. Rev.* **138**, 1587–1612, DOI: 10.1175/2009MWR2968.1.
- LUNDQUIST, J., K. DUVIVIER, D. KAFFINE, J. TOMASZEWSKI, 2018: Costs and consequences of wind turbine wake effects arising from uncoordinated wind energy development. – *Nature Energy* **1**, DOI: <https://doi.org/10.1038/s41560-018-0281-2>.
- MAGNUSSON, M., 1999: Near-wake behaviour of wind turbines. – *Journal of Wind Engineering and Industrial Aerodynamics* **80**, 147–167, DOI: 10.1016/S0167-6105(98)00125-1.
- MANGARA, R.J., Z. GUO, S. LI, 2019: Performance of the wind farm parameterization scheme coupled with the weather research and forecasting model under multiple

- resolution regimes for simulating an onshore wind farm. – *Adv. Atmos. Sci.* **36**, 119–132.
- MANN, J., D.H. LENSCHOW, 1994: Errors in airborne flux measurements. – *J. Geophys. Res.* **99**, 14519–14526.
- MELAS, D., 1998: The depth of the stably stratified internal boundary layer over the sea. – *Geophysical Research Letters* **25**, 2261–2264.
- MILLER, L.M., D.W. KEITH, 2018a: Climatic impacts of wind power. – *Joule* **in press**, DOI: 10.1016/j.joule.2018.09.009.
- MILLER, L.M., D.W. KEITH, 2018b: Observation-based solar and wind power capacity factors and power densities. – *Environ. Res. Lett.* **13**, 104008, DOI: 10.1088/1748-9326/aae102.
- MILLER, L.M., N.A. BRUNSELL, D.B. MECHEM, F. GANS, A.J. MONAGHAN, R. VAUTARD, D.W. KEITH, A. KLEIDON, 2015: Two methods for estimating limits to large-scale wind power generation. – *Proceedings of the National Academy of Sciences* **112**, 11169–11174, DOI: 10.1073/pnas.1408251112.
- MILLER, S., B. KEIM, R. TALBOT, H. MAO, 2003: Sea breeze: Structure, forecasting, and impacts. – *Rev. Geophys.* **41**, DOI: 10.1029/2003RG000124.
- NAKANISHI, M., H. NIINO, 2004: An improved Mellor–Yamada level-3 model with condensation physics: Its design and verification. – *Boundary-Layer Meteorol* **112**, 1–31, DOI: 10.1023/B:BOUN.0000020164.04146.98.
- NAKANISHI, M., H. NIINO, 2006: An improved mellor–yamada level-3 model: Its numerical stability and application to a regional prediction of advection fog. – *Boundary-Layer Meteorol* **119**, 397–407, DOI: 0.1007/s10546-005-9030-8.
- NEUMANN, T., K. NOLOPP, K. HERKLOTZ, 2004: First operating experience with the FINO1 research platform in the North Sea. – *DEWI Magazin* **24**, 27–32.
- NYGAARD, N.G., 2014: Wakes in very large wind farms and the effect of neighbouring wind farms. – *J. Phys.: Conf. Ser.* **524**, 012162.
- NYGAARD, N.G., S.D. HANSEN, 2016: Wake effects between two neighbouring wind farms. – *J. Phys.: Conf. Ser.* **753**, 032020, DOI: 10.1088/1742-6596/753/3/032020.
- ØRSTED, 2019: Energiewende. Available online at <https://energiewinde.orsted.de/trends-technik/vindeby-erster-offshore-windpark-daenemark>.

- PAN, Y., C.L. ARCHER, 2018: A hybrid wind-farm parametrization for mesoscale and climate models. – *Boundary-Layer Meteorol* 1–27, DOI: doi.org/10.1007/s10546-018-0351-9.
- PAN, Y., C. YAN, C.L. ARCHER, 2018: Precipitation reduction during hurricane harvey with simulated offshore wind farms. – *Environ. Res. Lett.* **13**, 084007, DOI: 10.1088/1748-9326/aad245.
- PLATIS, A., S.K. SIEDERSLEBEN, J. BANGE, A. LAMPERT, K. BAERFUSS, R. HANKERS, B. CANADILLAS, R. FOREMAN, J. SCHULZ-STELLENFLETH, B. DJATH, T. NEUMAN, S. EMEIS, 2018: First in situ evidence of wakes in the far field behind offshore wind farms. – *Scientific Reports* **8**, 2163, DOI: 10.1038/s41598-018-20389-y.
- PORTÉ-AGEL, F., Y.T. WU, H. LU, R.J. CONZEMIUS, 2011: Large-eddy simulation of atmospheric boundary layer flow through wind turbines and wind farms. – *J. Wind Eng. Ind. Aerodyn.* **99**, 154–168, DOI: 10.1016/j.jweia.2011.01.011.
- PORTER, D.F., J.J. CASSANO, M.C. SERREZE, 2011: Analysis of the Arctic atmospheric energy budget in WRF: A comparison with reanalyses and satellite observations. – *Journal of Geophysical Research: Atmospheres* **116**, DOI: https://doi.org/10.1029/2011JD016622.
- POSSNER, A., K. CALDEIRA, 2017: Geophysical potential for wind energy over the open oceans. – *Proc Acad Sci USA* **114**, 11338–11343, DOI: 10.1073/pnas.1705710114.
- PRYOR, S., R. BARTHELMIE, A. HAHMANN, T. SHEPHERD, P. VOLKER, 2018a: Downstream effects from contemporary wind turbine deployments. – In: *J. Phys.: Conf. Series*, volume 1037, 072010. IOP Publishing, DOI: 10.1088/1742-6596/1037/7/072010.
- PRYOR, S., R. BARTHELMIE, T. SHEPHERD, 2018b: The influence of real-world wind turbine deployments on local to mesoscale climate. – *Journal of Geophysical Research: Atmospheres* **123**, DOI: doi.org/10.1029/2017JD028114.
- RAJEWSKI, D.A., E.S. TAKLE, J.K. LUNDQUIST, S. ONCLEY, J.H. PRUEGER, T.W. HORST, M.E. RHODES, R. PFEIFFER, J.L. HATFIELD, K.K. SPOTH, OTHERS, 2013: Crop wind energy experiment (cwex): observations of surface-layer, boundary layer, and mesoscale interactions with a wind farm. – *Bull. Amer. Meteor. Soc.* **94**, 655–672, DOI: 10.1175/BAMS-D-11-00240.1.
- RAJEWSKI, D.A., E.S. TAKLE, J.K. LUNDQUIST, J.H. PRUEGER, R.L. PFEIFFER, J.L. HATFIELD, K.K. SPOTH, R.K. DOORENBOS, 2014: Changes in fluxes of heat,

- h 2 o, and co 2 caused by a large wind farm. – *Agricultural and forest meteorology* **194**, 175–187, DOI: 10.1016/j.agrformet.2014.03.023.
- ROY, S.B., J.J. TRAITEUR, 2010: Impacts of wind farms on surface air temperatures. – *Proc Acad Sci USA* **107**, 17899–17904, DOI: 10.1073/pnas.1000493107.
- SANDU, I., A. BELJAARS, P. BECHTOLD, T. MAURITSEN, G. BALSAMO, 2013: Why is it so difficult to represent stably stratified conditions in numerical weather prediction (nwp) models?. – *Journal of Advances in Modeling Earth Systems* **5**, 117–133, DOI: 10.1002/jame.20013.
- SATHE, A., S.E. GRYNING, A. PEÑA, 2011: Comparison of the atmospheric stability and wind profiles at two wind farm sites over a long marine fetch in the north sea. – *Wind Energy* **14**, 767–780, DOI: 10.1002/we.456.
- SHAO, Y., S. LIU, J.H. SCHWEEN, S. CREWELL, 2013: Large-eddy atmosphere–land–surface modelling over heterogeneous surfaces: Model development and comparison with measurements. – *Boundary-layer meteorology* **148**, 333–356.
- SHIMADA, S., T. OHSAWA, T. KOGAKI, G. STEINFELD, D. HEINEMANN, 2015: Effects of sea surface temperature accuracy on offshore wind resource assessment using a mesoscale model. – *Wind Energ.* **18**, 1839–1854.
- SIEDERSLEBEN, S.K., A. PLATIS, J.K. LUNDQUIST, A. LAMPERT, K. BÄRFUSS, B. CAÑADILLAS, B. DJATH, J. SCHULZ-STELLENFLETH, J. BANGE, T. NEUMANN, S. EMEIS, 2018a: Evaluation of a wind farm parametrization for mesoscale atmospheric flow models with aircraft measurements. – *Meteorologische Zeitschrift* **27**, 401–415, DOI: 10.1127/metz/2018/0900.
- SIEDERSLEBEN, S.K., J.K. LUNDQUIST, A. PLATIS, J. BANGE, K. BÄRFUSS, A. LAMPERT, B. CAÑADILLAS, T. NEUMANN, S. EMEIS, 2018b: Micrometeorological impacts of offshore wind farms as seen in observations and simulations. – *Environ. Res. Lett.* **13**, 124012.
- SIEDERSLEBEN, S.K., A. PLATIS, J.K. LUNDQUIST, J. BANGE, B. DJATH, K. BÄRFUSS, A. LAMPERT, B. CAÑADILLAS, J. SCHULZ-STELLENFLETH, NEUMANN, S. EMEIS, 2019: Observed and simulated TKE of large offshore wind farms. – *Geosci. Model Dev. Discuss.* **accepted for publication**.
- SIMPSON, J.E., 1994: *Sea breeze and local winds* – Cambridge University Press.
- SKAMAROCK, W., J. KLEMP, J. DUDHIA, D. GILL, D. BARKER, M. DUDA, X. HUANG, W. WANG, J. POWERS, 2008: A description of the advanced research WRF version 3, NCAR. Technical report, Mesoscale and Microscale Meteorology

- Division, National Center for Atmospheric Research, Boulder, Colorado, USA [Available online at [www2.mmm.ucar.edu/wrf/users/docs/](http://www2.mmm.ucar.edu/wrf/users/docs/)].
- SKAMAROCK, W.C., 2004: Evaluating mesoscale NWP models using kinetic energy spectra. – *Mon. Wea. Rev.* **132**, 3019–3032, DOI: 10.1175/MWR2830.1.
- SMEDMAN, A.S., U. HÖGSTRÖM, H. BERGSTRÖM, 1996: Low level jets—a decisive factor for off-shore wind energy siting in the Baltic Sea. – *Wind Engineering* 137–147.
- SMEDMAN, A.S., H. BERGSTRÖM, B. GRISOGONO, 1997: Evolution of stable internal boundary layers over a cold sea. – *J. Phys.: Conf. Ser.* **102**, 1091–1099, DOI: 10.1029/96JC02782.
- SMITH, C.M., R. BARTHELMIE, S. PRYOR, 2013: In situ observations of the influence of a large onshore wind farm on near-surface temperature, turbulence intensity and wind speed profiles. – *Environ. Res. Lett.* **8**, 034006, DOI: 10.1088/1748-9326/8/3/034006.
- SMITH, R.B., 2010: Gravity wave effects on wind farm efficiency. – *Wind Energ.* **13**, 449–458, DOI: 10.1002/we.366.
- SMITH, S.D., 1980: Wind stress and heat flux over the ocean in gale force winds. – *J. of Phys. Ocean.* **10**, 709–726.
- STAUFFER, R., G.J. MAYR, M. DABERNIG, A. ZEILEIS, 2015: Somewhere over the rainbow: How to make effective use of colors in meteorological visualizations. – *Bull. Amer. Meteor. Soc.* **96**, 203–216.
- STEELE, C., S. DORLING, VON R. GLASOW, J. BACON, 2012: Idealized wrf model sensitivity simulations of sea breeze types and their effects on offshore windfields.. – *Atmos. Chem. Phys.* **12**, DOI: 10.5194/acp-13-443-2013.
- STEELE, C., S. DORLING, VON R. GLASOW, J. BACON, 2015: Modelling sea-breeze climatologies and interactions on coasts in the southern north sea: implications for offshore wind energy. – *Q. J. R. Meteorol. S.* **141**, 1821–1835, DOI: 10.1002/qj.2484.
- SUN, H., Y. LUO, Z. ZHAO, R. CHANG, 2018: The impacts of Chinese wind farms on climate. – *Journal of Geophysical Research: Atmospheres* **123**, DOI: 10.1029/2017JD028028.
- SVENSSON, N., H. BERGSTRÖM, E. SAHLÉE, A. RUTGERSSON, 2016: Stable atmospheric conditions over the Baltic Sea: model evaluation and climatology. – *Boreal Environment Research* **21**, 387–404.

- THYNG, K.M., C.A. GREENE, R.D. HETLAND, H.M. ZIMMERLE, S.F. DiMARCO, 2016: True colors of oceanography: Guidelines for effective and accurate colormap selection. – *Oceanography* **29**, 9–13.
- TÜRK, M., S. EMEIS, 2010: The dependence of offshore turbulence intensity on wind speed. – *J. Wind Eng. Ind. Aerodyn* **98**, 466–471, DOI: doi.org/10.1016/j.jweia.2010.02.005.
- VANDERWENDE, B.J., B. KOSOVIC, J.K. LUNDQUIST, J.D. MIROCHA, 2016: Simulating effects of a wind-turbine array using LES and RANS. – *Journal of Advances in Modeling Earth Systems* **8**, 1376–1390, DOI: 10.1002/2016MS000652.
- VAUTARD, R., F. THAIS, I. TOBIN, F.M. BRÉON, J.G.D. DE LAVERGNE, A. COLLETTE, P. YIOU, P.M. RUTI, 2014: Regional climate model simulations indicate limited climatic impacts by operational and planned european wind farms. – *Nat. Commun.* **5**, ncomms4196, DOI: 10.1038/ncomms4196.
- VERHOEF, A., M. PORTABELLA, A. STOFFELEN, H. HERSBACH, 2008: CMOD5. n-the CMOD5 GMF for neutral winds. Technical report, KNMI, De Bilt, Netherlands.
- VOLKER, P., J. BADGER, A.N. HAHMANN, S. OTT, 2015: The Explicit Wake Parametrisation V1. 0: a wind farm parametrisation in the mesoscale model WRF. – *Geosci. Model Dev.* **8**, 3715–3731, DOI: 10.5194/gmd-8-3715-2015.
- VOLKER, P.J., A.N. HAHMANN, J. BADGER, H.E. JØRGENSEN, 2017: Prospects for generating electricity by large onshore and offshore wind farms. – *Environ. Res. Lett.* **12**, 034022.
- WANG, C., R.G. PRINN, 2010: Potential climatic impacts and reliability of very large-scale wind farms. – *Atmospheric Chemistry and Physics* **10**, 2053–2061, DOI: 10.5194/acp-10-2053-2010.
- WANG, C., R.G. PRINN, 2011: Potential climatic impacts and reliability of large-scale offshore wind farms. – *Environ. Res. Lett.* **6**, 025101, DOI: 10.1088/1748-9326/6/2/025101.
- WINDEUROPE, 2017: Wind energy in Europe: Outlook to 2020. Available online at <https://windeurope.org/about-wind/reports/wind-energy-in-europe-outlook-to-2020>.
- WU, Y.T., F. PORTÉ-AGEL, 2015: Modeling turbine wakes and power losses within a wind farm using LES: An application to the Horns Rev offshore wind farm. – *Renewable Energy* **75**, 945–955, DOI: 10.1016/j.renene.2014.06.019.

- XIA, G., M.C. CERVARICH, S.B. ROY, L. ZHOU, J.R. MINDER, P.A. JIMENEZ, J.M. FREEDMAN, 2017: Simulating Impacts of Real-World Wind Farms on Land Surface Temperature Using the WRF Model: Validation with Observations. – *Mon. Wea. Rev.* , DOI: 10.1175/MWR-D-16-0401.1.
- XIA, G., L. ZHOU, J.R. MINDER, R.G. FOVELL, P.A. JIMENEZ, 2019: Simulating impacts of real-world wind farms on land surface temperature using the WRF model: physical mechanisms. – *Clim Dyn* 1–17.
- XIE, S., C.L. ARCHER, 2017: A numerical study of wind-turbine wakes for three atmospheric stability conditions. – *Boundary-Layer Meteorol* **165**, 87–112, DOI: 10.1007/s10546-017-0259-9.
- ZHANG, W., C.D. MARKFORT, F. PORTÉ-AGEL, 2013: Experimental study of the impact of large-scale wind farms on land–atmosphere exchanges. – *Environ. Res. Lett.* **8**, 015002, DOI: 10.1088/1748-9326/8/1/015002.
- ZHOU, L., Y. TIAN, S.B. ROY, C. THORNCROFT, L.F. BOSART, Y. HU, 2012: Impacts of wind farms on land surface temperature. – *Nature Climate Change* **2**, 539–543, DOI: 10.1038/NCLIMATE1505.



## Acknowledgments

First things first, I am deeply grateful to Theresa for her support during the whole time of my Ph.D. and for taking care of our daughter Rosalie especially at the final stage of the Ph.D.! Further, I want to thank my parents for encouraging me during tough times.

I am also grateful to Stefan Emeis for supervising me and having the initial idea to execute aircraft measurements downwind of offshore wind farms. The success of this study is largely rooted in the novel airborne data. Moreover, he helped me to feel confident in the scientific community by giving me the freedom to participate at international conferences, workshops and summer schools and by allowing me to spend several months abroad, increasing my international network.

I am grateful to Julie K. Lundquist for supervising me during my stay at CU and mentoring me until the very end of my Ph.D.. Besides, she did not only care about the scientific progress she also cared about my well-being during my research stay in Boulder - a great recipe for success.

Additionally, I am grateful to:

Prof. Dr. Yaping Shao for reviewing this thesis and being part of the examination committee.

Prof. Dr. Bülent Tezkan and Dr. Frank Steffany for being part of the examination committee.

Ingo, Marcus, Konstantin, Baldur, Benne, Felix and Krischan for the amazing lunch breaks whether this was on bike, ski or at the sport climbing crag.

The cooking group for great lunches - I will miss the Käsespätzle of Konstantin.

Alexander Gohm for giving me the education and advice needed to do a Ph.D. successfully, during my masters and as a mentor later.

Lukas Umek, Daniel Leukauf und Christopher Holst for sharing their python code and giving me advice in case I had any issues with WRF.

Andreas Schenk, the manager of the Graduate School GRACE, making it possible to spend three months of my Ph.D. in wonderful Boulder, Colorado, USA.

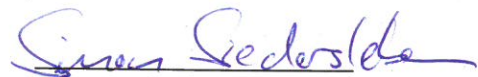
The WIPAFF project was funded by the German Federal Ministry of Economic Affairs and Energy (grant number: FKZ 0325783) on the basis of a decision by the German Bundestag. JKL's efforts were supported by the National Science Foundation under grant BCS-1413980 (Coupled Human Natural Systems). The Graduate School GRACE funded the research stay at CU of SKS. The WRF output was post-processed by the use of the python library wrf-python (LADWIG 2019) and visualized with matplotlib (HUNTER 2007). The simulations were performed on the keal cluster hosted by the IMK-IFU and gratefully managed by Benjamin Fersch and before him, by Dominikus Heinzeller. We visualized the WRF data by using colors as suggested by STAUFFER et al. (2015) and THYNG et al. (2016). We also thank the European Space Agency (ESA) for making Copernicus Sentinel-1 SAR data freely available.

## Eidesstattliche Erklärung

Ich versichere, dass ich die von mir vorgelegte Dissertation selbständig angefertigt, die benutzten Quellen und Hilfsmittel vollständig angegeben und die Stellen der Arbeit - einschließlich Tabellen, Karten und Abbildungen -, die anderen Werken im Wortlaut oder dem Sinn nach entnommen sind, in jedem Einzelfall als Entlehnung kenntlich gemacht habe; dass diese Dissertation noch keiner anderen Fakultät oder Universität zur Prüfung vorgelegen hat; dass sie - abgesehen von unten angegebenen Teilpublikationen - noch nicht veröffentlicht worden ist, sowie, dass ich eine solche Veröffentlichung vor Abschluss des Promotionsverfahrens nicht vornehmen werde. Die Bestimmungen der Promotionsordnung sind mir bekannt. Die von mir vorgelegte Dissertation ist von Prof. (apl) Dr. Stefan Emeis betreut worden.

21.01.2020

Datum



Unterschrift

Siedersleben, S. K., A. Platis, J. K. Lundquist, A. Lampert, K. Bärfuss, B. Cañadillas, B. Djath, J. Schulz-Stellenfleth, J. Bange, T. Neumann, S. Emeis, 2018: Evaluation of a Wind Farm Parametrization for Mesoscale Atmospheric Flow Models with Aircraft Measurements. Meteorol. Z., 27, 401-415. DOI: 10.1127/metz/2018/0900

Siedersleben, S. K., J. K. Lundquist, A. Platis, J. Bange, K. Bärfuss, A. Lampert, B. Cañadillas, T. Neumann, S. Emeis, 2018: Micrometeorological Impacts of Offshore Wind Farms as seen in Observations and Simulations. Environ. Res. Lett., 13, 124012. DOI: 10.1088/1748-9326/aaea0b

Siedersleben, S. K., Platis, A., Lundquist, J. K., Djath, B., Lampert, A., Bärfuss, K., Cañadillas, B., Schultz-Stellenfleth, J., Bange, J., Neumann, T., and Emeis, S.: Observed and simulated turbulent kinetic energy (WRF 3.8.1) overlarge offshore wind farms, Geosci. Model Dev. Discuss., accepted for publication, DOI: 10.5194/gmd-2019-100